THE UNIVERSITY OF CHICAGO

DNA BASED ADVANCED BIOIMAGING TECHNIQUES FOR QUANTITATIVE BIOLOGY

A DISSERTATION SUBMITTED TO

THE FACULTY OF THE DIVISION OF THE PHYSICAL SCIENCES

IN CANDIDACY FOR THE DEGREE OF

DOCTOR OF PHILOSOPHY

DEPARTMENT OF CHEMISTRY

BY

VED PRAKASH

CHICAGO, ILLINOIS

MARCH 2018

DEDICATION

to SCIENCE

LIST OF CONTENTS

List of figures

List of tables

Abbreviations

ALBRs	anionic ligand binding receptors
BAC	10,10′-bis[3-carboxypropyl]-9,9′-biacridinium dinitrate
BMDC	bone marrow derived dendritic cells
CFP	cyan fluorescent protein
DCM	dichloromethane
DHEA	dehydroepiandrosterone
DMEM	dulbecco's modified eagle's medium/f-12 (1:1)
DMF	dimethyl formamide
DNase	deoxyribonuclease ii
dsDNA	double stranded dna
EDC	1-ethyl-3-(3-dimethylaminopropyl) carbodiimide
FBS	fetal bovine serum
FISH	fluorescence in situ hybridization
FLIM	fluorescence lifetime imaging microscopy
FRET	Forster's resonance energy transfer
FWHM	full width at half maxima
HPLC	high performance liquid chromatography
HRMS	high resolution mass spectrometry
IRF	instrument response function
iSHiRLoC	intracellular single-molecule high-resolution localization and counting
LSDs	lysosomal storage disorders
MHC	major histocompatibility complex

NHS	n-hydroxysuccinimide
oSHiRLoC	organellar single-molecule high-resolution localization and counting
PAINT	point accumulation for imaging in nanoscale topography
PALM	photoactivated localization microscopy
PET	photoinduced electron transfer
PNA	peptide nucleic acid
qPAINT	quantitative PAINT
TCSPC	time correlated single photon counting
TFA	tri fluoro acetic aid
TFP	topaz fluorescence protein
TLR-9	toll like receptor-9
TMR	tetramethylrhodamine
YFP	yellow fluorescence protein

List of publications

1. **Prakash, V**., Tsekouras, K., Walter, N. G., Pressé, S. and Krishnan, Y.* (2017) Quantitative maps of endosomal DNA processing by molecule counting. *Manuscript under preparation*
2. Bhatia, D., Arumugam, S., Nasilowski, M., Joshi, H., Wunder, C., Chambon, V., **Prakash, V.,** Grazon, C., Nadal, B., Maiti, P. K., Johannes, L.*, Dubertret, B.* and Krishnan, Y.* (2016) Quantum dot-loaded monofunctionalized DNA icosahedra for single-particle tracking of endocytic pathways. *Nature Nanotechnology*, 11, 1112–1119
3. **Prakash, V.**, Saha, S.,[1] Chakraborty, K. and Krishnan, Y.* (2016) Rational design of a quantitative, pH-insensitive, nucleic acid based fluorescent chloride reporter. *Chemical Science*, 2016, 7, 1946 – 1953
4. Saha, S., **Prakash, V.**, Halder, S., Chakraborty, K. and Krishnan, Y.* (2015) A pH-independent DNA nanodevice for quantifying chloride transport in organelles of living cells. *Nature Nanotechnology*, 10, 645-651 (2015)

Acknowledgements

I would like to extend my sincere thanks to everyone who supported and contributed towards my PhD work. I would like to extend my heartfelt gratitude to Prof. Yamuna Krishnan for her patience, guidance, encouragement, dedication and support towards making things happen. I would like to thank the thesis committee members Prof. Jayant Udgaonkar, Prof. Sandhya Koushika, Dr. Rahul Roy, Dr. Bryan Dickinson and Dr. Vytas Bindokas for providing critical inputs and useful insights. Our collaborators Prof. Nils Walter, Prof. Steve Pressé, Dr. Konstantinos Tsekouras, Dr. Sethuramasundaram Pitchiaya, Dr. Laurie Heineke and Elizabeth Cameron deserve a special thanks for the valuable help they provided throughout the molecule counting project. I was fortunate enough to learn from Prof. Jayant Udgaonkar and Prof. G. Krishnamoorthy the nuances of fluorescence lifetime set up and data analysis associated with it.

I am extremely grateful to Dr. Sonali Saha for all the hard work she put in synthesizing and characterizing constructs used in Clensor studies. While Shareefa Thekkan, Maulik S. Jani, Kasturi Chakraborty and Dr. Ka Ho Leung helped a lot with cell cultures as well as intellectual inputs, my lab members Dhiraj Bhatia, Dr. Aneesh T. Veetil, Dr. Krishna Dan, Dr.Nagarjun Narayanaswamy, Anand Saminathan, Bhavyashree Suresh, Junyi Zou, John Devany, Dr. Sunaina Surana, Dr. ShabanaMehtab, Dr. Saikat Chakraborty, Dr. Suruchi Sharma and Dr. Saheli Halder deserve a special mention for having intellectual discussions with me. Thanks to Shiba for hosting me during my visits to University of Michigan.

I am grateful to Hossein Pourreza and Aditya Prakash for their excellent coding skills and helping me through Python code and running it on RCC, University of Chicago cluster. I would also like to thank Dr. Justin Jureller for fluorescence lifetime studies, integrated light microscopy core facility at University of Chicago and Nikon imaging facility at Northwestern University for FLIM

imaging facility. My sincere gratitude is extended to Dr. Manoj Mathew at NCBS imaging facility for training me on microscope.

This acknowledgement would be incomplete without the mention of my family members especially my grandfather, parents, Nitika and Ankita for supporting me through toughest of times. I am indebted to Sravan Perla, Dr. Archit Trivedi, Dr. Shweta Aras, Shantanu Mangalvedhekar, Amrutha Sakaray, Krishna Garimella, Lakshmi Cherukuri, Vidyadhar Tatipamula and Sreerama Tatipamula for all the encouragement and mentoring they provide for development of my professional skills, in which they already excel.

Lastly I would like to thank Council of Scientific and Industrial research, Tata Institute of Fundamental Research and University of Chicago for providing the necessary funds that were required to complete my PhD.

Synopsis

Background

Nucleic acid based imaging methods have given rise to high-end quantitative functional imaging for fixed as well as live biological samples (Chakraborty et al. 2016). This has been achieved by virtue of predictable base pairing, high programmability, biocompatibility and development of advanced synthesis methods to synthesize nucleic acids in large quantities with high purity. A few notable applications include endosomal pH sensing using a pH- sensitive DNA nanodevice called the I-switch (Modi et al. 2009; Surana et al. 2011), chloride sensing using a pH-insensitive DNA nanodevice called *Clensor* (Saha et al. 2015a; Chakraborty et al. 2017), biologically active molecule delivery with spatiotemporal control using light responsive polymer loaded into an icosahedron made from DNA (Veetil et al. 2017), DNA-based super resolution imaging (Jungmann et al. 2014) and molecule counting using quantitative Points Accumulation In Nanoscale Topography (qPAINT) (Jungmann et al. 2016).

Chloride plays a major role in cellular homeostasis by regulating the lumenal pH of intracellular organelles and its function (Weisz 2003), and its imbalance leads to diseased conditions like cystic fibrosis and lysosomal storage disorders (Di et al. 2006; Stauber and Jentsch 2013). *Clensor* based chloride measurement was a major landmark in the field of chloride sensing as it enabled first measurement of luminal chloride concentration in lysosomes (Saha et al. 2015b) as well as along the endocytic pathway of a live multicellular organism (Chakraborty et al. 2017). *Clensor* based chloride measurements have provided insight into intracellular localization of chloride channels as well as their role in lysosomal storage disorders. These measurements were made possible by optimizing the molecular design of *Clensor* to achieve high sensitivity and

specificity while maintaining its robustness and targetability. Fluorescence lifetime based molecular probing has been used extensively to study variation of photophysical properties of fluorophores as a function of their environment (Anon 2006). In chapter I of this thesis, we have given a brief description of existing quantitative bioimaging techniques and what has been our addition to the field. In chapter II of this thesis, we have explored the use of fluorescence lifetime and ratiometric fluorescence intensity to get an insight into general design principles of ion-sensitive nucleic acid reporters based on the sensing strategy of *Clensor* (Prakash et al. 2016).

Molecule counting is a technique using which one can count individual molecules of a given species in a sample with high spatial precision and is a growing area of research in the field of quantitative biology. To utilize nucleic acid based sensing and cargo delivery platform maximally, it is indispensable to understand how many such devices are uptaken by a cell or accommodated in an organelle and how are they spatiotemporally processed within a cell. Despite the development of several methods for cargo quantification in the cytosol (Puchner et al. 2013; Jungmann et al. 2016; Lee et al. 2012; Pitchiaya et al. 2012), cargo quantification in subcellular compartments has not yet been achieved. (Jung et al. 2017). In chapter III, we have modified an advanced imaging protocol called intracellular Single-molecule High-Resolution Localization and Counting (iSHiRLoC) (Pitchiaya et al. 2012) in conjunction with LabView and Python based image analysis (Tsekouras et al. 2016) to quantify the number of DNA nanodevices uptaken by receptor mediated endocytosis as a function of time and the effect of DNase II activity in macrophages. This study sets up a general platform for quantification of cargo within intracellular compartments.

Rational design of a quantitative, pH-insensitive, nucleic acid based fluorescent chloride reporter

Most protein-based chloride sensors are pH sensitive, and hence cannot be used to measure chloride in acidic subcellular compartments like lysosomes (Sonawane et al. 2002). We have described a pH-independent, fluorescent chloride reporter called *Clensor* that has successfully measured resting chloride in organelles of living cells (Saha et al. 2015b). Here, we describe the rational design of *Clensor* (Prakash et al. 2016). *Clensor* integrates a chloride sensitive fluorophore called 10,10′-bis[3-carboxypropyl]-9,9′-biacridinium dinitrate (BAC) (Sonawane et al. 2002) with the programmability, modularity and targetability available to nucleic acid scaffolds. We show that simple conjugation of BAC to a DNA backbone fails to yield a viable chloride-sensitive reporter. Fluorescence intensity and lifetime investigations on a series of BAC-functionalized structural variants yielded molecular insights that guided the rational design and successful realization of the chloride sensitive fluorescent reporter, *Clensor* (Saha et al. 2015a). This study provides some general design principles that would aid the realization of diverse ion-sensitive nucleic acid reporters based on the sensing strategy of *Clensor*.

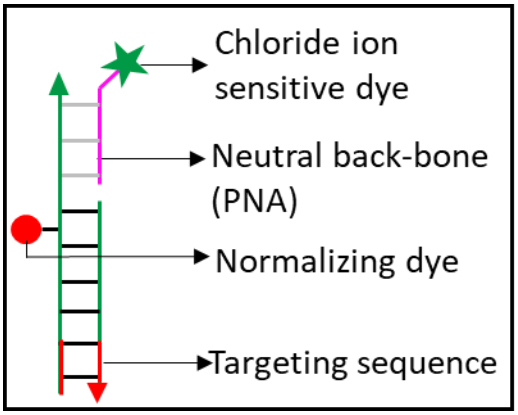

Figure 1 *Schematic of Clensor showing its constituent modules*

Molecule counting of endosomal cargo maps DNase II activity spatially and temporally.

With the advent of modern bio-imaging techniques and advanced computational power, quantitative biology has become highly topical. Given the growth of nucleic-acid based architectures being administered to living cells for various biomedical applications, it is important to understand the quantity of endocytosed DNA architectures, their kinetics of processing and the spatial and temporal effects of molecular players involved in the processing pathways. Molecule counting is considered the most accurate method to quantify organellar cargo (Jung et al. 2017). A few recent reports have successfully located and counted target molecules in an endosome (Puchner et al. 2013; Jungmann et al. 2016; Sugiyama et al. 2005), but protein function has not yet been quantitated. A few assays have been developed to address endosomal cargo processing however these are semi-quantitative in nature (Yang et al. 2006). Here we have combined the power of synthetic DNA architectures and iSHiRLoC (Tsekouras et al. 2016; Pitchiaya et al. 2012) based molecule counting to successfully count number of cargo DNA molecules along the ALBR mediated endocytic pathway (Modi et al. 2009) as a function of endosomal maturation. DNase II digests endocytosed DNA devices and plays a major role in determining endosomal cargo abundance as a function of endosomal maturation (Evans and Aguilera 2003). Counting the number of intact cargo DNA molecules at various endocytic stages allowed us to map DNase II activity with spatial and temporal resolution *in cellulo*. This sets up a general platform applicable to pinpointing the function of diverse cofactors, proteins or synthetic molecules that regulate in endosomal DNA or RNA processing (Coorens et al. 2015; Howell et al. 2003; Kaestner et al. 2015; Kawane et al. 2001; Crozat and Beutler 2004). It may be used to quantify amount of DNA devices endocytosed and regulate the timing of the function of endosomally localized DNA devices (Veetil et al. 2017). Lastly, knowing the number of devices per compartment, can guide the quantitation

of other chemical species in endocytic organelles from the rate of signal generation (Winterbourn et al. 2006).

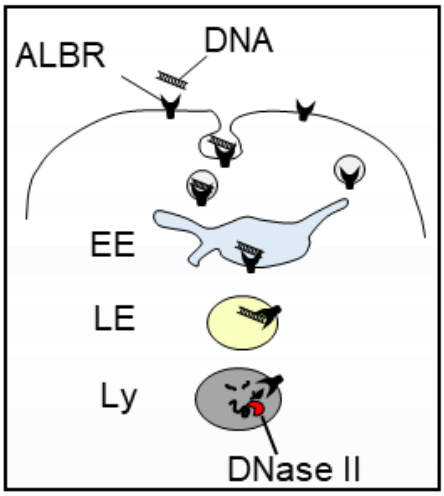

Figure 2 *Proposed model depicting spatiotemporal role of DNase II in J774 cells.*

Chapter 1

1 Introduction

1.1 DNA based devices in bio imaging

Nucleic acids form the genetic material of all living species (Dahm 2008). In the past two decades, nucleic acids have been extensively used to build numerous synthetic nanoscale architectures (Krishnan and Bathe 2012; Chakraborty et al. 2016; Seeman 2010). This could be accomplished because unlike polypeptides, polynucleotides are highly programmable molecular scaffolds. Nucleic acids regardless of their sequence, have fairly conserved dimensions (~2 nm in width) (Saenger 1984). Their secondary structure can be precisely controlled using Watson-Crick complementarity as well as unusual base pairing and they can be site-specifically decorated with molecules of choice (Jones et al. 2015). These devices exploit the modularity of nucleic acids to encode on a single device a sensing/functional module, normalizing module and targeting module to localize them specifically within target compartment in a cell or an organism. This capability to combine synthetic organic fluorophores with the capacity of nucleic acids to interface with biological molecules has resulted in a wide range of nucleic acid based nanodevices that can image biological processes in cells as well as whole organisms (Chakraborty et al. 2016).

DNA is widely used for building nanostructures due to its inherent chemical stability. A few key examples of static structures include DNA-based wires, DNA-based nanotubes, DNA-based tiles, DNA polyhedral and DNA origami. There are also dynamic DNA-based nanodevices that undergo well-defined conformational changes such as a pH sensitive DNA-based nanomachine, mention a few others that are dynamic. Some of these DNA nanodevices have been used for imaging applications in biology. A few examples include the I-switch that measures luminal pH of intracellular compartments , FISH (fluorescence in situ hybridization) that maps gene of choice in

fixed cells, molecular beacons that recognize target sequence and undergo conformational change to give fluorescent read out, DNA PAINT that maps and quantitates target macromolecule at super resolution in fixed samples (point accumulation for imaging in nanoscale topography) and aptamers that bind specifically to target molecule (Chakraborty et al. 2016). Many DNA-based nanodevices have been used for the sensitive detection of biologically relevant molecules in fixed as well as living samples with high spatiotemporal precision. For example, FISH (Amann and Fuchs 2008) and molecular beacons (Tyagi and Kramer 1996) have been used to visualize target DNA and RNA in fixed cells using Watson-Crick sense anti-sense hybridization.

1.2 Nucleic acid devices in Quantitative bio-imaging applications

DNA icosahedra have been used to map pH along the endocytic pathway *in vivo* (Bhatia et al. 2011) as well as to encapsulate and deliver a neurosteroid dehydroepiandrosterone (DHEA) via photoactivation in living cells and caged fluorophores *in vivo* (Veetil et al. 2017). The I-switch was the first DNA based nanodevices that was used inside living systems where it pH-sensitivity was leveraged to map spatiotemporal changes in pH that occurred during endosomal maturation in a living cell (Modi et al. 2014) as well as in a living organism such as *C. elegans* (Surana et al. 2011). I-switch consists of two C-rich strands connected to ends of hinged handle and undergoes pH dependent conformational change to form an i-motif (***Figure 3 a***). Ends of these C-rich strands are labeled with a FRET pair, thereby allowing ratiometric detection of pH. Aptamers are sequences of polynucleotides that have been screened via systematic evolution of ligands by exponential enrichment (SELEX) against a target small molecule or a macromolecule and bind with high specificity/affinity. A well-known example of aptamer was spinach aptamer that was screened against GFP fluorophore analogue 3,5-difluoro-4-hydroxybenzylidene imidazolinone (DFHBI) (***Figure 3 b***) (Paige et al. 2011). DFHBI in free form has very low intrinsic brightness

due to rotational/vibrational relaxation and it undergoes fluorescence brightness enhancement due to restricted motion upon binding to genetically expressed spinach aptamer. DFHBI has been used in living cells to image genetically encoded RNA aptamers that can be coexpressed with mRNA of interest (Paige et al. 2011). *Clensor* is a PNA-DNA hybrid device that can measure chloride in a manner that is independent of pH (***Figure 3 d***). This is important because all protein-based sensors have failed to measure chloride in endocytic organelles that are acidic because they are also pH sensitive (Saha et al. 2015b; Chakraborty et al. 2017). It consists of a chloride sensing dye conjugated BAC conjugated to PNA which forms the sensing module. Complementary strand with a chloride insensitive dye (Alexa 647) serves as the normalizing module, while a double stranded DNA region acts as targeting module for deploying the device in scavenger receptor pathway.

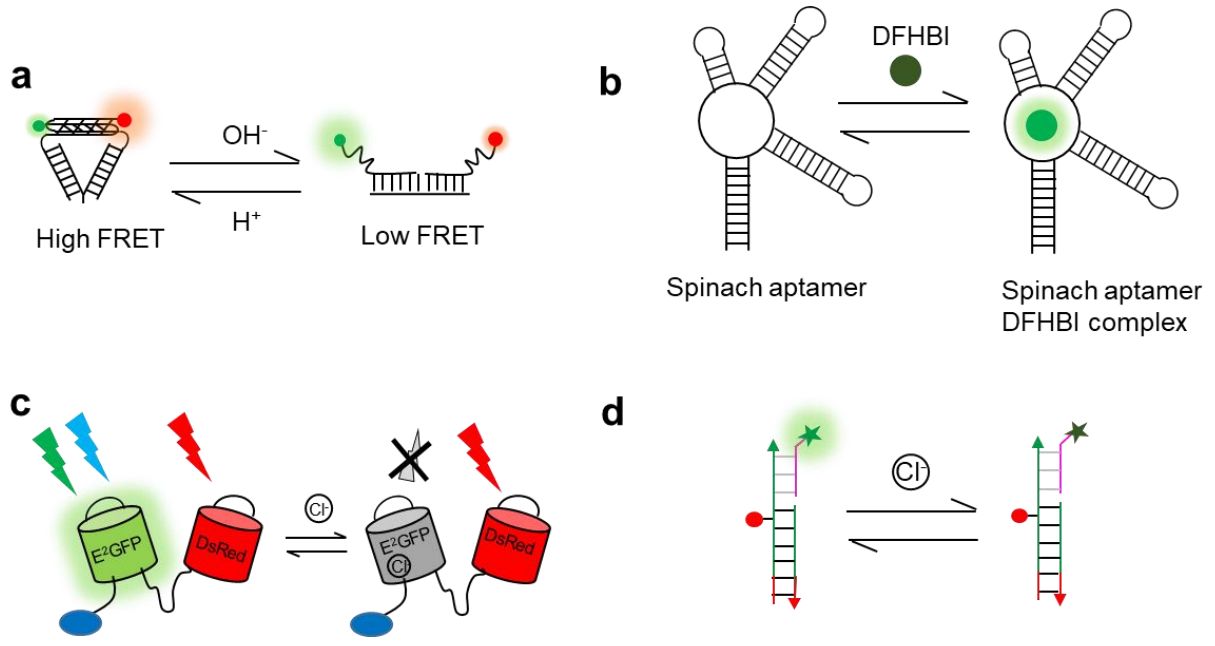

Figure 3 *Tools for quantitative imaging of ions and small molecules (a) pH sensing using I-switch (Modi et al. 2009) (b) aptamer imaging using DFHBI (Paige et al. 2011) (c) simultaneous sensing of pH and chloride by ClopHensor (Arosio et al. 2010) (d) chloride sensing by Clensor (Saha et al. 2015b).*

qPAINT is a molecule counting method where target biomolecule is immunostained by antibody labeled with a docking oligonucleotide strand (Jungmann et al. 2016). During image acquisition, a short oligonucleotide sequence labeled with fluorphore is introduced that turns on upon transiently binding to complementary docking strand (***Figure 5***). This system has been used to not just image target molecules in fixed samples at super resolution, but also count them with high precision (Jungmann et al. 2014; Jungmann et al. 2016). This was an important development because it overcame the challenge of overcounting and undercounting that most of PALM based molecule counting methods face (Jung et al. 2017).

Nucleic acid based devices are ideal candidates for investigation of biology due to high precision in molecular programmability. Thus, nucleic acid based devices stand to play a major role in quantitative bioimaging given our increased ability to process massive amounts of data with high content information.

1.3 Importance of quantitative biology

With the emergence of systems biology, it has become clear that behavior of a system is not a simple linear combination of its individual components. In order to model a living system using mathematical principles, information related to the number of molecules involved, their spatial and temporal distributions and activity levels are indispensable (Horisawa 2014). For example, mathematically modeling the process of clearance of extracellular DNA by a macrophage involves several parameters (see later) with each of them playing a critical role in regulating the function of the immune system (Kawane et al. 2014). A few of these parameters include the concentration of extracellular cargo, scavenger receptor density on cell membrane, rate of endocytosis and compartment size would determine the amount of cargo DNA that can be internalized by the cell for processing. Processing itself would be dependent on the concentration of processing enzymes

like DNase II (Seong et al. 2006), endosomal pH, concentration of other soluble luminal ions (Evans and Aguilera 2003; Shack 1959); and endosomal maturation rate. The strength of the downstream signaling and immune response would be guided by the binding affinity to receptors like TLR-9 and abundance of DNA epitope in the TLR-9 containing organelle (Atianand and Fitzgerald 2013; Chan et al. 2015)(Kawane et al. 2001). Thus accurate determination of these parameters in living systems is essential to accurately predict the behavior of biological systems by informing the development of relevant mathematical models.

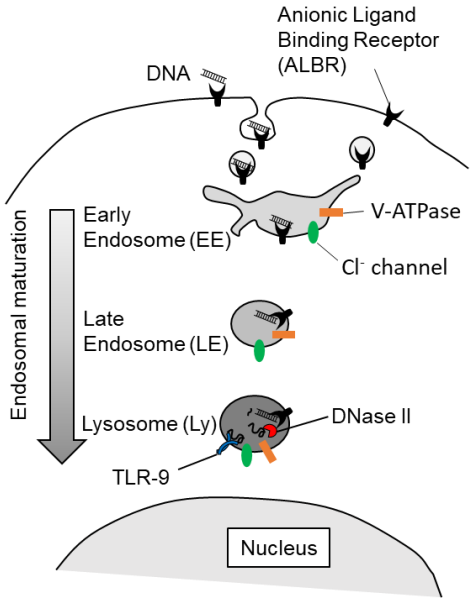

Figure 4 *Scavenger receptor pathway. Schematic representing receptor mediated endocytosis of extracellular DNA by a macrophage cell and its processing by DNase II and immune response triggering by TLR-9.*

1.3.1 Role of vesicular chloride

The ionic composition within a subcellular compartment plays a major role in regulating resident enzyme activity, thereby determining the fate of molecular cargo along the endolysosomal pathway (Shack 1959). Among various cations, the effect of pH is the most widely studied (Casey et al. 2010). In order to maintain charge balance within these compartments, membranes of these

compartments also contain a wide range of ion channels and ion exchangers that use ion gradients to transport various ions across the membrane (Weisz 2003). It is well known that chloride, the most abundant anion in biological systems, plays a critical role in maintaining ionic homeostasis in organelle lumens and the cytosol (Weisz 2003). Chloride imbalance leads to diseased conditions like cystic fibrosis, Dent's disease and lysosomal storage disorders (LSDs) (Di et al. 2006; Stauber and Jentsch 2013; Devuyst and Luciani 2015). Recently, lysosomal levels of chloride has been shown to also regulate the activity of lysosome-resident enzymes like cathepsin C and arylsulfatase (Chakraborty et al. 2017). Further, in LSDs such as osteopetrosis which is caused due to loss of function of lysosomal H^+-Cl^- exchange transporter CLC-7, the luminal levels of lysosomal chloride decreases significantly without altering pH, causing lysosomal dysfunction (Kasper et al. 2005). These observations clearly convey the message that chloride plays a role that is more significant than just being a facilitator of maintaining ionic balance within an organelle.

1.4 Methods to sense intracellular chloride

There are three main approaches to measure intracellular chloride, namely, chloride selective microelectrodes, chloride-sensitive fluorescent proteins and chloride-sensitive organic fluorescent dyes. Fluorescence methods are much more widely used because of their ability to report non-invasively and amenability to cover large sample sizes.

1.4.1 Genetically encoded chloride indicators

Genetically encoded chloride sensors sense anions via static quenching. Upon anion binding to chromophore region of the protein, the chromophore ionization constant changes, thereby causing a shift in fluorescence emission (Bregestovski et al. 2009). YFP sensitivity to anions varies as $I^- > NO_3^- > Cl^- > HCOO^- > CH_3COO^-$ (Jayaraman et al. 2000). As chloride is the most biologically abundant anion and concentration of other anions is negligible in comparison, YFP effectively acts

as chloride sensor in living systems. A few notable examples of genetically encodable ratiometric chloride probes are Clomeleon, Cl-sensor, ClopHensor and LSSmClopHensor (Germond et al. 2016). The great advantage of these sensors is that they are fairly easy to use and to implement because of their genetic encodability.

Clomeleon consists of two fluorescent proteins, Cl^- insensitive cyan fluorescent protein (CFP) and a variant of YFP, topaz fluorescence protein (TFP) connected via a short polypeptide linker (Kuner and Augustine 2000). Binding of chloride to TFP leads to reduction in fluorescence emission as a function of chloride concentration, whereas CFP fluorescence remains constant, leading to change in FRET as well as fluorescence intensity ratio. Clomeleon showed extraordinary photostability as well as proteolytic stability allowing it to be used for chloride imaging upto 2 h in cells (Berglund et al. 2006). Clomeleon has an EC_{50} value of 160 mM chloride which makes it relatively less sensitive to physiological concentrations of chloride. In order to overcome this sensitivity challenge, Cl-sensor was developed which had EC_{50} value of 30 mM, enabling it to have five-fold higher sensitivity at physiological chloride concentrations compared to Clomeleon (Markova et al. 2008). YFP in this construct has three point mutations that increase its binding kinetics to chloride. A major challenge that still remained with these sensors was that their pH sensitivity made them error prone in systems where pH varies as a function of acidity. Arosio *et al* developed an elegant protein based ratiometric sensor ClopHensor that could simultaneously measure pH as well as chloride (Arosio et al. 2010). It was constructed using fusion of an E^2GFP variant that senses pH via dual excitation method with a pKa of 6.8 while it undergoes static quenching with a binding constant of 13.1 mM for protonated form of sensor. pH and chloride insensitive Ds-red monomer was used as a normalizing fluorophore. Two challenges that still remained with these sensors were low signal to noise ratio at lysosomal pH and low photostability. LSSmClopHensor is a variant of

ClopHensor where normalizing fluorescent protein Ds-red has been replaced by a high stokes shift fluorescent protein LSSmKate2 that can be excited at the same wavelength as E2-GFP and can be imaged in red channel (Paredes et al. 2016). This greatly simplified the microscopy setup as well as time needed for carrying out simultaneous imaging of pH and chloride. There was a recent report where further mutations in the YFP demonstrated reduced pH sensitivity and enhanced photostability in Cl^--sensitive YFP, achieving a binding constant of 14 mM for chloride and a pKa of 5.9 with a 15-fold longer bleach time constant (175 seconds) than YFP (Zhong et al. 2014). Thus though proteins provide spatial resolution, they are still limited in their regimes of chloride sensing, the acidity of the microenvironment they can be deployed in, their low dynamic ranges and their response times to chloride changes.

1.4.2 Chloride sensitive fluorescent dyes

A wide range of quinolinium-derived fluorescent dyes have been reported in literature that undergo collisional quenching in presence of chloride (Geddes 2001; C D Geddes et al. 2001). These dyes have advantages of fast response times and pH insensitivity that make them good candidates for physiological chloride sensing. Unfortunately, most of these dyes have fluorescence excitation in the UV range and are not very photostable, limiting their use in biological systems (Chris D Geddes et al. 2001). However, there are reports where two photon excitation has been used to overcome these challenges (Marandi et al. 2002). Still, they cannot be used for quantitative measurements in isolation. This was circumvented by conjugating a quinolinium-based dye called BAC (10,10′-Bis[3-carboxypropyl]-9,9′-biacridinium Dinitrate) to dextran. Using a mixture of this with TMR-dextran that functioned as a reference fluorophore, it was localized in organelles through fluid phase endocytosis in order to measure chloride in endosomes (Sonawane et al. 2002). It was also conjugated to other ligands like cholera toxin B, transferrin and α_2-macroglobulin to target

compartments like Golgi, recycling endosomes and late endosomes (Sonawane and Verkman 2003). A major challenge with this system was batch to batch variation due to varying number of labels (Sonawane et al. 2002).

1.4.3 Nucleic acids for quantitative sensing in biological systems

Nucleic acids have been extensively used for making static as well as dynamic nanodevices for quantitative fluorescence bio-imaging (Krishnan and Simmel 2011; Chakraborty et al. 2016). They have been successfully used to detect and measure ions and small molecules in living cells and organisms (Modi et al. 2009; Bhatia et al. 2011; Modi et al. 2013; Surana et al. 2011; Veetil et al. 2017; Kellenberger et al. 2013). These devices are highly programmable and can be prepared in high yields and purity. They can be coupled elegantly to targeting strategies along specific cellular trafficking pathways, stable within biological systems and can be used to derive time dependent information from the system (Surana et al. 2013; Surana et al. 2015). As these devices are highly modular, each module can be prepared separately and assembled in a one pot format by leveraging the capacity of DNA to self-assemble. Even though most of these devices cannot be genetically encoded, they can integrate a conjugatable fluorescent dye with a reference fluorophore in a specific stoichiometry and be targeted to an organelle of choice with high spatiotemporal control and specificity which predisposes it studying the activity of chloride channels in situ in biological systems.

1.5 DNase II and its role in digestion of endocytosed DNA

Deoxyribonuclease (DNase) II is a 43 kDa lysosome resident endonuclease and is expressed ubiquitously in all tissue types (Evans and Aguilera 2003). It plays an important role in DNA fragmentation and degradation during apoptosis and phagocytosis (Odaka and Mizuochi 1999). Extracellular DNA generated during development and injury is endocytosed by innate immune

cells and is digested by endosomally localized DNase II. During phagocytosis, cargo is phagocytosed into a phagosome which then fuses with a lysosome to form a compartment called a phagolysosome. Hydrolytic enzymes like protease and DNase II degrade endocytosed cargo in these compartments and clear them. Malfunction of DNase II leads to accumulation of endocytosed cargo DNA and eventually causes autoimmune disorders (Lamphier et al. 2006; Blasius and Beutler 2010). DNase II was shown to play a critical role in this context, as revealed by the fact that homozygous DNase II-mutant mice (−/−) died either in utero or just after birth due to severe anemia (Kawane et al. 2001; Krieser et al. 2002). Further investigation revealed that anaemia occurred because erythroblasts in the peripheral blood of these mutant animals failed to enucleate. In a recent report DNase II based digestion was shown to be necessary for the generation of an immune response in dendritic cells in mice (Chan et al. 2015; Ohto et al. 2015). Thus accumulation of DNA due to DNase II activity inhibition is functionally significant in both mice and *Drosophila* as it negatively affects their development and immunity (Seong et al. 2006; Yu et al. 2015; Kawane et al. 2001; Lan et al. 2014; Kawane et al. 2014; Odaka and Mizuochi 1999). It is likely to do the same in other organisms (Kawane et al. 2014).

1.6 Methods to quantify organellar cargo and resident protein function

Endocytosed DNA from damaged or apoptotic cells are distinguished from viral/bacterial DNA based upon rate of digestion in endocytic compartments (Barton et al. 2006). Mechanism of manifestation of autoimmune disorders such as systemic lupus erythematosus (SLE) is a long debated topic (Pathak and Mohan 2011; Chan et al. 2015). However, it is known that undigested DNA that traffics along the endolysosomal pathway of immune cells is an important trigger of the immune response, whose dysregulated processing causes autoimmune disorders (Kawane et al. 2014). Quantitative maps of endosomal DNA processing while retaining organelle-specific

information is critical to our ability to computationally model the immune response. The ability to study endosomal processing and regulators thereof have been significantly hampered by the lack of methods to quantitatively map cargo processing in cells while retaining organelle-specific information.

Bulk measurements such as western blots have greatly helped in ascertaining relative amounts of endocytosed molecules present in a sample but they lack information on processing heterogeneity within a given sample (Jung et al. 2017). Fluorescence intensity based methods provide internal heterogeneity but lack the quantitative precision obtained by blotting. For example, in order to study disulfide reduction in endosomes, a FRET pair was connected via a thiol bond and was targeted to endosomes using folate receptors. Upon thiol reduction, while FRET intensity decreased and donor intensity increased, overall and relative thiol reductase activity in endosomes could be estimated between different samples, however, thiol-reductase activity could not be quantitated as a function of spatial resolution in a given cellular context (Yang et al. 2006).

Molecule counting is considered to be the most accurate method to quantify the absolute amount of organellar cargo (Jung et al. 2017). There are two major methods to count molecules (a) stepwise photobleaching and (b) photoactivated localization microscopy (PALM) (***Figure 5***). Stepwise photobleaching has mostly been used to find out copy numbers in a given multimeric complex (Leake et al. 2006; Penna et al. 2008). In a typical study, the molecule of choice is expressed as a fusion with a fluorescent protein, a video is recorded at a high frame rate (100 ms) and then the data is either visually analyzed or fitted using a Markov model (Chen et al. 2014). Fitting steps >10 used to be a challenge, however, with the advent of better data fitting models and advanced computational power, data fitting upto 500 photobleaching steps have been achieved (Tsekouras et al. 2016). A major limitation here is that any intensity fluctuation

during data acquisition may lead to incorrect counting (Jung et al. 2017). This challenge may be overcome by equilibrating the imaging system for a few minutes before imaging and the use of drift correction systems to prevent sample movement during data acquisition.

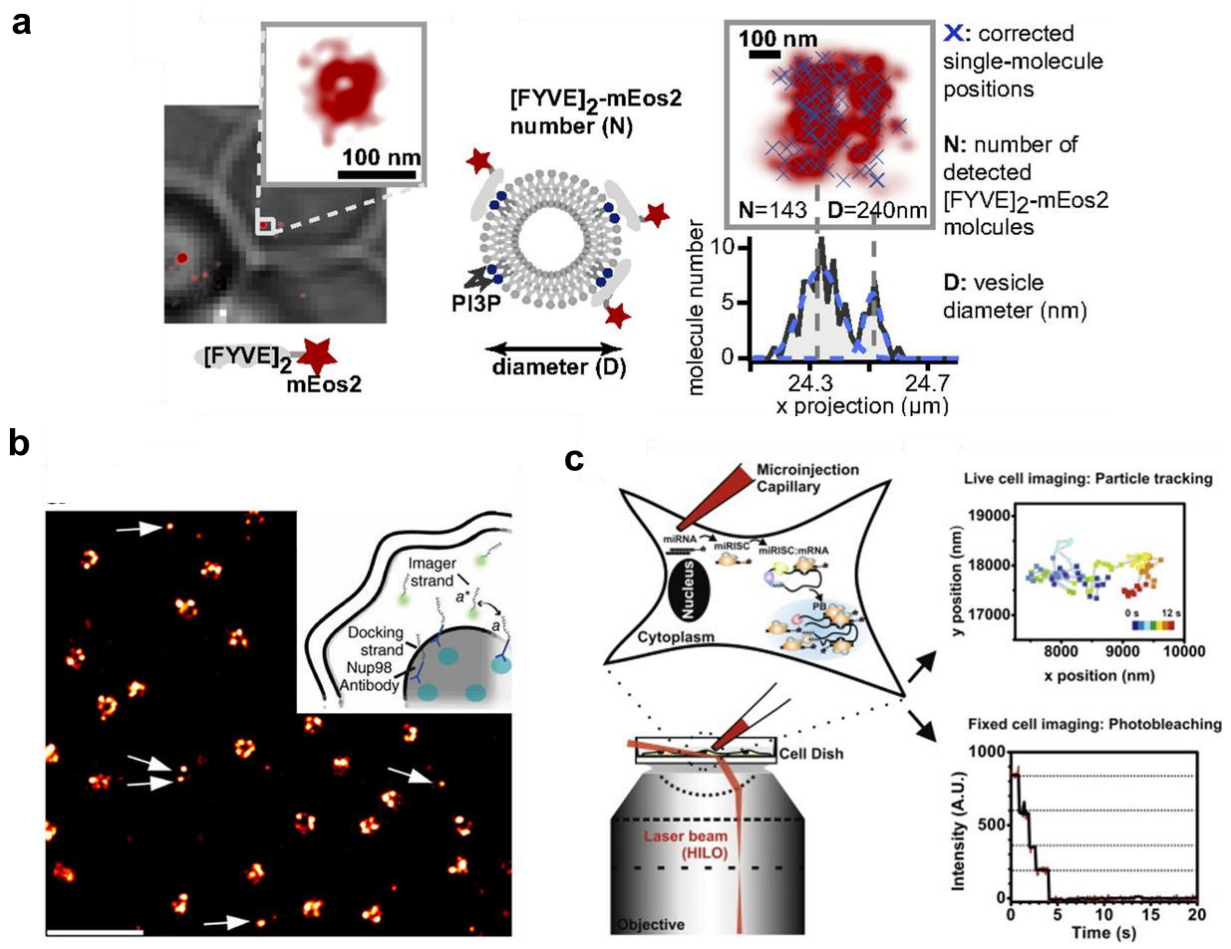

Figure 5 *Tools for molecule counting (a) super resolution imaging and counting of endosomal PI-3P using PALM imaging of FYVE-mEos2 (Puchner et al. 2013) (b) Molecule counting of monomers of nuclear pore complex using DNA qPAINT (Jungmann et al. 2016) (c) Molecule counting of labeled RNA molecules by iSHiRLoC (Pitchiaya et al. 2013).*

PALM-based counting was developed with the intent to overcome limitations in spatial resolution as well as counting associated with the conventional imaging methods described above (Jung et al. 2017). Here, the target molecule is fused with a protein that undergoes photoactivation upon irradiation with violet light (405 nm) to form a fluorescent protein. Thus, when the cell is irradiated

with a violet laser (405 nm) to sparsely activate a few molecules, the photoactivatable protein undergoes photoconversion to form a fluorescent protein that can be imaged and then photobleached (Lee et al. 2012). A key point in this method is that photoactivation must be sparse enough that the point-spread function (PSF) of the individual molecules does not overlap. This imaging sequence is cycled until no new molecules are photoactivated. Individual PSFs are then fit to a 2D Gaussian and its centroid is located and are counted. This method has been used to successfully count number of accessible phosphatidylinositol 3-phosphate (PI-3P) binding sites on a vesicle as well as size of individual vesicles (***Figure 5*** a) (Puchner et al. 2013). In order to correct for undercounting owing to immature fluorescent proteins and overcounting owing to fluorophore blinking, an intracellular calibration must be performed. As photoactivation kinetics is highly sensitive to environmental conditions as well as illumination intensity, there is a high probability of error from sample to sample. Further, fine control over protein expression of the fluorescent label can be challenging (Jung et al. 2017).

In order to overcome these challenges, a technique called qPAINT (Jungmann et al. 2016) was developed where accessible target molecules are labeled with antibodies carrying a short DNA strand (docking strand) that transiently binds to free floating dye labeled short DNA sequences (imager strand) (***Figure 5 b***). The rate of binding and unbinding depends upon docking strand concentration and hence can be used to quantify the number of target molecules present at a given spot. As qPAINT is independent of photobleaching and blinking kinetics of dye, it prevented overcounting and undercounting of molecules. Three challenges which still remain with this method are as follows: (1) stoichiometric labeling of antibodies with the docking DNA strand is still a challenge (2) the accessibility of the probe strand to the docking strand may be hindered due to the formation of secondary structures by the target DNA strand under certain conditions (3) the

leakage of small target molecules during immunolabeling. These techniques have been used to quantify number of target molecules, but they have not yet been used to probe protein activity.

1.7 Mapping DNase II activity spatially and temporally by molecule counting

DNase II is known to digest endocytosed cargo DNA (Evans and Aguilera 2003) however their site of action along the endolysosomal pathway is not yet established (Chan et al. 2015). iSHiRLoC is a molecule counting method which was developed to study intracellular localization, composition and transport of miRNA complexes. (Pitchiaya et al. 2012) HeLa cells were microinjected with let-7 miRNA and were imaged using highly inclined laminar optical sheet (HILO) microscopy to produce photobleaching decay traces of individual RNA complexes in cytosol. The number of photobleaching steps observed per trace revealed number of let-7 miRNA molecules per complex.

We proposed that if we quantify number of intact cargo DNA as a function of endosomal maturation in absence and presence of DNase II inhibitor, we can map spatiotemporal activity of DNase II along the ALBR mediated endocytic pathway (Kawane et al. 2014). Endosomal cargo quantification using oSHiRLoC is not limited to dsDNA, and is potentially applicable to a range of externally added endocytic ligands such as 'self-DNA'; or 'non-self DNA' ssDNA, dsRNA, shiga toxin, EGF, mannose-6-phosphate, that traffic along well-defined pathways (Bhatia et al. 2016; Chan et al. 2015; Rigby et al. 2014; Henault et al. 2012; Dhami and Schuchman 2004; Tomas et al. 2014). In addition to enabling the quantification of trafficking cargo, this approach can be used to evaluate the processing of solutes, receptors, and pathogenic agents with organelle-specific information. It can also be used to assay the location and activity of regulators of endosomal cargo processing (Coorens et al. 2015; Howell et al. 2003; Kaestner et al. 2015; Kawane et al. 2001; Crozat and Beutler 2004).

1.8 Thesis outline

For my PhD work, I have developed two tools for quantitative bioimaging. In the first section, I studied the rationale behind the molecular design of a fluorescent pH independent ratiometric chloride sensor called *Clensor*. It involved carrying out a structure-activity relationship between fluorescence intensity and lifetime based studies on various nucleic acid constructs which provided mechanistic insights into the function of *Clensor*. This study, afforded a step by step approach for designing and optimizing an ion sensitive nucleic acid based sensor starting from a conjugatable ion sensing dye. In the second section of my PhD work, I have used molecule counting to count number of cargo DNA molecules in endosomes of J774A.1 cells as a function of endosomal maturation. I have further used it to elucidate spatiotemporal activity of DNase II in processing endosomal cargo DNA. To enable this study, I had to modify iSHiRLoC to now make it amenable to not only count any kind of endosomal cargo, but also make it deployable to quantitatively map the activity of diverse enzymes, cofactors and molecular players involved in endosomal processing of cargo.

Chapter 2

2 Rational design of pH insensitive nucleic acid based chloride reporter: *Clensor*

Cellular metabolic homeostasis is controlled by a wide range of biochemical processes occurring in an orchestrated fashion within specific sub-cellular organelles. A complete family of ions play a major role in defining the chemistry occurring inside a specific organelle, thereby determining the fate of molecular cargo trafficking along a given pathway (Casey et al. 2010). For example, the mannose-6-phosphate dependent cargo sorting occurring in the Golgi works on the basis of a pH gradient (Coutinho et al. 2012). It is well-known that chloride is a primary facilitator of organelle acidification (Weisz 2003), and its imbalance leads to diseased conditions like cystic fibrosis and lysosomal storage disorders (Di et al. 2006; Stauber and Jentsch 2013). Not just that, it has recently been shown to play a significant role in enzyme function of lysosomal enzyme like cathepsin C and arylsulfatase B (Chakraborty et al. 2017).

There are several reports on measurement of cytosolic chloride concentration inside live cells (Sonawane et al. 2002; Inglefield and Schwartz-Bloom 1999; Jayaraman et al. 1999; Jayaraman et al. 2000; Kuner and Augustine 2000; Markova et al. 2008; Arosio et al. 2010). However the ability to accurately measure resting chloride in subcellular organelles has turned out to be challenging due to their diverse resting pH values. As most chloride reporters based on YFP are pH sensitive (Sonawane et al. 2002), and further as intracellular chloride affects lumenal pH (Stauber and Jentsch 2013), there is a need for a pH insensitive reporter that can measure chloride. Krishnan group has shown that DNA based nanodevices can function as highly sensitive, bright fluorescent reporters inside subcellular organelles of live cells and live organisms (Modi et al. 2009; Modi et

al. 2013; Surana et al. 2011; Bhatia et al. 2011). To build a nucleic acid-based ratiometric sensor for measuring intracellular chloride, we have combined the chloride sensing property of BAC with the programmability, modularity and targetability of nucleic acid scaffolds. It has been shown that a DNA-based nanodevice called *Clensor* functions as a pH-independent, fluorescent, ratiometric chloride ion reporter inside sub-cellular organelles of living cells (Saha et al. 2015b) as well as living organism (Chakraborty et al. 2017). Chapter II describes step by step process involved in rational design of *Clensor*.

2.1 Materials and Methods

2.1.1 Reagents

All unmodified oligonucleotides (**Table 2**) were procured from Sigma (India) while all the modified oligonucleotides (**Table 2**) were procured from IBA GmbH (Germany). Fluorescently labeled oligonucleotides were purified by ethanol precipitation before use to remove any contaminants from synthesis. Fluorescently labeled oligonucleotides were subjected to ethanol precipitation prior to use to remove any contaminating fluorophores. All oligonucleotides were quantified by their UV absorbance at 260 nm. The peptide nucleic acids (PNA) oligomers, P and P' (**Table 2**) were synthesized using standard solid phase Fmoc chemistry on Nova Syn® TGA resin (Novabiochem, Germany) using analytical grade reagents (Applied Biosystems®, USA), purified by reverse phase HPLC (Shimadzu, Japan). HPLC purified and lyophilized oligonucleotides were dissolved in MQ water, aliquoted into small fractions and stored at -20 °C. To quantify BAC conjugated DNA and PNA oligomers, molar extinction coefficient at 260 nm (ε_{260}) for BAC was considered as 1.65×10^5 M^{-1} cm^{-1}.

2.1.2 BAC synthesis and characterization.

10,10′-Bis[3-carboxypropyl]-9,9′-biacridinium dinitrate (BAC) and 10,10′-Bis[(3-N-succinimidyloxycarbonyl)propyl]-9,9′-biacridinium dinitrate (BAC NHS) was synthesized according to a literature procedure (Litt et al. 1985; Sonawane et al. 2002).

Step I: Acridone (Figure 6, compound I) (5 g, 0.0256 mol), potassium hydroxide (1.8 g, 0.032 mol) and absolute ethanol (80 mL) were heated to reflux (80 °C) for 30-40 min until the acridone dissolved. The ethanol and water formed were distilled off and the remaining solid was lyophilized overnight. 100 mL (large excess) γ-butyrolactone was added to the dried material and the solution was heated to reflux (205°C) for 4 h. The excess γ-butyrolactone was distilled off under reduced pressure. The remaining solid was dissolved in water, precipitated by dropwise addition of dilute HCl, filtered, and lyophilized. The lyophilized product was further purified by recrystallization from chlorobenzene to yield (70%) 10-[3-carboxypropyl]-9(10H)-acridone (Figure 6, compound II). Compound II was characterized using mass spectrometry and NMR. HRMS m/z calculated for C17H15NO3 282.1130 ([M+H]+), observed 282.1118. 1H NMR (400 MHz, DMSO-d6): δ 8.35(d, 2H, aromatic, J = 8.0 Hz), 7.33 (dd, 2H, aromatic, J1 = J2 = 4.0 Hz), 7.83 (t, 2H, aromatic, J1 = J2 = 8.0 Hz), 7.94 (d, 2H, aromatic, J = 8.0 Hz), 4.48 (t, 2H, N-CH2, J = 8.0 Hz), 2.02 (m, 2H, alkyl CH2), 2.57 (t, 2H, alkyl CH2, J = 8.0 Hz), 12.28 (s, 1H, COOH).

Step II: To a suspension of compound II (1.4 g, 5 mmol) in acetone (40 ml), zinc dust (6.6 g, 101 gram atom) was added. The mixture was then stirred at 30–40 °C for 20 min. The flask was cooled in ice-cold water, and 37% HCl (60.5 g, 613 mmol) was added dropwise over 6 h under N2 atmosphere at ~10 °C. The reaction mixture was stirred overnight at room temperature followed by addition of 25 ml of degassed water. A bright yellow precipitate was collected by filtration, rinsed with water, and dissolved in 25 ml of 5% aqueous NaOH. The mixture then was filtered,

and the filtrate was neutralized with acetic acid till bright yellow precipitate generation. The precipitate was filtered, washed with water, dried, and recrystallized from hot ethanol to yield 2.2 g (65%) of 10,10′-bis[3-carboxypropyl]-9,9′-biacridylidene (Figure 6, compound III) as yellow crystalline solid. Compound III was characterized using mass spectrometry. HRMS m/z calculated for $C_{34}H_{30}N_2O_4$ 266.1181 ($[M+2H]^{2+}$), observed 265.6102.

Step III: Compound III (2.6 g, 5 mmol) was heated in 2 N nitric acid (120 ml) for 2 h at 120 °C until most of the brownish mass was dissolved. After cooling and filtration, the precipitate was washed with dilute nitric acid, dried, and recrystallized from dilute nitric acid to yield 2.4 g (80%) of 10, 10′-bis[3-carboxypropyl]-9,9′-biacridinium dinitrate (Figure 6, compound IV) as a yellow crystalline solid. Compound IV was characterized using mass spectrometry and NMR. HRMS m/z calculated for C34H30N2O4 265.1103, observed 265.0545. 1H NMR (400 MHz, DMSO-d6): δ 9.08 (d, 4H, aromatic, J = 8.0 Hz), 8.48 (t, 4H, aromatic, J = 8.0 Hz), 7.75 (t, 4H, aromatic, J = 8.0 Hz), 7.68 (m, 4H, aromatic), 5.61 (t, 4H, N-CH2, J = 8.0 Hz), 2.07 (t, 4H, alkyl CH2, J = 4.0 Hz), 2.89 (t, 4H, alkyl CH2, J = 8.0 Hz), 12.47 (s, 2H, COOH).

Step IV: To prepare 10, 10′-Bis[(3-N-succinimidyloxycarbonyl)propyl]-9,9′-biacridinium dinitrate (Figure 6, compound V), compound IV (1.0 mg, 1.53 μmol) was dissolved in DMF (500 μl) and triethylamine (12.5 μl). After addition of N-hydroxysuccinimide (NHS) (0.7 mg, 4.0 equiv.), and 1-Ethyl-3-(3-dimethylaminopropyl) carbodiimide (EDC) (0.58 mg, 2.0 equiv.); the mixture was stirred in the dark for 18 h followed by spin down at 10,000 rpm for 10 min to remove the precipitated if any. The supernatant (DMF solution of BAC-NHS) was used directly to conjugate to DNA and PNA. Compound V was characterized using mass spectrometry. HRMS m/z calculated for $C_{42}H_{36}N_4O_8^{2+}$ 362.1266, observed 362.1573.

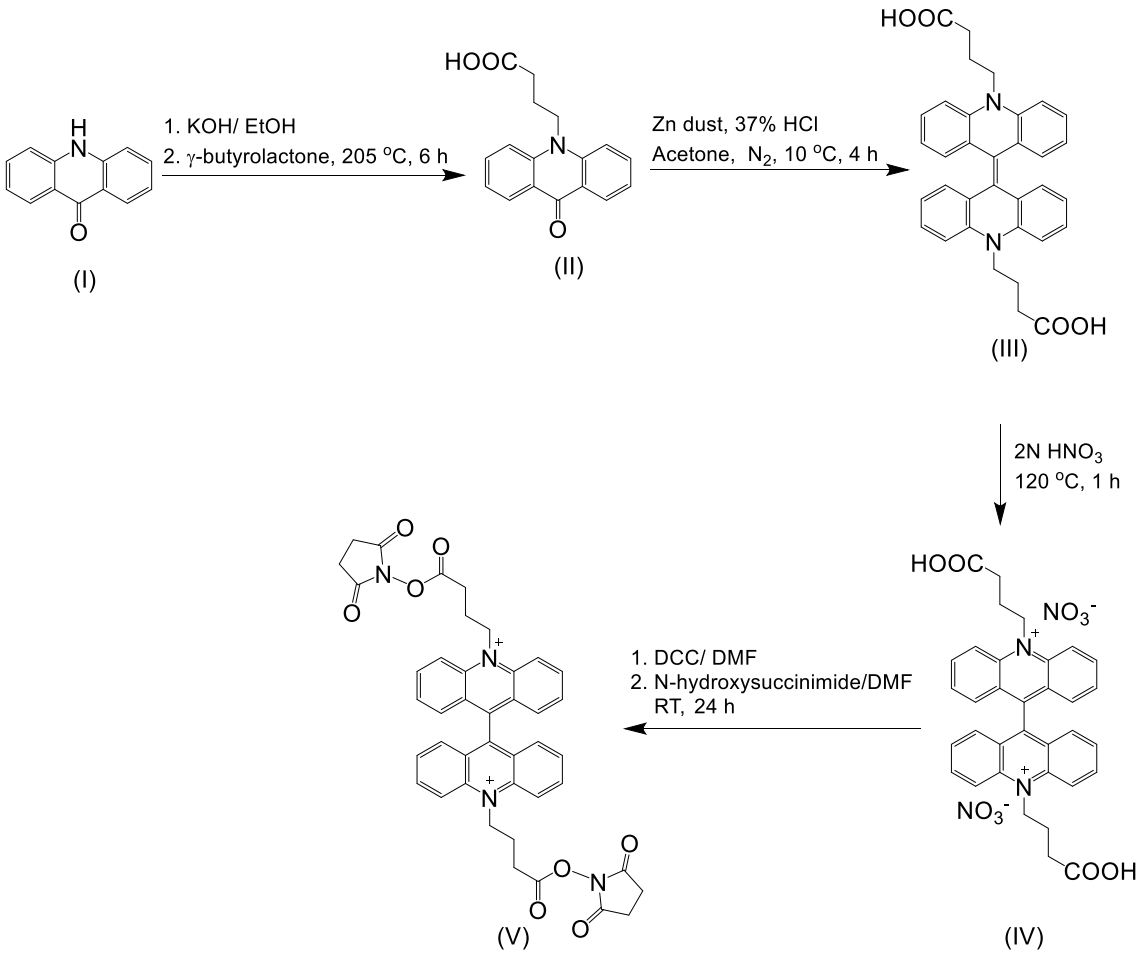

Figure 6 *Reaction scheme for synthesis of BAC NHS ester*

2.1.3 BAC-DNA conjugates preparation and purification.

Amine labeled DNA (2.5 nmol) was dissolved in 180 µL of 100 mM sodium phosphate buffer, pH 8.5. 20 µL (25 nmol) of freshly prepared above mentioned DMF solution of BAC-NHS ester was added to DNA and stirred for 4 h at room temperature. The reaction mixture was then subjected to reverse phase HPLC (Shimadzu, Japan) purification to isolate the BAC-DNA conjugates. A linear H_2O/CH_3CN gradient starting from 5/95 (v/v) to 100/0 (v/v) over 30 min was employed. In a typical procedure, 100 µL of crude reaction mixture was injected into an analytical C18 column (Phenomenex, LunaC18, 100 Å pore size, 5 µm bead size with dimensions of 250 mm × 4.6 mm)

and separated using the above mentioned gradient with a flow rate of 2 mL/min. In order to avoid multiple conformation adopted by single BAC-DNA conjugate during purification, the HPLC column was kept inside a temperature controllable unit (CTO 20A, Shimadzu) to maintain a constant temperature of 40 °C throughout the procedure. Fractions corresponding to BAC-DNA conjugates starting from 20.0 min to 21.0 min were collected, concentrated and stored at -20 °C.

2.1.4 PNA synthesis and characterization.

PNA synthesis was performed using standard solid phase Fmoc chemistry on Nova Syn® TGA resin (Christensen et al. 1995; Koch et al. 1997) using analytical grade reagents. In brief, Fmoc-Lys (Boc)-NovaSyn® TGA (cat. No. 04-12-2662) was weighed out in a dry vac-elute column containing a rice grain magnetic stir bar. The resin was swollen in dry DCM overnight (6-8 h) with gentle stirring. DCM was removed by applying vacuum and the resin was washed with dry DCM thrice. Freshly prepared 600 µL 20 % piperidine in dry DMF was added to the resin and stirred gently for 30 min. The piperidine solution was then replaced with fresh solution and was stirred for another 30 min. The piperidine solution was removed by applying vacuum, and the resin was alternatively washed thrice with dry DCM, twice with dry DMF and finally with dry DCM. To this deprotected resin, 600 µL of coupling solution containing PNA monomer (Fmoc-N-A/G/C-Bhoc-COOH or Fmoc-N-T-COOH) along with HATU, HOAT and DIPEA-lutidine mix in NMP was added. The coupling mixture used was added five equivalents in excess of the loading value of the resin for efficient coupling. The coupling reaction was carried out for 2 h with gentle stirring, with an exception to the first coupling which was carried out for 6 h. Each coupling step was followed by three DCM, two DMF and one DCM wash in the same order. To the resin, 600 µL of 20% piperidine in DMF was added and this cycle was repeated until the complete sequence was synthesized. After coupling of the lysine residue (Fmoc-Lys(Mtt)-OH) at the N-terminus, 600 µL

of a freshly prepared mixture of TFA/ TIS/ DCM (1:5:94) was added and stirred gently for 5 min to remove methytrityl (Mtt) group, for conjugation of BAC at the e-N site . This step was repeated thrice with fresh solutions for complete deprotection. After that, the resin was washed as mentioned earlier. The resin was neutralized by addition of 10% DIPEA in DCM. To the Mtt deprotected resin, BAC-NHS ester in DMF (10 eqv.) was added and stirred gently for 16-18 h. The final Fmoc deprotection was carried out as described earlier and the BAC conjugated PNA sequence (BAC-PNA) was cleaved from the resin bed by treatment with a mixture of TFA/TIS/water (95:2.5:2.5) with vigorous stirring for 1.5 h. The step was repeated twice and the flow through solution obtained was collected in a round bottom flask. The cleaved resin was washed twice with water, 500 μL EtOH and 500 μL DCM for 30 min each and the washings were collected in the same flask. The collected solution was evaporated completely in a Rotavapor® (Buchi, Switzerland) Synthesized BAC-PNA was precipitated by cold and dry ether. The precipitated material was dried and dissolved in MQ water after careful decanting of the supernatant. This crude reaction mixture was then subjected to purification by RP-HPLC (Shimadzu, Japan). CH_3CN/H_2O gradient starting from 5/95 (v/v) to 45/55 (v/v) over 5 min and 45/55 (v/v) to 100/0 (v/v) over 25 min was employed. 0.1% TFA was added to CH_3CN/H_2O mixture to sharpen the eluted peaks. In a typical experiment, 100 μL of crude product solution was injected into an analytical C18 column (Phenomenex, Luna C18, 100 Å pore size, 5 μm bead size with dimensions of 250 mm × 4.6 mm) and separated using the above mentioned gradient with a flow rate of 2 mL/min. In order to minimize multiple conformations formed by BAC-ssPNA, the column was kept inside a temperature controllable unit (CTO 20A, Shimadzu) to maintain a constant temperature of 40 °C throughout the procedure. Fractions starting from 16.5 min to 17.5

min were collected and subjected to positive ion ESI-MS analysis. BAC-ssPNA was stored as a 2 mM aqueous solution at -20 °C.

2.1.5 Mass spectrometry.

Mass spectrometry studies for BAC were performed on a Micromass ESI-MS Q-TOF Ultima Mass Spectrometer (Manchester, UK) with micro-channel plate detector in positive ion mode. Samples were diluted into a final concentration of ~400 μM using 1:1 mixture of methanol and water containing 0.1% formic acid. Synthesized ssPNA and BAC-ssPNA purified by reverse phase HPLC were characterized using positive ion mode ESI-MS on coupled Synapt G2 HD mass spectrometer (Waters). The ssPNA and BAC-ssPNA samples were diluted to a final concentration of ~20 μM using a solution of a 1:1 mixture of water and acetonitrile containing 0.1% formic acid. The mass spectra were acquired with a source temperature of 70 °C, capillary voltage at 1.5 kV and cone voltage at 60 V. MassLynx 4.0 software was used for the analysis of the spectra obtained. The HPLC fraction containing the right mass was taken further for subsequent studies. The HPLC profile and mass spectrum of the crude product after cleavage indicated that the synthesized BAC-ssPNA was quite pure.

Table 1 Mass spectrometry of ssPNA and BAC-ssPNA. *Molecular weight of ssPNA and BAC-ssPNA as determined by electrospray ionization mass spectrometry (ESI-MS). M and M′ are the exact mass of ssPNA and BAC-ssPNA respectively.*

Name	Sequence	Observed m/z (ion peak)	Observed mass (Da)	Calculated mass (Da)
P	NH_2-Lys-ATC AAC ACTGCA-Lys-COOH	696.7471 ($[M'+5H]^{5+}$)	3478.7355	3478.4915
		580.7830 ($[M'+6H]^{6+}$)	3478.6980	3478.4915
		497.9610 ($[M'+7H]^{7+}$)	3478.7270	3478.4915
BAC-ssPNA	BAC-NH_ε-Lys-ATC AAC ACTGCA-Lys-COOH	679.8029 ($[M+H+2Na+K]^{6+}$)	3992.7318	3992.0861
		582.8340 ($[M+2H+2Na+K]^{7+}$)	3992.7445	3992.0861
		510.1084 ($[M+3H+2Na+K]^{8+}$)	3992.7658	3992.0861
		453.5418 ($[M+4H+2Na+K]^{9+}$)	3992.7669	3992.0861
P’	Cys-TGCAGTGTTGAT-Lys	710.3474 ($[M"+5H]^{5+}$)	3546.737	3546.73
		887.6876 ($[M"+4H]^{4+}$)	3546.75	3546.73
		1183.2268($[M"+3H]^{3+}$)	3546.68	3546.73

2.1.6 NMR studies.

All NMR spectra were recorded on Bruker 400 MHz NMR Spectrometer.

2.1.7 Sample preparation.

Stock solutions of all nucleic acid constructs were prepared at 10 μM concentration by mixing all the relevant component strands (**Table 2**) in equimolar ratio in 10 mM sodium phosphate buffer, pH 7.2. Annealing was done by heating the solution at 90 °C for 5 min and cooling at the rate of 5 °C/ 15 min. All the samples were incubated at 4 °C minimum for 48 h before experiments.

Table 2 *Sequences of PNA and DNA oligomers used in this study. The sequences in same colors are complementary. The bases shown in blue are the bulge sequences.*

Name	Sequences	Description
$C1_3$	5′ GACTCACTGTTTGTCTGTCGTTCTAGGATATATATTT 3′	3′ amine-C_6 linker
C2	5′ AAATATATATCCTAGAACGACAGACAAACAG*T*GAGTC 3′	Unmodified
$C1_I$	5′ GACTCACTGTTTGTCTGTCGTT***C******T***CGGATATATAT 3′	Internal 5- aminoallyl modification on the T shown in bold and italics
$C2_{B0}$	5′ ATATATATCCGAGAACGACAGACAAACAG*T*GAGTC 3′	Unmodified
$C2_{B1}$	5′ ATATATATCCGGAACGACAGACAAACAG*T*GAGTC 3′	Unmodified
$C2_{B2}$	5′ ATATATATCCGAACGACAGACAAACAG*T*GAGTC 3′	Unmodified
$C2_{B3}$	5′ ATATATATCCAACGACAGACAAACAG*T*GAGTC 3′	Unmodified
P	BAC-NH_ε-Lys-ATC AAC ACT GCA-Lys-COOH	Sensing module: PNA strand
P′	NH_2-Lys-TGC AGT GTT GAT-Lys-COOH	Complementary PNA strand
D2	5′ TATA***T***ATA GGATCTTGCTGTCTGGTG TGC AGT GTT GAT 3′	Normalizing module: internal Alexa 647 modification on the T shown in bold and italics
D1	5′ CACCAGACAGCAAGATCC TATATATA 3′	Targeting module: Unmodified

2.1.8 Fluorescence studies.

All fluorescence studies were carried out using a Fluoromax-4 (Horiba Scientific, Japan) spectrophotometer. 10 µM stock of different nucleic acid constructs were diluted to a final concentration of 200 nM using 10 mM sodium phosphate buffer, pH 7.2 and incubated for 30 min at room temperature prior to experiments. 200 nM free Tetramethylrhodamine (TMR) was added as normalizing fluorophore to the diluted samples in absence of Alexa 647 on the complementary strands. The emission spectra of BAC and TMR or Alexa 647 were acquired by exciting the samples at 435 nm (λ_{Ex}BAC) and 540 nm (λ_{Ex}TMR) or 640 nm (λ_{Ex}Alexa 647) respectively. An emission value of 10 mM sodium phosphate buffer, pH 7.2 served as blank and was subtracted from all relevant acquired spectra. To study the chloride sensitivity of different constructs, different final [Cl^-] ranging between 5 mM to 200 mM were achieved by adding microliter aliquots from a 1M stock of NaCl to 400µL of sample. Emission intensity of BAC at 505 nm (G) was

normalized to emission intensity of TMR at 570 nm (R) or Alexa 647 at 670 nm (R). Fold change was calculated from the ratio of R/G values at two different added [Cl^-].

2.1.9 Lifetime decay measurements.

The fluorescence lifetime decay traces were acquired using TEMPRO (Horiba Jobin Yvon, Japan) with a Time Correlated Single Photon Counting (TCSPC) system. The excitation source used was a pulsed NanoLED with excitation at 443 nm at a repetition rate of 1 MHz. The emission was collected at 488 nm, and was monitored at the magic angle (54.7°) to eliminate the contribution from the decay of anisotropy. The fluorescence decay data collection was done using microchannel plate photomultiplier tube coupled to a TCSPC card at 0.11 ns per channel. The instrument response function (IRF) at 443 nm was measured using a dilute colloidal suspension of coffee whitener, and was found to be 1.23 ns (FWHM). The peak preset was set to 20,000 counts.

Fluorescence decay measurements on various constructs were carried at 1 µM concentration in 10 mM degassed potassium phosphate buffer, pH 7.2. For each fluorescence lifetime decay based titration, 2 µL aliquots of 1 M NaCl were sequentially added in batches to 100 µL of sample at 25°C.

2.1.10 Data analysis.

Fluorescence decay curves were analyzed with the associated software using a standard iterative reconvolution method, assuming a multiexponential decay function:

$$I(t) = A + \sum_{i=1}^{n} \left(B_i e^{-t/\tau_i} \right) \qquad i = 1 - 3$$

where, A is the background level (dark count of the detector), Bi is the fractional amplitude, τ_i is the fluorescence lifetime of the i^{th} decay component such that $\Sigma B_i = 1$. The quality of fit was judged

on the basis of the reduced chi-square statistic (χ^2_{red}), the randomness of residuals and autocorrelation function about the mean (Lakowicz 2006). Mean lifetime was calculated using the equation (Lakowicz 2006):

$$< \tau > = \frac{\sum_{i=1}^{n}(B_i\tau_i^2)}{\sum_{i=1}^{n}(B_i\tau_i)} \qquad i = 1 - 3$$

The Stern-Volmer constant was estimated from slope of the linear plot of τ_0/τ versus [Q],

$$\frac{< \tau_0 >}{< \tau >} = 1 + K_{SV}[Q]$$

where <τ0> is the mean fluorescence lifetime in the absence of quencher and<τ> is the mean fluorescence lifetime in the presence of quencher at a concentration [Q]. Bimolecular quenching rate constant (k_q) is given by the equation

$$k_q = \frac{K_{SV}}{< \tau_0 >}$$

2.1.11 Fluorescence Lifetime Imaging Microscopy (FLIM)

J774 macrophages (ATCC No. TIB-67) were a kind gift from Prof Deborah Nelson, Department of Pharmacological and Physiological Sciences, the University of Chicago. They were cultured in Dulbecco's Modified Eagle's Medium/F-12 (1:1) (DMEM-F12) (Invitrogen Corporation, USA) containing 10% heat inactivated Fetal Bovine Serum (FBS) (Invitrogen Corporation, USA), 100 U/ml penicillin and 100 g/ml streptomycin at 37ºC in 5% CO2, and were used at 60% confluence. 100 µM BAC-PNA in M1 buffer (pH 7.4) was pulsed for 30 min at 37ºC in J774 cells, washed with PBS, briefly fixed (2.5% PFA for 2 min) at RT and clamped at pH 5 and 5 mM Cl^- as described (Saha et al. 2015a). Confocal FLIM (Fluorescence Lifetime Imaging Microscopy) images of cells were acquired on

Nikon ISS Alba (λ_{ex} = 448 nm, λ_{em} = 530/43 nm, frequency modulation of 20-140 MHz with peak counts of ~1000). Identical images were obtained from unlabeled J774 cells.

2.2 Results and discussion

In order to build a chloride sensitive device that can be targeted to a specific organelle, we chose to conjugate it to DNA (Modi et al. 2013). This DNA nanodevice would be able to quantitate resting chloride in the target organelle as it would comprise a chloride sensitive fluorophore and a normalizing fluorophore. Given that the nanodevice would be comprised of two complementary strands bearing each of these fluorophores, this would result in a reporter system that would be monodisperse in bulk, with a 1:1 ratio of the reporter and normalizer fluorophores. Such monodispersity is key to accuracy in quantitation of sub-cellular chloride in living systems.

We chose as our chloride reporter BAC (Figure 7 a), a quinolium-based dye, well-known to undergo collisional quenching in presence of chloride (Sonawane et al. 2002). Such quinolium-based chloride indicators have good sensitivity and rapid response (<1 msec) to changes in Cl^- concentration (Geddes 2001). Even though BAC is sensitive to collisional quenching by all halides (Huber et al. 1999), concentration of other halides (F-, Br- and I-) and pseudo halides (CN-, SCN- and azide) in biological systems combined is less than 1% the value of chloride (Sener et al. 2007; Olszowy et al. 1998; Gbadebo and Nwufoh 2010; Paul and Smith 2006; Spectrometry et al. 2000). Hence, in living systems, BAC predominantly behaves like a chloride sensor (Sonawane et al. 2002). This sensor is designed to act as a chloride sensor only in living systems and NOT for other applications like environmental remediation. Importantly, they are insensitive to physiological changes in pH. BAC was chosen due to its long excitation and emission wavelengths relative to other quinolinium based reporters (Geddes 2001; Huber et al. 1999; C D Geddes et al. 2001).

Further, BAC has been used to quantitate chloride in endosomes, albeit with much lower accuracy (Sonawane et al. 2002).

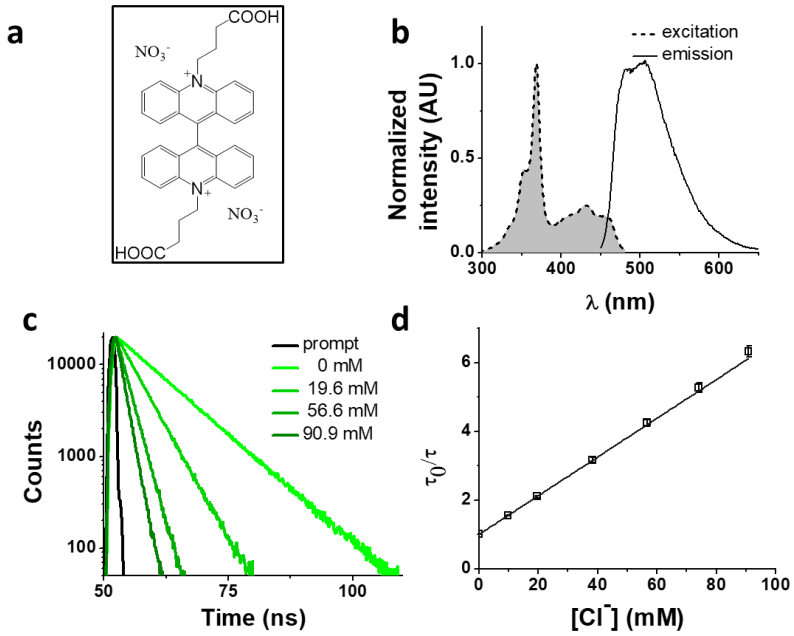

Figure 7 *Photophysical properties of BAC (10,10'-bis[3-carboxypropyl]-9,9'-biacridinium dinitrate). (a) Chemical structure of BAC. (b) Excitation and emission spectra (λex = 443 nm) of BAC. (c) Representative fluorescence lifetime decay traces of 1 µM BAC in 10 mM potassium phosphate buffer, pH 7.2 various chloride concentrations (λex = 443 nm, λem = 488 nm, RT). (d) Stern-Volmer plot for BAC. Error bars indicate the mean of three independent experiments ± s.e.m.*

2.2.1 BAC synthesis and characterization

BAC shows a mono-exponential fluorescence decay in 10 mM potassium phosphate buffer (pH 7.2) with a lifetime of 9.15 ns (***Table 3***). It has a reasonably good sensitivity towards chloride with a K_{SV} of 56.4 M^{-1} and k_q of 6.16 $ns^{-1}M^{-1}$. K_{SV} values obtained from fluorescence quenching experiments reveal overall sensitivity of fluorophore to quencher, while the k_q values give information about rate of diffusion of quencher around sensing dye. The lower value of k_q compared to diffusion limited rate (10 $ns^{-1}M^{-1}$) is likely due to the two negatively charged carboxyl groups shielding the positively charged core of the dye, thereby reducing the efficiency of collisional quenching by negatively charged chloride ions (Ando and Asai 1980). In fact, it has

been reported that synthetic analogues of BAC show different values of k_q depending upon the nature of the charge on the side chain (Huber et al. 1999).

2.2.2 Effect of conjugation to DNA

Previously, it has been shown that due to the presence of the negatively charged phosphate backbone, DNA nanodevices act as anionic ligands and are internalized by Drosophila hemocytes that express the ALBRs (Anionic Ligand Binding Receptors) (Modi et al. 2009; Surana et al. 2011). Our laboratory has also demonstrated a general strategy to target DNA nanostructures, carrying a specific dsDNA sequence $d(AT)_4$ to probe the ionic environment of the lumen of endocytic organelles (Modi et al. 2013).

In order to achieve targeted intracellular chloride sensing in a specific organelle of interest, we conjugated BAC to single stranded DNA at the 3′ end via a flexible hexamethylene linker using hydroxysuccinimide chemistry (BAC-ssDNA, Figure 6a). Upon conjugation, the fluorescence intensity of the dye as well as its sensitivity towards chloride reduced (***Table 3***).

This reduction in fluorescence intensity as well as lifetime upon conjugation to DNA is due to Photoinduced Electron Transfer (PET) from guanine to fluorophore (Johnson et al. 2003; Sauer, M, Drexhage,K.H., Lieberwirth,U., Muller,R., Nord,S., Zander 1998; Seidel et al. 1996) that is dependent upon the relative redox potentials of the dye and nucleobase (Seidel et al. 1996). The energetics and feasibility of this electron transfer process, described by the Weller's equation (Lewis and Letsinger 1998) indicates that guanine is mainly responsible for PET based quenching by nucleobases (Seidel et al. 1996). The efficiency of PET from guanine reduces logarithmically with increasing distance (Lewis and Letsinger 1998).

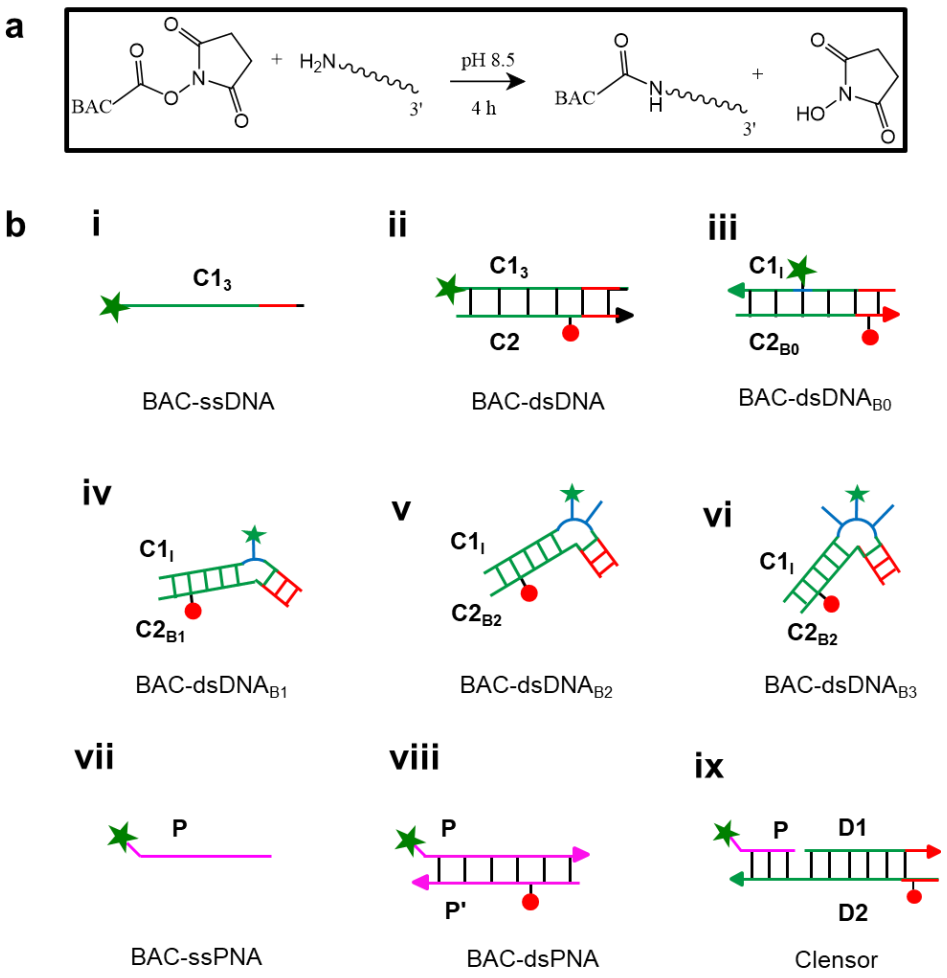

Figure 8 *Nucleic acid constructs used in the study. (a) Reaction scheme for chemical conjugation of BAC to amine labeled DNA. (b) Schematic showing structures of different chloride sensing nucleic acids constructs. BAC: green filled star; Alexa 647: red filled circle.*

We observed a similar trend in fluorescence lifetime where we observed bi-exponential decay with lifetime values of 5.5 ns (98%) and 13.9 (2%) (***Table 3*** and

Table 4). BAC-ssDNA incorporates 18% guanine residues where the first guanine is located 10 nt apart from the BAC labeled 3′ end (**Table 2**). Given that the persistence length of ssDNA is only 3 bases (Murphy et al. 2004), potentially BAC-ssDNA can collapse into a globular conformation bringing the guanine residues significantly nearer to BAC. Therefore, we assigned the 5.5 ns component to this quenched state of BAC that has 98% relative contribution to the total fluorescence intensity (***Table 3***). The reduction in the lifetime value of the major component accounts for the reduction of fluorescence intensity.

This pre-quenched state of BAC with 5.5 ns lifetime exhibited 40% reduction in chloride sensitivity showing a K_{SV} value of 33.56 M^{-1} compared to free BAC (K_{SV} = 56.4 M^{-1}) (***Table 3***). The k_q value remained unaffected upon conjugation to DNA indicating that the negatively charged DNA backbone provides similar level of shielding as that of two carboxylate groups, and hence negligible change in chloride diffusion around BAC-ssDNA.

In order to understand the nature of the longer lifetime component observed for BAC-ssDNA, we determined the fluorescence lifetime of free BAC in the presence and absence of excess dsDNA (***Figure 10*** and ***Table 3***). When dsDNA was added to a solution containing free BAC, the observed fluorescence decay (***Table 3***) yielded a tri-exponential decay model as the best fit to the data with decay components of 5.7, 9.1 and 13.5 ns. The 13.5 ns component proved to be insensitive to chloride quenching, indicating that this lifetime originates due to association of BAC with dsDNA. Spectroscopic studies have shown that lucigenin, the parent molecule of BAC, intercalates efficiently into the DNA double helix (Wu et al. 2002). Electrostatic interaction between cationic lucigenin and the polyanionic DNA play a crucial role in the propensity of lucigenin to intercalate in dsDNA (Wu et al. 2002). It is well known that intercalated lucigenin is also less sensitive to quenching by chloride. Free BAC is also expected to intercalate into dsDNA analogous to its parent

molecule lucigenin and show an increased lifetime because of hindered movement. In fact, fluorescence lifetimes of other fluorophores like ethidium bromide and acridine orange increase to 1400% and 300% respectively upon binding dsDNA (Johnson et al. 2003), and are also considerably less sensitive to quenching due to inaccessibility (Suh and Chaires 1995). However, the bound form of BAC with 13.5 ns lifetime represents only 1% population in contrast to 98% for ethidium bromide and 88% for acridine orange indicating a weaker interaction (Johnson et al. 2003).

Closer scrutiny of the excitation spectra of BAC-ssDNA and BAC-dsDNA, revealed that intensity of 443 nm band was reduced, while that of 392 nm was increased (Figure 1-4a). We observed similar trends in the emission spectrum of BAC-dsDNA, where we observe a blue shifted emission at 425 nm along with the normal emission (Figure 1-4a), that is contrary to most cases where intercalation or groove binding of a dye leads to small red shift in its absorption spectrum (Suh and Chaires 1995). The nature of molecular interaction responsible for this is as yet unclear, but it is worth mentioning that blue shifts usually occur when the dye interacts with single stranded oligonucleotide (Timtcheva et al. 2000) or because of reduced solvation (Merrill et al. 1993; Vivian and Callis 2001). In order to check whether BAC is solvent accessible, we titrated BAC-ssDNA against chloride and observed a significant population (27 %) that was insensitive to quenching at 392 nm excitation (Figure 10d), indicating that it is indeed solvent inaccessible. On the other hand, almost the entire population (98 %) is sensitive to chloride at 443 nm excitation (***Table 3***). This indicates that 392 nm excites the insensitive form which has a blue shifted excitation with respect to the free dye. Notably, the reduction in sensitivity due to DNA binding is negligible when excited at 443 nm because the emission arising from it is blue shifted (Figure 10c), and hence, has a meagre contribution towards total population (2%). But as we have observed

using 392 nm excitation, a significant population is insensitive to quenching because of ssDNA binding, which is an indicator of an inefficient sensor.

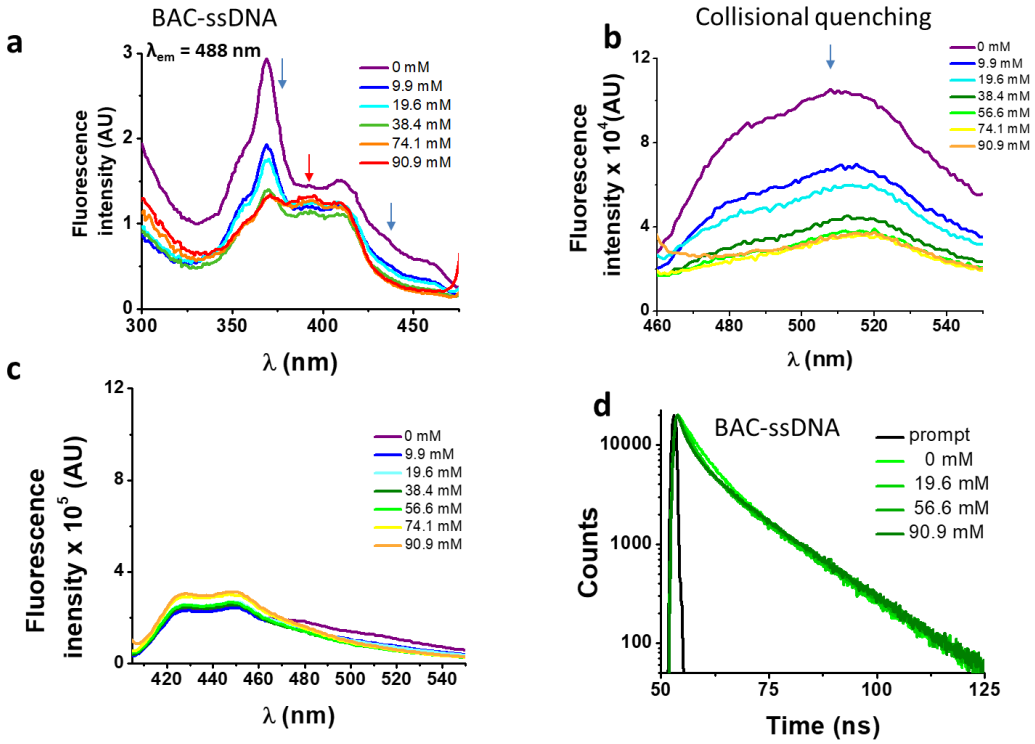

Figure 9 *Photophysical properties of BAC in BAC-ssDNA. (a) Excitation spectra of 1 µM BAC-ssDNA ($C1_I$) at different chloride concentrations. Emission spectra at (b) λ_{ex} = 443 nm and (c) λ_{ex} = 392 nm. (d) Representative fluorescence lifetime decay traces of 1 µM BAC-ssDNA in 10 mM potassium phosphate buffer, pH 7.2 at various chloride concentrations (λ_{ex} = 392 nm, λ_{em} = 488 nm).*

2.2.3 Effect of DNA structure

The ability of guanine to quench fluorophores strongly depends on its hydrogen bonding state and its position within the double-stranded structure (Nazarenko et al. 2002). It has also been shown that depending on sequence, a fluorescein labeled oligo undergoes dequenching upon hybridization. Duplexes containing dA-T base pairs adjacent to covalently labeled fluorophores show 14% higher fluorescence intensities compared to their single stranded forms (Nazarenko et al. 2002). Therefore, to study the effect of duplexation on the chloride sensitivity of BAC, BAC-

ssDNA was hybridized to oligo C2 to form BAC-dsDNA and carried out fluorescence measurements. Upon comparison of the excitation and emission spectra of BAC-dsDNA with that of BAC-ssDNA, we observed that intensity of 443 nm band had recovered, while that of 392 nm had reduced (Figure 9a) indicating a reduction in the DNA-complexed - likely intercalated - form of BAC. We expected BAC-dsDNA to show higher fold change in R/G or higher chloride sensitivity than BAC-ssDNA due to relief of quenching as the 3′ end of BAC-ssDNA is highly rich in AT. In contrast, BAC-dsDNA showed negligible increase in chloride sensitivity (***Table 3***). Thus, based on fluorescence intensity and lifetime data, we may conclude that the reduced chloride sensitivity of BAC in BAC-ssDNA is primarily due the prior quenching of BAC by guanine residues (Sauer, M, Drexhage,K.H., Lieberwirth,U., Muller,R., Nord,S., Zander 1998; Nazarenko et al. 2002). Additionally, the complexation or intercalation of BAC into either dsDNA or any secondary structure formed by ssDNA might also restrict the accessibility of BAC to chloride thereby decreasing the chloride sensitivity.

Next, we sought to understand whether there was any positional effect of BAC attachment on the DNA scaffold or effect of linker flexibility on chloride sensitivity of BAC. Therefore, we chose oligo C1I, where BAC is internally conjugated to T24 using a rigid 5-aminoallyl linker. The internally labeled oligo C1I was hybridized to $C2_{B0}$ to form BAC-dsDNA_{B0} (Figure 8 iii). Moreover to minimize groove binding of BAC into nearby base pairs as well as to understand the effect of flanking base pairs on chloride sensitivity of BAC, we designed bulges different sizes around the point of BAC attachment (T24) by changing the complementary sequence as shown in Figure 11. In case of BAC-dsDNA_{B1}, an unopposed T24 residue, flanked by C residues is known to remain extrahelical (Kalnik et al. 1990) and hence is expected to position BAC away from helical region. However, the conformation adopted by multiple pyrimidines comprising the bulge

for BAC-dsDNA$_{B2}$ (dCdT) and BAC-dsDNA$_{B3}$ (dCdTdC) is not described (Rosen et al. 1992) although increase in bulge size is known to enhance the conformational flexibility of the bulged nucleotides (Dornberger et al. 1999).

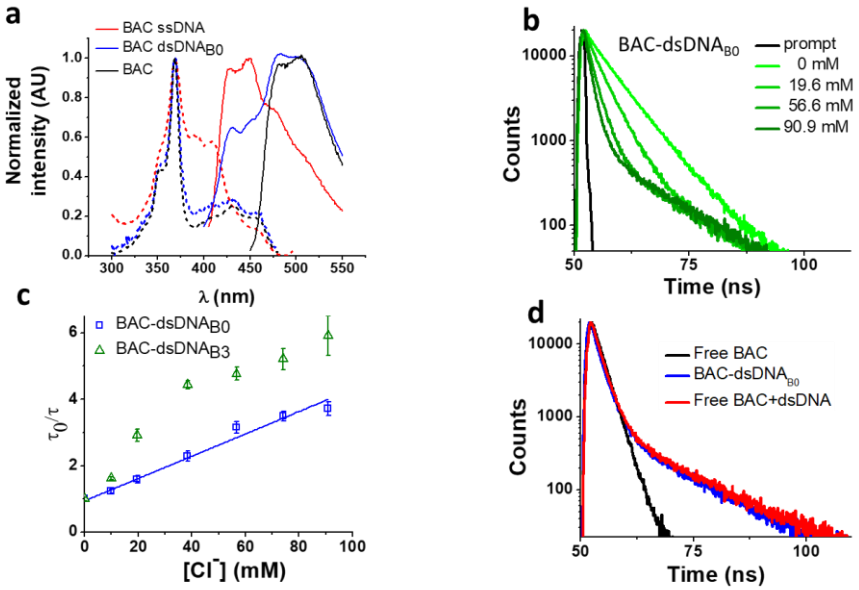

Figure 10 *Interaction of BAC with DNA (a) Comparison of excitation and emission spectra of free BAC, BAC-ssDNA and BAC-dsDNA$_{B0}$. (b) Representative fluorescence lifetime decay traces of 1 µM BAC-dsDNA$_{B0}$ in 10 mM potassium phosphate buffer, pH 7.2 at various chloride concentrations (λ_{ex} = 443 nm, λ_{em} = 488 nm). (c) Stern-Volmer plots for BAC-dsDNA$_{B0}$ and BAC-dsDNA$_{B3}$. Average lifetime (τ_{Avg}) of the sensitive components has been used to plot Stern-Volmer plot. Error bars indicate the mean of two independent experiments ± s.e.m. (d) Representative fluorescence lifetime decay traces of 1 µM BAC-dsDNA$_{B0}$, BAC and 2 µM BAC + 1.5 mM$_b$ dsDNA in 10 mM potassium phosphate buffer (pH 7.2) at 60 mM chloride (λ_{ex} = 392 nm, λ_{em} = 488 nm).*

We therefore determined the chloride sensitivity of BAC when incorporated internally into the above designed bulges in DNA assemblies using fluorescence intensity based chloride titrations (***Table 3***). All the internally labeled constructs showed similar fold changes in R/G (1.2-1.5) with their single stranded forms indicating no significant effect of bulge positioning using a rigid linker on the chloride sensitivity of BAC. To investigate the chemical environment of BAC in these bulge-labeled scaffolds, we determined fluorescence lifetimes in the absence (BAC-dsDNA$_{B0}$) and presence of a pyrimidine-rich (BAC-dsDNA$_{B3}$) bulge around the BAC label (T24). BAC-dsDNA$_{B0}$

showed complex multi-exponential fluorescence decay with components of 1.3, 5.8 and 13 ns (***Table 3***). We can assign the 13 ns lifetime component to the intercalated or complexed state of BAC, while 1.3 ns and 5.8 ns as quenched states as seen from BAC-ssDNA (***Table 3***). However the relative contributions of these forms are now altered as we go from BAC-ssDNA to BAC-dsDNA$_{B0}$. Here, the 1.3 ns component corresponds to a population (38%) of BAC that is more efficiently quenched by the three guanine residues within 4 nt on either side of the dye. In fact, for a dye like fluorescein, positioning the fluorophore internally leads to far more efficient quenching than when positioned at the 5′ or 3′ terminus (Nazarenko et al. 2002).

Both, BAC-dsDNA$_{B1}$ as well as BAC-dsDNA$_{B2}$ showed complex multi-exponential fluorescence decay (***Table 3***). We observed considerable reduction in fluorescence lifetime, K_{SV} and k_q compared to BAC-dsDNA$_{B0}$. With the introduction of a bulge, the accessibility of chloride to BAC is reduced as much as 3-4 fold (Heinlein et al. 2003). BAC-dsDNA$_{B2}$ and BAC-dsDNA$_{B3}$ shows only an ~33% and 54% improvement respectively in fluorescence lifetime compared to that of BAC-dsDNA$_{B1}$ indicating that increasing the bulge size does little to improve the sensitivity of BAC to chloride.

BAC-dsDNA$_{B3}$ also showed similar complex multi-exponential fluorescence decay with components of 1.3, 7.8 and 14.5 ns (***Table 3***). It is known that bulge structures significantly affect the local geometry of DNA and RNA duplexes (Lilley 1995). Diverse biophysical experiments such as electrophoretic mobility (Bhattacharyya and Lilley 1989; Bhattacharyya et al. 1990) FRET (Gohlke et al. 1994), electron microscopy (Wang et al. 1992) and NMR (Rosen et al. 1992) suggest that bulges introduce a defined kink into the helical axis of the DNA and RNA molecules. The magnitude of helix bending depends on the size and the sequence of the bulge (Wang and Griffith 1991; Zacharias and Hagerman 1995). Purine bulges generate greater helical bending than

pyrimidine bases (Wang and Griffith 1991). FRET efficiency are very similar for both DNA and RNA helices containing bulges, indicating a similar kinking process despite the geometrical differences between DNA and RNA helices (Gohlke et al. 1994). The estimated bend angle for UUU bulge is 55° (Zacharias and Hagerman 1995). Molecular modelling based on NMR data indicated that the angle of bending at the bulge site ranges between 50° and 60° in the direction away from the bulge containing strand for an ATA bulge (Rosen et al. 1992). Further a significant reduction in helical twist was also observed due to insertion of three nucleotide bulge (Rosen et al. 1992).

We considered a 55° bend angle for BAC-dsDNA_{B3} to calculate relative change in distance between BAC and the nearby guanine residues upon bulge insertion. To calculate the minimum distance we did not incorporate any helical twist in the calculation. In this case, the distance between BAC and the nearest guanine residue (one nucleotide away from T24) on the 3′ increases from 15.2 Å to 19.9 Å (Figure 11). Similarly the distance between BAC and the nearest guanine residue (three nucleotides away from T24) on the 5′ side increases from 19.2 Å to 26.6 Å. The new component with 7.8 ns lifetime likely reflects the reduced quenching efficiency by guanine because of the greater distance between BAC and its neighboring guanines due to bending caused by introduction of the bulge (Sauer, M, Drexhage,K.H., Lieberwirth,U., Muller,R., Nord,S., Zander 1998). However, due to the small percentage of this population (11%), the overall chloride sensitivity of BAC remains poor. The major population (85%) has a short lifetime of 1.3 ns indicating a conformer with highly efficient quenching by guanine present at the edge of the bulge. This implies that for the majority of time, BAC in this conformer prefers accommodation within the bulge, where it interacts strongly with the nucleobases and the backbone. Fluorescence lifetime based chloride titration of BAC-dsDNA_{B0} and BAC-dsDNA_{B3} revealed that the 14.5 ns lifetime

species was again present as the chloride insensitive bound/intercalated form. Lastly, the intrinsic structural dynamics of the dsDNA backbone yields non-linearity in the Stern Volmer plot of BAC-dsDNA$_{B3}$ (Figure 9c), for chloride concentrations > 40 mM and this portion was not considered for analysis.

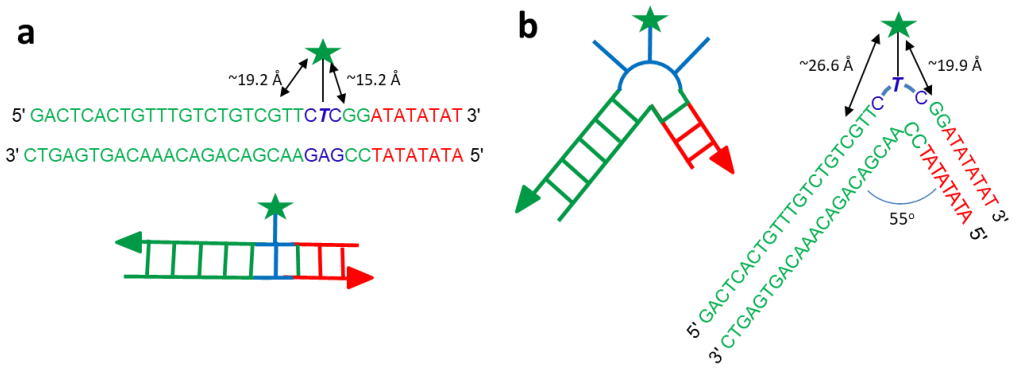

Figure 11 *Secondary structure of BAC-dsDNA constructs. Schematic showing structures and calculated distances between BAC and guanosine residues in different nucleic acid assemblies used in this study. (a) BAC-dsDNA$_{B0}$ (b) BAC-dsDNA$_{B3}$. We have the aminoallyl linker to be rigid, in the all-trans form and positioning BAC in the plane of the paper, bisecting the angle made by helix axes of the constituent helical domains.*

Cumulatively, DNA assemblies carrying an internal BAC label exhibit two types of quenched states depending on the quenching efficiency of the guanine residues (***Table 3***). The efficiency of quenching by guanine residues and relative contributions of both quenched states depends on the geometry around the internal fluorophore label. Importantly, a chloride insensitive 14 ns component was constantly observed in all three dsDNA constructs independent of fluorophore position, linker flexibility and nature of base pairs in the proximity, which correlates well with a form of the fluorophore that is bound/intercalated with DNA. Importantly, we do not observe any component with lifetime comparable to that of free dye, indicating a strong interaction between DNA and BAC; observed as (i) PET based quenching and (ii) dsDNA intercalation.

2.2.4 Effect of an electrically neutral backbone

An ideal chloride reporter should have a high fluorescence intensity as well as high chloride sensitivity. It is known that quenching efficiency of I^- decreases with increase in negative charge on the fluorophore due to the repulsion between the quencher and the negative charge on the fluorophore (Ando and Asai 1980). Increase in ionic strength compensates this by shielding the negative charge on the fluorophore. Accordingly, conjugation of BAC to DNA not only reduces its fluorescence intensity, but also its sensitivity towards collisional quenching by chloride. Thus, we hypothesized that the negatively charged DNA backbone attracts the positively charged quinolinium core of BAC and this proximity to DNA enhances quenching of BAC by nucleobases resulting in reduced chloride sensitivity (Suh and Chaires 1995; Merrill et al. 1993; Marras et al. 2002).

Electrostatic interactions are a primary contributor to fluorophore-DNA interactions (Wittung et al. 1994). We reasoned that eliminating these electrostatic interactions, would yield an assembly with higher chloride sensitivity. We therefore covalently linked BAC to a PNA oligomer because it has a neutral backbone (BAC-ssPNA). Peptide nucleic acids are remarkable DNA/RNA mimics in which the sugar–phosphate backbone of the DNA/RNA is replaced by a synthetic peptide backbone formed from N-(2-aminoethyl)-glycine units (Nielsen and Haaima 1997; Nielsen et al. 1991). The plot of R/G vs. $[Cl^-]$ showed 1.8 fold change in R/G compared to 1.2 observed for BAC-ssDNA (***Table 3***) indicating an increased chloride sensitivity of BAC upon conjugation to PNA. Next to study the effect of hybridization, BAC-ssPNA was hybridized to P′ to form BAC-dsPNA (Figure 8 viii). Upon hybridization, the fold change in R/G values increased to 2.7 which is indeed comparable to fold change observed for free BAC.

Fluorescence lifetime experiments were carried out to ascertain the mechanism of improvement of chloride sensitivity upon conjugation to PNA. BAC-ssPNA showed a biexponential fluorescence decay with components of 4.3 and 8.4 ns (***Table 3***). The sequence of P contains 8% guanine residues (**Table 2**). Neutral polymers are known to collapse into dense spherical globules in order to reduce unfavorable solvent polymer interactions and charged polymers show a higher radius of gyration (Dobrynin 2008). Further given its neutral backbone and much higher conformational flexibility of BAC-ssPNA, compared to ssDNA the average proximity of guanine is likely to be much shorter in random coiled BAC-ssPNA. Therefore, we assign 4.3 ns lifetime component as the guanine quenched population of BAC due to PET. However, 59% of BAC remained unaffected resulting in a 8.4 ns lifetime that is comparable to free BAC (9.2 ns), indicating weakened interaction between PNA and BAC compared to DNA and BAC. BAC-dsPNA also showed two components with 5 ns and 9.2 ns lifetimes (***Table 3***) indicating that a major population of BAC is in same environment as free BAC. This reinforces that there is some quenching of BAC due to the DNA scaffold itself, before the addition of chloride, which is responsible for the lower chloride sensitivity in BAC-ssDNA and BAC-dsDNA.

Interestingly, BAC-ssPNA and BAC-dsPNA did not show the 14 ns lifetime component. It is known that the propensity of EtBr to intercalate reduces drastically as DNA-DNA> DNA-PNA> PNA-PNA (Wittung et al. 1994). Fluorescence lifetime based chloride titrations of BAC-ssPNA and BAC-dsPNA showed K_{SV} values slightly better than that of the free BAC (***Table 3***). The 42% and 47% increase in observed k_q value for BAC-ssPNA and BAC-dsPNA respectively indicate higher diffusion rate of chloride in this medium than that of BAC-ssDNA. This is consistent with the negative charge due to DNA surrounding BAC in BAC-ssDNA restricts chloride diffusion rate, and is partially responsible for reduction in chloride sensitivity of DNA-based assemblies.

2.2.5 Clensor

To combine the dsDNA specific intracellular targeting and increased chloride sensitivity based on our previous observation, we designed a scaffold consisting of three nucleic acids oligomers, that we call *Clensor*. In *Clensor*, BAC has been covalently conjugated to the N-terminus of ssPNA using hydroxysuccinimide chemistry to give BAC ssPNA. BAC ssPNA has then been hybridized to its complementary DNA stand to form a DNA-PNA hybrid duplex. PNA oligonucleotides containing purine and pyrimidine nucleobases hybridize with complementary DNA and RNA strands to form right-handed, double-helical complexes according to the Watson–Crick rules of hydrogen bond mediated base pair formation (Egholm et al. 1993; Eriksson and Nielsen 1996). The hybrid duplexes formed by PNA with DNA generally have higher thermal stabilities than their duplex DNA counterparts (Chakrabarti and Schwarz 1999). They show unique ionic strength effects because the PNA strand does not bear negatively charged phosphate groups. Examination of the PNA/DNA hybrid structure by NMR spectroscopy reveals a unique double helical conformation that has features of both A and B-form DNA (Eriksson and Nielsen 1996).

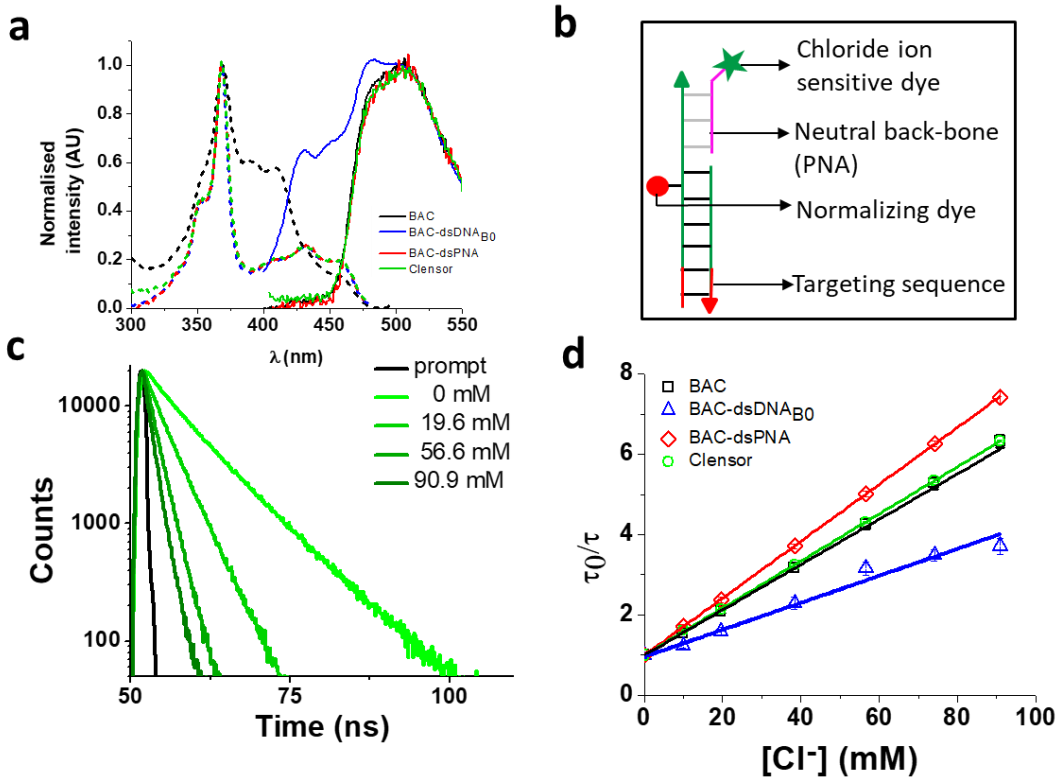

Figure 12 *Photophysical properties of Clensor. (a) Comparison of excitation and emission spectra of BAC, BAC-dsDNA$_{B0}$, BAC-dsPNA and Clensor. (b) Schematic of Clensor. (c) Representative fluorescence lifetime decay traces of 1 μM Clensor in 10 mM potassium phosphate buffer, pH 7.2 at various chloride concentrations (λex = 443 nm, λem = 488 nm). (d) Stern-Volmer plots for BAC, BAC-dsDNA$_{B0}$, BAC-dsPNA and Clensor. Average lifetime has been used to evaluate K_{SV} and k_q. Error bars indicate the mean of three independent experiments ± s.e.m.*

Clensor is composed of three modules: a sensing module (P), a normalizing module (D2) and a targeting module (D1) (Figure 8 ix and Figure 12b). The sensing module, P is a 12 mer peptide nucleic acid (PNA) oligomeric sequence conjugated to BAC. The normalizing module, D2 is a 38 nt DNA sequence carrying an Alexa 647 fluorescent label that is Cl^- insensitive. The targeting module, D1, is a 26 mer DNA sequence. P and D1 are hybridized to adjacent sites on D2 as shown in Figure 8 ix and Figure 12b. The dsDNA domain on *Clensor* comprising D1 and D2 functions as a negatively charged ligand for the ALBRs (Anionic Ligand Binding Receptors)(Saha et al. 2015a) and harbors the $d(AT)_4$ sequence required for targeting of the sensor.(Modi et al. 2013)

Clensor showed 1.8 fold change in R/G in the physiological range of chloride concentration when subjected to fluorescence quenching by addition of NaCl (***Table 3***). It showed 33% improvement in R/G fold change compared to BAC-dsDNA_{B0}. However 33% decrease in R/G fold change of *Clensor* compared to BAC-dsPNA can be explained by the presence of the negatively charged DNA backbone in the hybrid. Fluorescence lifetime experiments on *Clensor* revealed two components with 4.0 ns and 8.3 ns lifetime, as observed as BAC-ssPNA (***Table 3***). However, their relative contributions are different from BAC-ssPNA. The increase in relative contribution of the 8.4 ns component with from 59% to 65% is probably due to the relief of quenching effect upon hybridization. Again, no bound/intercalated population of BAC corresponding to 14 ns was observed in *Clensor* as expected. Fluorescence lifetime based chloride titration revealed a K_{SV} value of 58.6 M^{-1} that is comparable with free BAC indicating a similar sensitivity of BAC to quencher (***Table 3***). However, the 29% increase in k_q value indicates that negatively charged DNA backbone of the hybrid duplex is responsible for the lower diffusion rate of chloride. ***Table 3*** summarizes the photophysical properties and sensitivities of various constructs. However, there is a slight mismatch between the intensity fold change and lifetime fold change possibly because insensitive component has been excluded from the calculation for lifetime fold change; but overall trend seems to be conserved.

Table 3 *Summary of photophysical properties of constructs. Fluorescence lifetimes (τ_0), their relative populations (shown in brackets), average lifetime ($\tau_{0\ avg}$), Stern-Volmer constant (K_{SV}), bimolecular quenching rate constant (k_q) and fold change observed for various versions of nucleic acid based chloride sensors. Insensitive component is shown in bold. * Fold change in τ_{avg}, ** Fold change in fluorescence intensity from 24.4 – 90.9 mM [Cl^-]*

Construct	τ_0 (ns)	$\tau_{0\ avg}$ (ns)	K_{SV} (M^{-1})	k_q ($M^{-1}ns^{-1}$)	Fold change*	Fold change**	χ^2_{red}
BAC	9.15 ± 0.01	9.15 ± 0.01	56.4 ± 0.6	6.16 ± 0.07	2.60	2.89	1.00
BAC-ssDNA	5.47 ± 0.25 (98 ± 1), **13.94 ± 0.42 (2 ± 1)**	5.47 ± 0.25	33.56 ± 0.76	6.13 ± 0.41	2.22	1.24	1.03
BAC-dsDNA$_{B0}$	1.27 ± 0.2 (38 ± 11), 5.78 ± 0.08 (60 ± 10), **13.00 ± 0.13 (2 ± 1 %)**	5.16 ± 0.19	33.6 ± 1.78	6.52 ± 0.59	2.27	1.21	0.98
BAC-dsDNA$_{B1}$	1.1 ± 0.08 (74 ± 0) 4.43 ± 0.21 (16 ± 0) **13.5 (9 ± 1 %)**	2.68 ± 0.11	3.9 ± 0.5	1.45 ± 0.45	1.3	1.3	1.04
BAC-dsDNA$_{B2}$	1.1 ± 0.08 (44 ± 10) 4.44 ± 0.04 (35 ± 7) **13.5 (22 ± 2 %)**	3.57 ± 0.26	7.7 ± 1.1	2.15 ± 0.23	1.3	1.3	0.98
BAC-dsDNA$_{B3}$	1.29 ± 0.1 (85 ± 2), 7.79 ± 0.19 (11 ± 1), **14.51 ± 0.12 (3 ± 1 %)**	4.17 ± 0.11	ND	ND	ND	1.27	0.97
BAC + free dsDNA	9.11 ± 0.5 (69.6 %) 5.72 ± 0.76 (29.4 %) **13.5 ± 0.45 (1 %)**	8.4	56.1	6.68	NA	NA	0.94
BAC-ssPNA	4.34 ± 0.17 (41 ± 2), 8.44 ± 0.11(59 ± 2)	7.35 ± 0.06	64.3 ± 1.1	8.74 ± 0.22	2.68	1.82	0.98
BAC-dsPNA	5.02 ± 0.14 (47 ± 3), 9.17 ± 0.17 (53 ± 3)	7.80 ± 0.08	70.8 ± 0.2	9.02 ± 0.11	2.72	2.72	1.01
Clensor	3.9 ± 0.03 (35 ±1), 8.3 ± 0.01(65 ± 1)	7.40 ± 0.01	58.6 ± 0.3	7.92 ± 0.05	2.61	1.82	0.97

Table 4 *Residuals and autocorrelation for lifetime data fitting. Comparison of the residuals (green) and autocorrelation (blue) obtained for the fits to the experimental fluorescence lifetime decay traces of free BAC, BAC-ssDNA, BAC-dsDNA$_{B0}$ (at 90.9 mM chloride) and BAC-ssPNA. All residuals correspond to 0 mM chloride unless otherwise mentioned.*

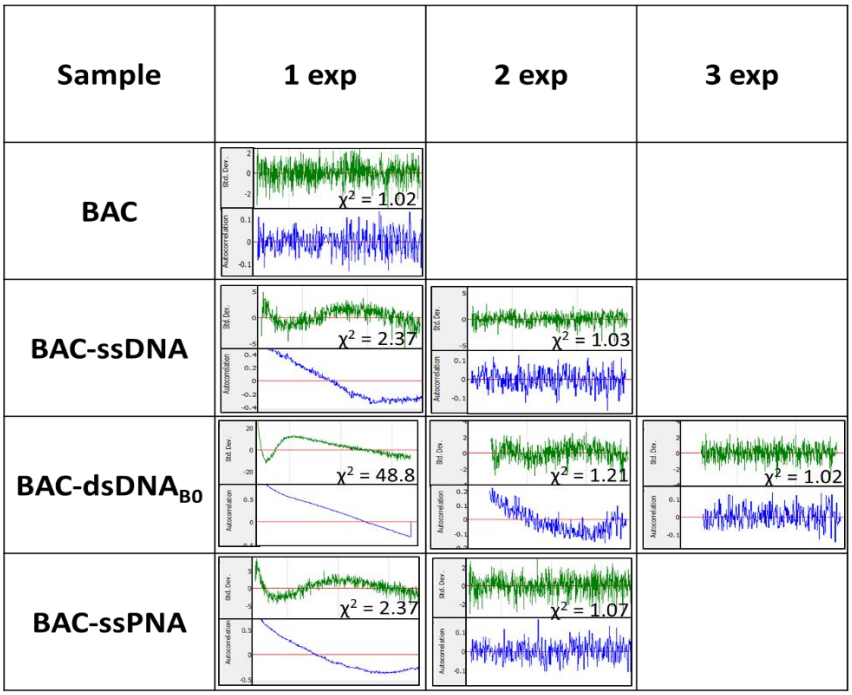

2.2.6 Fluorescence Lifetime Imaging Microscopy

A combination of fluorescence lifetime measurement and confocal microscopy is a very powerful tool to investigate biological systems. Fluorescence Lifetime Imaging Microscopy (FLIM) provides an opportunity to overcome typical pitfalls that conventional ratiometric microscopy faces. For example, FLIM is independent of dye concentration, scattering, photobleaching, etc. and gives an opportunity for multiplexed imaging as it can distinguish same color fluorophores based upon of their fluorescence lifetimes. We were able to distinguish fluorescence signal of BAC-PNA from that of autofluorescence in the same channel by mapping long lived fluorescence lifetime component (***Figure 13*** and ***Table 5***). Even though BAC shows dramatic fold change in fluorescence lifetime upon chloride based quenching, it is not suitable for FLIM due to intrinsically

very low fluorescence signal. A chloride sensitive dye with brighter fluorescence intensity may prove to be a suitable candidate for such studies.

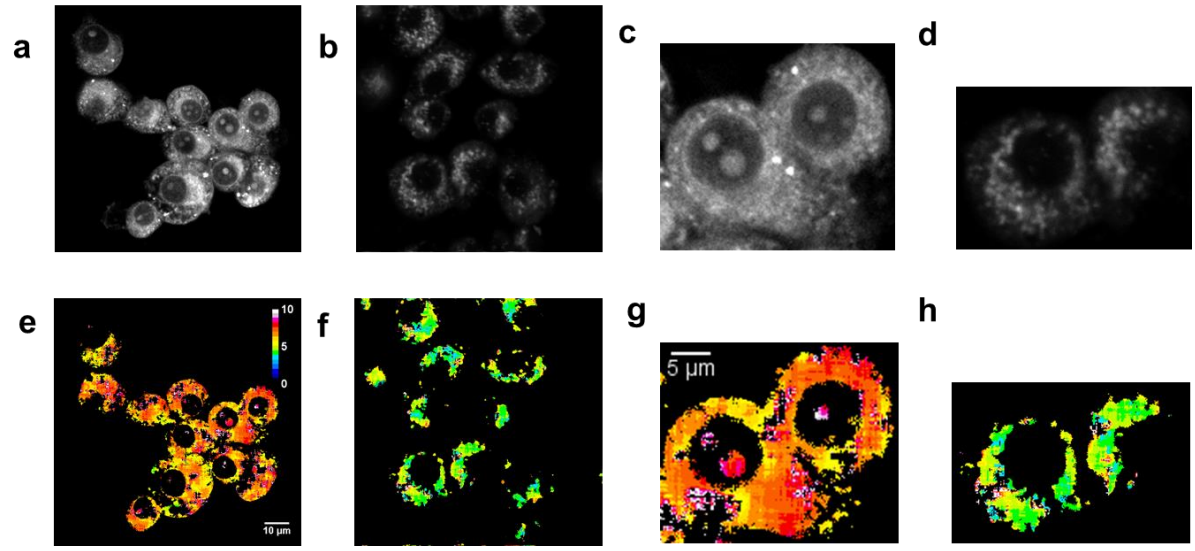

Figure 13 *FLIM using BAC-PNA. Comparison of J774 cells labeled with BAC-PNA (100 µM) and Unlabeled cells clamped at 5 mM Chloride and pH 5. a, Raw fluorescence intensity for BAC-PNA labeled cells. b, Raw fluorescence intensity for unlabeled cells. c, Zoom in of a. d, Zoom in of b. e, long fluorescence lifetime component for BAC-PNA labeled cells. scale bar 10 µm. f, long fluorescence lifetime component for unlabeled cells. g, Zoom in of c. scale bar 5 µm. h, Zoom in of d.*

Table 5 *FLIM of BAC-ssPNA. Comparison fluorescence lifetimes of BAC-PNA and autofluorescence clamped at 5 mM Chloride and pH 5.*

Sample	Individual lifetime components and populations	Average lifetime (ns)
In vitro BAC-PNA	2.1 ± 1.6 (47 ± 21), **7.3 ± 0.5** (53 ± 21)	7.0 ± 0.3
In cellulo BAC-PNA	1.4 ± 0.7 (76 ± 6), **6.7 ± 1.1** (24 ± 6)	4.9 ± 0.8
Autofluorescence	1.3 ± 0.4 (27 ± 9), **4.5 ± 0.7** (73 ± 9)	3.2 ± 0.4

2.3 Conclusions

The goal of this study was to merge the reporter capabilities of an organic dye like BAC with the programmability of the DNA scaffold. Using various photophysical studies, we have described the rational design of a nucleic acid scaffold that successfully integrates the chloride sensing ability of an organic dye. This turns out to be non-trivial, as the functionality of such ion-based fluorescent reporters becomes highly compromised upon chemical conjugation to a DNA architecture. In

previous studies, it has been also shown that the fluorescence of BAC was quenched by nearly 90% upon conjugation to proteins, despite the introduction of long spacers (Sonawane and Verkman 2003). It is also known that the chloride sensitivity of quinolinium-based chloride indicators decreases upon conjugation to dextran due to limited accessibility of quencher to the fluorophore (Biwersi et al. 1992).

We observed that covalently linked BAC to DNA results in dramatic quenching leading to reduced chloride sensitivity of BAC. We did not observe any significant effect of linker flexibility on the chloride sensitivity of BAC. Interestingly, the extent of BAC quenching increased in the case of scaffolds that carried an internal BAC label. However, the chloride sensitivity of BAC remained unaffected and this was regardless of the nature of flanking base pairs. Upon conjugation to PNA, a major population of BAC was in a similar environment as that of free BAC resulting in significant improvement in chloride sensitivity. Importantly, no bound/intercalated form of BAC was observed in ssPNA, dsPNA or DNA-PNA hybrids unlike as seen in dsDNA based constructs. Currently, we cannot deconvolute the relative contributions of PET-based quenching of BAC by guanine residues and the shielding effect due to the negatively charged DNA backbone. The difference in sequences of DNA and PNA strands used in this study support that these effects are sequence independent.

To achieve intracellular targeting and reasonable chloride sensitivity we designed *Clensor* where BAC is covalently linked at the N-terminus of a DNA-PNA hybrid duplex. It showed significant improvement in fluorescence intensity as well as chloride sensitivity compared to DNA based scaffolds. The BAC-PNA module serves as the sensing module while DNA serves as the targeting module. The basic principles involved in the design are generalizable to a variety of ionic reporters and can be used for developing any collisional quenching based nucleic acid sensor.

We therefore describe some general guidelines while designing ionic reporters using DNA. To sense ions by collisional quenching, one may increase bimolecular collisional quenching constants by choosing a sensing dye oppositely charged compared to the charge of the ion being detected (Ando and Asai 1980). We may achieve this by modifying functional groups on the dye such that it decreases electrostatic repulsion between the ion of interest and reporter dye (Huber et al. 1999). For example, if one is sensing negatively charged ions, carboxylate groups could be modified to esters or amides. Dyes that fluoresce at longer wavelengths are preferred due to lower phototoxicity and autofluorescence contributions (Hazelwood et al. 2007). Both sensing and normalizing dyes should be spectrally well separated and placed spatially at least 10 nm apart to avoid cross-talk (Lakowicz 2006). Further substantial spatial separation between sensing and normalizing dyes would enable better binding between sensor and its protein targets as well as preserve the photophysical properties of both dyes. The use of an electrically neutral PNA backbone disrupts intercalation between the dye and carrier scaffold due to lesser breathing motions associated with PNA-DNA hybrids (Wittung et al. 1994), which can be leveraged to achieve better sensing. DNA-PNA hybrids have much lower interstrand electrostatic repulsions that results in higher Tm values of duplex domains. This can therefore reduce the molecular weight of nucleic acid-based reporter, which is highly desirable when investigating living systems (Armitage et al. 1998). Given that guanines tend to quench fluorophores due to PET (Heinlein et al. 2003), one should take care that sequence designs avoid dyes being placed proximal to guanines. Sequence designs should further avoid 5' terminal guanines or GR (where R = G/A) as this reduces guanine ionization potentials by 0.2-0.5 eV due to stacking (Sugiyama and Saito 1996). Higher ionization potential of G reduces the probability of PET. Use of rigid linkers and incorporation of bulges are useful strategies to disrupt stacking interactions between dyes and

backbone. However it is important to note that coplanar stacking of dyes with purines (G>A) tends to increase static quenching (Heinlein et al. 2003).

Chapter 3

3 Quantitative maps of endosomal DNA processing by molecule counting

The processing of endocytosed cargo within cells is highly orchestrated. The stage-specific processing of endocytic cargo in immune cells affects important phenomena such as antigen cross presentation, evasion of the immune system by pathogens and even the differentiation between self and non-self DNA. (Rincon-Restrepo et al. 2017; Barton et al. 2006; Compeer et al. 2012) For example, when vaccine nanocarriers are processed at the stage of early endosomes in bone marrow dendritic cells (BMDCs), $CD8^+$ T-cells are activated via MHC-I antigen presentation. However, when the same nanocarriers are processed in lysosomes, $CD4^+$ T-cells are activated via MHC-II antigen presentation. (Rincon-Restrepo et al. 2017) Dendritic cells harbor mechanisms that attenuate endosomal maturation so that antigen fragments of endocytosed pathogens are preserved longer. Microbes such as mycobacteria and salmonella leverage this mechanism to prevent the display of MHC-I antigens. (Compeer et al. 2012) "Self DNA", generated from damaged or apoptotic host cells, is endocytosed by immune cells and distinguished from "non-self DNA", of viral/bacterial origin, based on their rate of digestion in specific endocytic organelles. (Barton et al. 2006)

Undigested DNA that traffics along the endolysosomal pathway of immune cells is one of the triggers of the immune response, whose dysregulated processing causes autoimmune disorders such as systemic lupus erythematosus (SLE). (Pathak and Mohan 2011; Chan et al. 2015),(Kawane et al. 2014) Endocytosed DNA is digested by DNase II ubiquitously in all tissues and this process

plays a critical role in during development, apoptosis, autophagy, erythropoiesis and phagocytosis. (Evans and Aguilera 2003) DNase II knockout mice are embryonic lethal due to constitutive activation of immune pathways that leads to anemia. However, mice lacking *Dnase2a* and interferon alpha receptor (*Ifnar*) are normal at birth, but the over production of TNF-α leads to chronic arthritis, an autoimmune disorder. (Kawane et al. 2006) Endocytosed self DNA triggers the immune response only when it is delivered undigested to TLR-9 containing endocytic organelles. (Barton et al. 2006) The anti-microbial peptide LL37 binds to immunogenically inert self DNA to form aggregates that remain undigested in endocytic compartments and induces cytokine production via TLR-9. (Lande et al. 2007) This is also observed when plasmid DNA complexed with sera from SLE patients is endocytosed by macrophages. (Vallin et al. 1999) Thus, endocytosed DNA is processed at specific stages during endosomal maturation and the disruption of this organelle-specific processing leads to pathophysiological outcomes such as psoriasis, arthritis and SLE.(Lande et al. 2007)

Cells distinguish self DNA from non self DNA based upon the fact that self DNA is usually processed efficiently in extracellular space by DNase I or in endosomes by DNase II before it binds to lysosomal TLR-9 and activates immune cells. (Ishii and Akira 2005; Barton et al. 2006) Endocytosed immunogenic CpG containing DNA (CpG-DNA) is processed in LAMP-2^+ compartments by DNase II and the digestion resistant DNA fragments activate TLR-9 in dendritic cells. (Chan et al. 2015) The localization of DNase II is considered to be largely extralysosomal and upon CpG-DNA treatment, DNase II translocates to LAMP-2^+ compartments. However, it is currently unclear in which organelles CpG-DNA and genomic DNA are cleaved by DNase II or where TLR-9 is activated by cleaved DNA in dendritic cells.(Chan et al. 2015) Thus, the ability to quantitatively map endosomal DNA processing of synthetic DNA fragments while retaining

organelle-specific information, would enable us to understand how self and non-self DNA are distinguished at the cellular level.

The ability to study endosomal processing and regulators thereof have been significantly hampered by the lack of methods to quantitatively map cargo processing in cells while retaining organelle-specific information. Endosomal processing has been well-studied by biochemical assays such as sulfation, radio labeling, RT-PCR and transient or induced protein expression. (Amessou et al. 2006; Stechmann et al. 2010; Weihe 2014; Sperinde et al. 2001; Tjelle et al. 1996) While these methods can precisely quantitate cargo processing or cargo cleavage and have guided our current understanding of endosomal cargo processing, they utilize cell extracts or whole cell intensities and thus spatial or organelle-specific information is lost. Fluorescence microscopy methods provide spatial and organelle-specific resolution, but methods to quantitate endocytic cargo are still lacking. Reporters of endosomal cargo processing such as disulfide reduction, pH sensitive naphthofluorescein or split GFP complementation can provide spatial information on activity, but are limited in terms of quantitative precision. (Qian et al. 2015; Hällbrink et al. 2001; Kim et al. 2015; Brown and Swank 1983; Amessou et al. 2006; Yang et al. 2006) On the other hand, super-resolution microscopy methods such as PALM and qPAINT have recently been applied to protein markers of organelles, where protein abundance has been accurately mapped while retaining organelle-specific information. (Puchner et al. 2013; Jungmann et al. 2016) Yet, there is still no way to obtain such quantitative maps of endocytic cargo processing that occurs within the organelle lumen while retaining organelle-specific cargo abundances.

Here, we combine the molecular precision afforded by synthetic DNA nanodevices with the quantitative precision of a new molecule counting method to quantitatively map DNase II-

mediated processing of DNA as a function of endosomal maturation within innate immune cells.[6-8] Intracellular single-molecule, high-resolution localization and counting (iSHiRLoC) is a molecule localization and counting protocol that has been used to quantitatively map cytosolic distribution of miRNA in HeLa cells. (Pitchiaya et al. 2012) In iSHiRLoC, the number of fluorophore labeled miRNA molecules microinjected in cells are counted by the number of photobleaching events observed per photobleaching decay trace for each particle/cluster. We have leveraged this approach to now count molecules in with organelle-level resolution and have applied it to endocytosed dsDNA trafficking along the scavenger receptor-mediated uptake pathway. Using this new method called organellar single-molecule, high-resolution localization and counting (oSHiRLoC) we have constructed organelle-specific dsDNA abundance maps in the presence and absence of a DNase II inhibitor. This revealed that the major site of DNase II activity in reticular macrophages were the lysosomes. oSHiRLoC can be applied to pinpoint the role of diverse cofactors or protein regulators of endosomal processing of DNA, RNA or their synthetic mimics in immune cells.

3.1 Materials and Methods

3.1.1 Reagents

All the oligonucleotides used were obtained from Integrated DNA Technologies (IDT). Labeled oligonucleotides were subjected to ethanol precipitation to remove any contaminating fluorophores. Oligonucleotides were dissolved in Milli Q water a stock and was stored at –20^{o}C.

Table 6 *Oligonucleotide sequences used in this study*

Oligo name	Sequence (5'-3')	5' label
I4	CCC CTA ACC CCT AAC CCC TAA CCC CAT ATA TAT CCT AGA ACG ACA GAC AAA CAG TGA GTC	Cy5
I4'	GAC TCA CTG TTT GTC TGT CGT TCT AGG ATA TAT ATT TTG TTA TGT GTT ATG TGT TAT	None
Bleach-Cy5	ATA ACA CAT AAC ACA TAA CAA AAT ATA TAT CCT AGA ACG ACA GAC AAA CAG TGA GTC	Cy5
Bleach-488	ATA ACA CAT AAC ACA TAA CAA AAT ATA TAT CCT AGA ACG ACA GAC AAA CAG TGA GTC	Alexa 488

3.1.2 Cargo DNA sample preparation

Constituent complementary strands of $I4_{Cy5}$ (I4 and I4') were mixed in 20 mM sodium buffer pH 5.5 containing 100 mM KCl at 5 µM concentration. For dsDNA DNA, constituent strands dsDNA-Cy5 and I4' or dsDNA-A488 and I4') were mixed at 5 µM concentration in 50 mM sodium phosphate buffer pH 7. For both cases, the resultant solution was heated from 25^{o}C to 90^{o}C in 15 min and was then cooled to room temperature at 1^{o}C/2 min and equilibrated at 4^{o}C overnight.

3.1.3 Protein conjugation

Ovalbumin was obtained from Sigma was labeled with FITC using a standard protein labeling protocol. (Mckinney et al. 1964) Briefly, 200 µl of 1.25 mg/ml FITC solution in 0.1 M sodium phosphate buffer at pH 8 was added to 500 µl of 10 mg/ml protein solution. The reaction mixture was adjusted to pH 9.0 with 0.1 M trisodium phosphate. The reaction mixture was maintained at 25°C for 3 hours. Labeled ovalbumin was purified from reaction mixture using 10 kDa cutoff Amicon filter using PBS and was then stored in PBS at –20^{o}C.

Mouse Apo-transferrin was obtained from Sigma and was converted to holo-transferrin by loading with Fe(III) as described previously. (Bunescu et al. 2008) Briefly, 4.49 mg of $FeCl_3$ was dissolved in 2 ml of water and was neutralized with sodium hydroxide. 106 mg of nitrilotriacetic acid was added to it and the solution was neutralized again. 0.5 mg of apo-transferrin was dissolved in 100 µl of buffer 1 (0.1 M $NaClO_4$/20 mM $NaHCO_3$/10 mM Tris-HCl, pH 7.6) (5 mg/ml protein

concentration). To this protein solution, 1 µl of above Fe^{3+} solution was added, incubated for 1-hr at room temperature and was subjected to 30 kDa cutoff Amicon. Buffer was exchanged with buffer2 (100 mM sodium bicarbonate buffer pH 9) and volume was concentrated to 5 mg/ml.

In order to label holo-transferrin with Rhodamine B, 0.2 ml of 5 mg/ml holo-transferrin solution in pH 9, 0.1 M sodium bicarbonate buffer was mixed with 6.7 µl of 20 mg/ml Rhodamine B isothiocyanate solution. Solution was allowed to stir at RT for 1 hour and was then subjected to 30 kDa cutoff Amicon purification using perchlorate buffer (0.1 M $NaClO_4$/20 mM $NaHCO_3$/10 mM Tris-HCl, pH 7.6).

3.1.4 Cell culture and labelling with endocytic markers

J774A.1 macrophages (ATCC No. TIB-67) were a kind gift from Prof Deborah Nelson, Department of Pharmacological and Physiological Sciences, the University of Chicago. They were cultured in Dulbecco's Modified Eagle's Medium/F-12 (1:1) (DMEM-F12) (Invitrogen Corporation, USA) containing 10% heat inactivated Fetal Bovine Serum (FBS) (Invitrogen Corporation, USA), 100 U/ml penicillin and 100 g/ml streptomycin at 37ºC in 5% CO2, and were used at 60% confluence.

In order to label early endosomes, J774A.1cells were co-pulsed with a cocktail of 1 µM Rhodamine labeled holo-transferrin and 500 nM Cy5 labeled dsDNA for 10 min at 37ºC. Cells were immediately washed with PBS and placed on ice to prevent endocytosis progression. Cells were surface stripped by incubating them in surface stripping buffer (160 mM sodium ascorbate, 40 mM ascorbic acid, 1 mM $CaCl_2$, and 1 mM $MgCl_2$, pH 4.5.) for 10 min on ice. Cells were then washed with PBS and fixed using 2.5 % paraformaldehyde (PFA) at room temperature for 20 min. For labeling late endosomes, cells were pulsed with Cy5 labeled DNA dsDNA in complete medium for 5 min at 37ºC followed by addition of FITC labeled ovalbumin such that its final concentration

in pulsing medium was 1 µM. After 5 min pulse at 37°C, cells were washed with PBS and were chased at 37°C for 30 min in complete medium. Cells were then washed, surface stripped and fixed as it were done for early endosome sample. For labeling lysosomes, cells were pulsed with 0.5 mg/ml TMR labeled 10 kDa dextran for 16 hours in complete medium at 37°C followed by 2 hours chase in complete medium. Cells were then pulsed with 500 nM Cy5 labeled DNA dsDNA for 10 min followed by 2 hours chase in complete medium. Cells were then washed, surface stripped, fixed and imaged on confocal microscope.

3.1.5 Labeling endosomes for molecule counting

In a typical molecule counting experiment, for labeling early or late endosomes J774A.1cells were pulsed with a cocktail of 25 nM of dsDNA-Cy5 (reporter) + 475 nM dsDNA-A488 (endocytic tracer) for 10 min and chased for indicated time in DMEM with 0.1% BSA (without serum) at 37°C. In the same way, lysosomes were labeled with 100 nM of dsDNA-Cy5 (reporter) + 400 nM dsDNA-A488 (endocytic tracer) for no inhibitor sample and with 50 nM of dsDNA-Cy5 (reporter) + 450 nM dsDNA-A488 (endocytic tracer) for 10 uM inhibitor sample. Cells were then washed with PBS, surface stripped, incubated at room temperature for 3 hours and imaged in imaging buffer (Tris-base 50mM, NaCl 10mM, Glucose 10%, oxygen-scavenging system (0.1 mg/ml glucose oxidase, 0.02 mg/mL catalase, pH=8) on Total Internal Reflection Fluorescence (TIRF) microscope.

3.1.6 DNase II inhibitor treatment

In order to block DNase II activity, J774A.1cells were pretreated with 10 µM DNase II inhibitor peptide ID2-3 in DMEM with 0.1% BSA (without serum) for 1 hour at 37°C. (Sperinde et al. 2001) Cells were then pulsed with cargo DNA dissolved in DMEM with 0.1% BSA and 10 µM DNase

II inhibitor peptide (without serum) at 37^{o}C for 10 min and were chased in DMEM with 0.1% BSA (without serum) and 10 µM DNase II inhibitor peptide at 37^{o}C for indicated time.

3.1.7 Image acquisition

Confocal images were acquired Olympus FV1000 confocal laser scanning microscope set up equipped with IX81 body, 60x / NA 1.42 oil (PlanApoN) objective, multi alkali PMTs and laser lines for 488, 543 and 633 nm excitation.

TIRF images for molecule counting were acquired on Leica four-color (405nm, 488nm, 532nm and 642nm) Total Internal Reflection fluorescence (TIRF) microscope equipped with automated critical angle positioning, 160x NA 1.43 state of the art, adhesive-free objective, Supressed Motion (SuMo) stage which locks in the 160x objective to minimize sample drift and iXon Ultra EMCCD camera. Before image acquisition, samples were allowed to sit on microscope undisturbed for thermal equilibration. This prevented z-drift during image series acquisition. Image series of 4,000 to 12,000 frames was acquired with 100 ms exposure.

3.1.8 Image analysis

Acquired images were opened in Fiji and were exported into image sets for small areas using custom written ImageJ macro. This was a vital step as too large image sets can't be opened in LabView program due to memory limits. Images were manually analyzed and spots where significant colocalization in endocytic tracer and reporter channels was observed were marked and fluorescence photobleaching trace for each such spot was exported. More than 200 such traces for each sample was then fit using a previously reported Python program "Photobleach". (Tsekouras et al. 2016) Results were then exported into excel and were plotted in OriginPro software.

3.2 Results

3.2.1 Molecule counting workflow

iSHiRLoC is a molecule counting method which was developed to study intracellular localization, composition and transport of miRNA complexes. (Pitchiaya et al. 2012) HeLa cells were microinjected with let-7 miRNA and were imaged using highly inclined laminar optical sheet (HILO) microscopy to produce photobleaching decay traces of individual RNA complexes in cytosol. The number of photobleaching steps observed per trace revealed number of let-7 miRNA molecules per complex. In a recent study, a software package "Photobleach" was developed to fit ≥ 500 photobleaching steps in a photobleaching decay trace. (Tsekouras et al. 2016) We reasoned that molecule counting by oSHiRLoC applied to subcellular compartments could potentially be used to quantify cargo abundance while retaining organelle localization if the endocytic cargo displayed a fluorescent label. Macrophages are innate immune cells that endocytose single and double stranded DNA through scavenger receptors. Endocytosed DNA cargo is trafficked along the endolysosomal pathway progressing from the early endosome, to the late endosome and finally reaching the lysosome, where they are degraded.

In order to see whether we could use oSHiRLoC to count molecules in endosomes, we pulsed a 57 base pair long duplex DNA cargo labeled with Cy5 along with 19 equivalents of the same 57 base pair dsDNA sequence bearing an Alexa 488 label such that the total strand concentration of both duplexes was 500 nM (***Figure 14a***). We varied the ratios of dsDNA-Cy5: dsDNA-A488 from 1:19 to 1:4. Both strands were uptaken with similar efficiency and are expected to label all compartments retaining their relative ratios. Here, dsDNA-A488 functions as a fiducial marker for endosomes along the scavenger receptor pathway, which is also facilitated by its high molar brightness. The dsDNA-Cy5 functions as the fluorescent reporter for oSHiRLoC, and is

particularly suited for counting by photobleaching due to the negligible contribution of cellular autofluorescence in the Cy5 channel. In addition, any single stranded DNA labeled with Cy5 cannot be retained in endosomes, either due to rapid degradation, or because of endosomal translocation, which affords a clean system that reports on the abundance of only undigested, unprocessed, dsDNA cargo. (Lorenz et al. 2011)

A modified protocol of oSHiRLoC was used to count endocytosed dsDNA cargo in cells. Reticular macrophages J774A.1 cells were pulsed with 500 nM of a given ratio of dsDNA-Cy5 and dsDNA-A488, washed and chased for a specified duration. The cells were fixed at a specified time point, and imaged under a TIRF microscope in the Alexa488 channel and a photobleaching image series was captured in the Cy5 channel (***Figure 14b***). The images in the A488 channel corresponded to endocytic compartments, and the corresponding photobleaching series in the Cy5 channel yielded the number of photobleaching events in each compartment. To eliminate false positives from the data set of endosomal images, only those compartments showing colocalization between Alexa 488 and Cy5 channels were analyzed. We fit photobleaching data using photobleaching data-fitting package "Photobleach", and extracted the number of photobleaching steps observed per trace (***Figure 14c and Figure 15***). [6] The average number of molecules per compartment was obtained from the product of the number of photobleaching steps observed in the compartment and the ratio of dsDNA-Cy5 to dsDNA-A488.

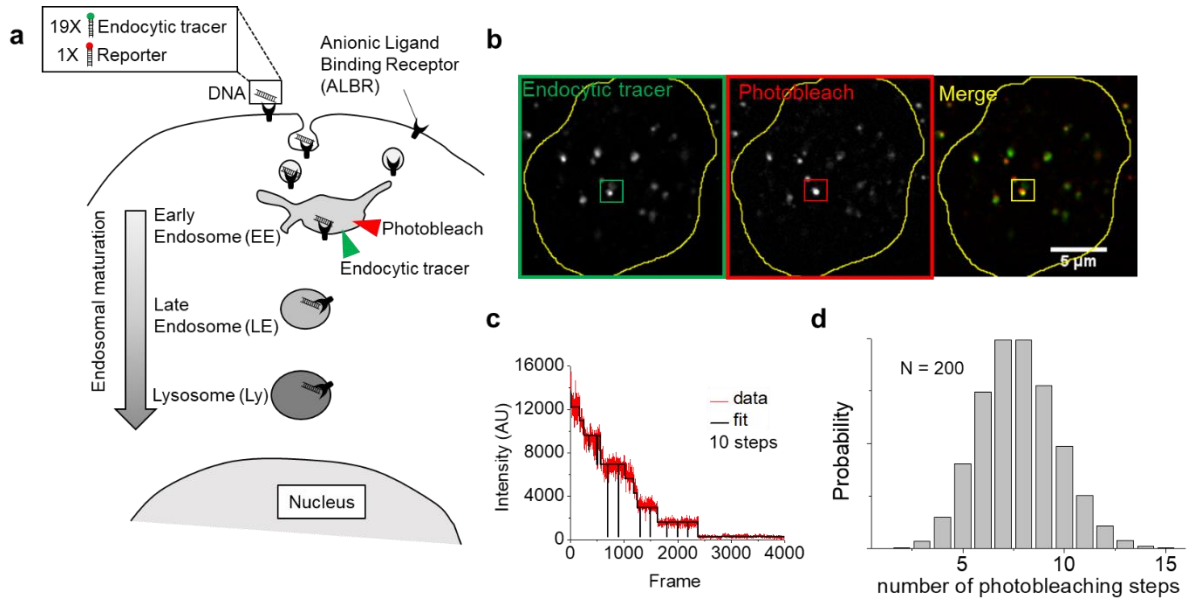

Figure 14 *Molecule counting workflow. Schematic representing the work flow for counting number of endosomal DNA cargo in J774A.1 cells. (A) Cells are labeled with cocktail of cargo DNA (1X dsDNA-Cy5 (reporter) : 19X dsDNA-A488 (endocytic tracer)). (B) Representative TIRF images of early endosomes (EE) of J774A.1 cells containing cargo DNA. Cells were imaged in the Alexa 488 channel and molecule counting was performed by photobleaching in the Cy5 channel. (C) Representative photobleaching trace measured in the Cy5 channel for the indicated endosome. (D) Histogram of the number of photobleaching steps observed for a sample. The number of devices per compartment, N* = number of photobleaching steps observed × dilution factor.*

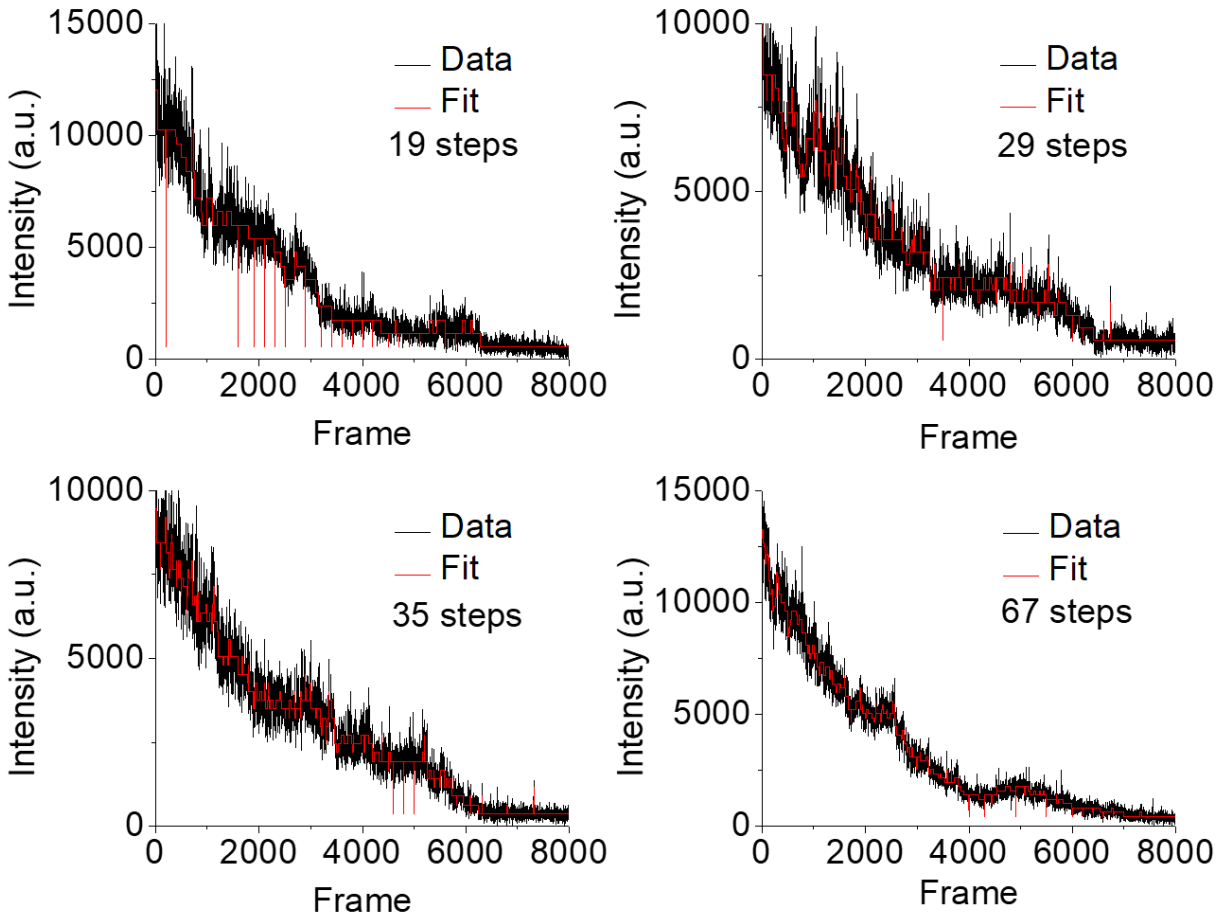

Figure 15 *Photobleaching data fitting. Representative photobleaching decay traces (black) and their data fits (red) for early endosomes.*

3.2.2 Trafficking of cargo DNA along the scavenger receptor mediated endocytic pathway

We first confirmed that extraneously added cargo DNA was taken up via the scavenger receptor (SR) or anionic ligand binding receptor (ALBR) mediated endocytic pathway, by carrying out a competition assay using maleylated BSA (mBSA). We observed that Cy5 labeled cargo dsDNA ($I4_{Cy5}$) uptake is abolished in presence of 25 equivalents excess of mBSA (***Figure 16g***). (Modi et al. 2009) In order to count cargo DNA molecules, as a function of endosomal maturation along this endocytic pathway, we first standardized the durations for cargo DNA to reach the early endosome, the late endosome and the lysosome, post-pulsing with J774A.1 cells.

Transferrin was used as a marker of the early/sorting endosomes. (Raje et al. 2007; Wadsworth and Goldfine 2002) We found maximal colocalization with transferrin-Rhodamine B and cargo DNA at t = 5-10 minutes of chase after a 10 min pulse of 500 nM transferrin-Rhodamine B and 500 nM cargo DNA (***Figure 16a & d***). It is known that after a 5 minutes pulse and 30 minutes chase, ovalbumin is enriched in Rab-7 positive compartments corresponding to late endosomes in J774A.1 cells. (Tjelle et al. 1996) In our hands, cargo DNA colocalized well with fluorescein-labeled Ovalbumin with a 10 minute pulse and a 30 minute chase (***Figure 16b & e***). Finally, fluorescently labeled dextrans localize in the lysosome after a 16 h pulse and a 4 h chase in J774A.1 cells. (Majumdar et al. 2007) Cells whose lysosomes were pre-labeled using the aforementioned protocol showed maximal colocalization with cargo DNA when the latter was pulsed for 10 minute chased for 2 hours (***Figure 16c & f***).

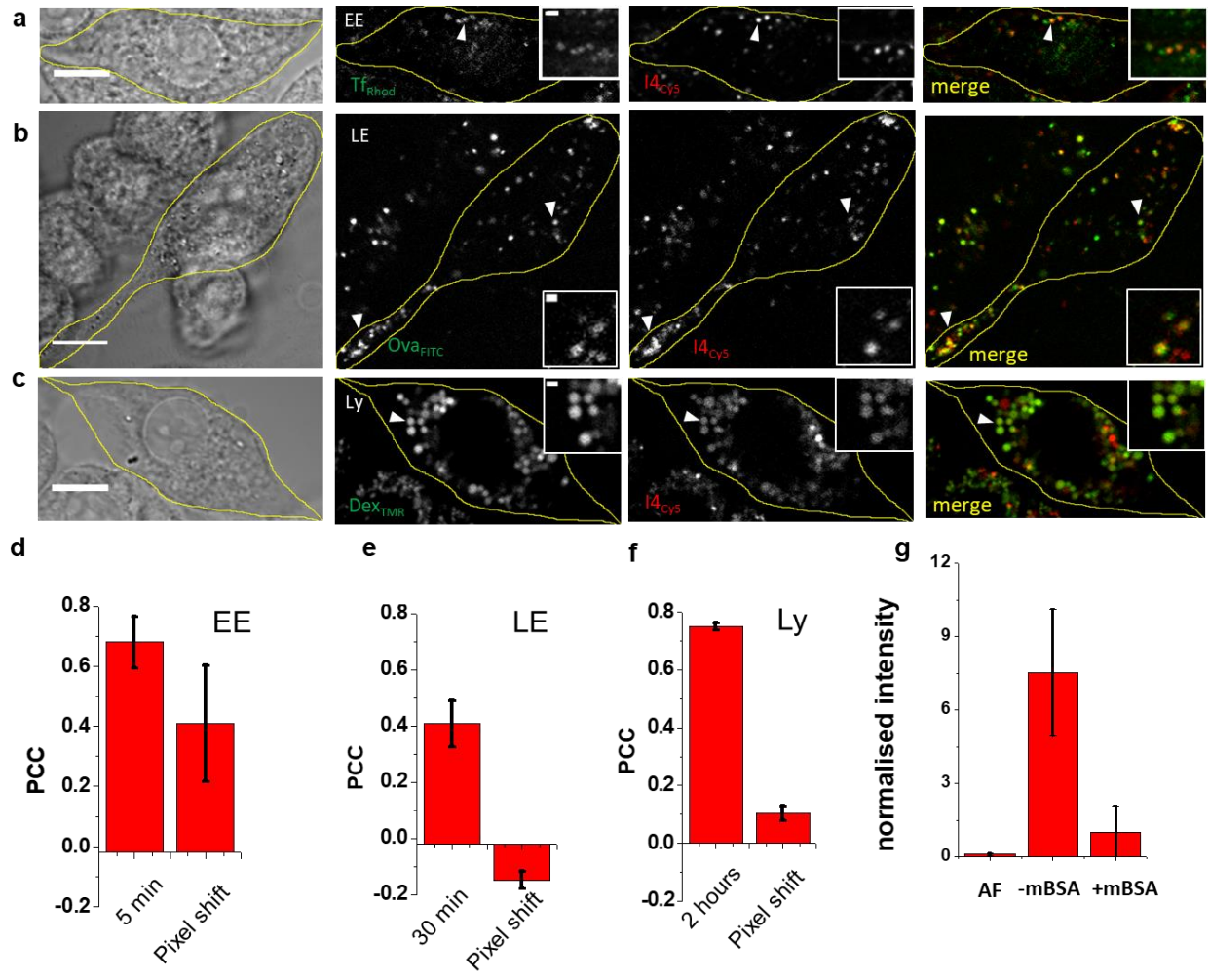

Figure 16 *Trafficking of cargo DNA along endocytic pathways. Representative single-plane confocal images showing co-localization of cargo with various compartment markers (a) J774A.1 cells were co-pulsed with* $I4_{Cy5}$ *and transferrin-Rhodamine B (*Tf_{Rhod}*) to label the early endosome. (b)Colocalization between* $I4_{Cy5}$ *and Ovalbumin-FITC (*Ova_{FITC}*) to label late endosomes. (c) Lysosomes were pre-labeled with Dextran-TMR (*Dex_{TMR}*) and then labeled with* $I4_{Cy5}$*. Colocalization between* Dex_{TMR} *and* $I4_{Cy5}$ *(Lysosomes). All cell boundaries are demarcated with yellow outlines. (d-f) Quantification of co-localization by Pearson's Correlation Coefficient (PCC) between cargo DNA and endosomal markers in a-c. Values indicate mean of n~20 cells. (g)* $I4_{Cy5}$ *internalization by J774A.1 cells in the presence (+mBSA) and absence (−mBSA) of excess competitor ligand maleylated BSA (mBSA, 10 μM) and autofluorescence (AF). Error bars indicate the mean of two independent experiments ± std. dev. (n=30 cells). Scale bars, 10 μm and 1 μm for insets.*

3.2.3 Molecule counting in endosomes as a function of endosomal maturation

We first mapped the abundance of endocytosed cargo DNA as a function of endosomal maturation, in order to obtain a basal organelle-specific map of cargo DNA processing. Specific endocytic organelles in J774A.1 cells were labeled with a cocktail of 1: 19 dsDNA-Cy5: dsDNA-A488 cargo DNA, using the pulse-chase protocols determined above, and fixed for 20 minutes with PFA. Post fixation, cells were incubated at room temperature for 3 h to allow endosomal leakage of digested cargo DNA fragments if any. Cells were then imaged on a TIRF microscope to quantify photobleaching steps for each endosome in the red channel (***Figure 17***). It was observed that early endosomes showed two kinds of populations, with endosomes containing ~200 molecules and those containing ~700 molecules. Overall, early endosomes showed a mean of 344 ± 58 cargo DNA molecules per endosome (***Figure 17 top panel & Figure 19b***). We speculate that endosomes showing fewer molecules of cargo DNA might correspond to freshly endocytosed cargo, while endosomes showing larger amounts of cargo DNA could correspond to larger sorting stations.

Late endosomes show a maximum at ~200 with a mean of 325 ± 76 cargo DNA molecules per compartment revealing a fairly broad distribution of cargo molecules in their lumens (***Figure 17 middle panel & Figure 19b***). However, in the lysosomes, the abundance of cargo DNA molecules per compartment dropped 3-fold, showing a maximum at 50 and a mean of 103 ± 7 (***Figure 17 bottom panel & Figure 19b***) reflecting the effect of endosomal cargo processing/digestion.

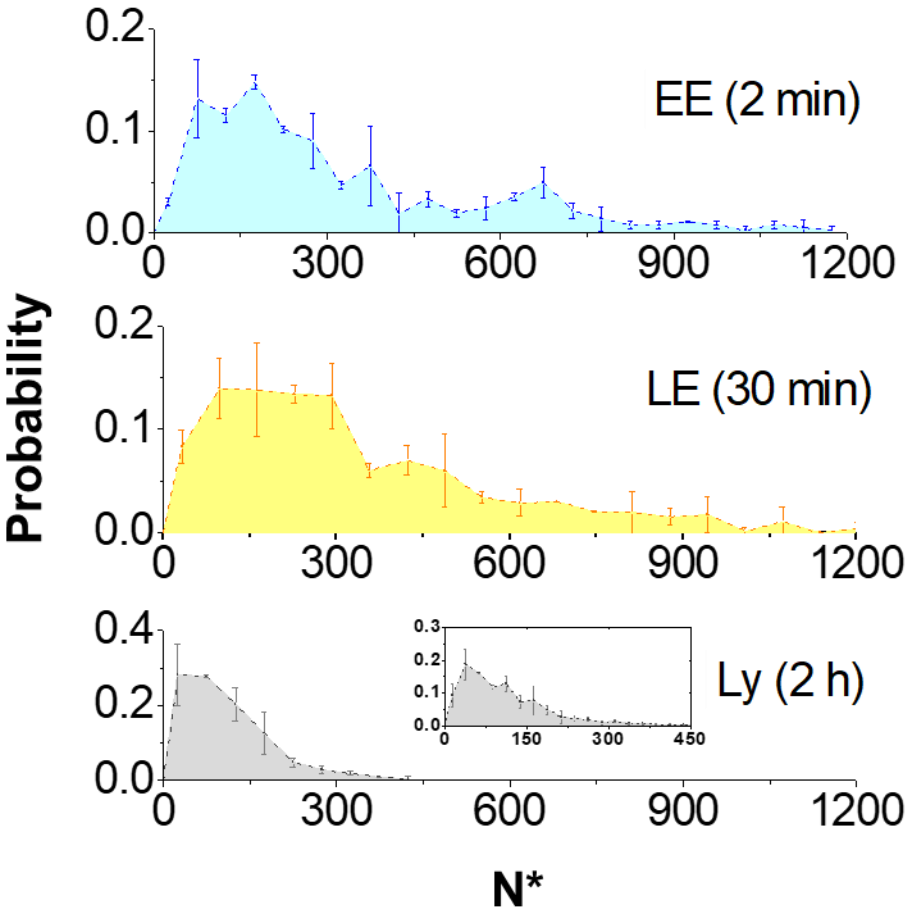

Figure 17 *Molecule counting in endosomes. Histograms of the number of devices observed per compartment in early endosomes (EE), late endosomes (LE) and lysosomes (Ly) of J774A.1 cells. Early and late endosomes were labeled with 25 nM of dsDNA-Cy5 (reporter) + 475 nM dsDNA-A488 (endocytic tracer). Lysosomes were labeled with 100 nM of dsDNA-Cy5 (reporter) + 400 nM dsDNA-A488 (endocytic tracer). Error bars indicate the mean of two independent experiments ± std. dev. N* = n_p × d where N* = total number of devices per compartment, n_p = number of photobleaching steps observed and d = dilution factor. n = 200 endosomes (duplicate). Inset is zoom of histogram showing distribution at lower N*.*

3.2.4 Molecule counting reveals DNase II activity in lysosomes

In order to study the organelle-specific activity of DNase II if any in immune cells, we treated cells with a well-characterized peptide inhibitor of DNase II, and performed molecule counting experiments at each stage of endosomal maturation. (Sperinde et al. 2001) Upon DNase II inhibitor treatment, counting experiments at the level of early endosomes revealed that the population

containing ~200 cargo DNA molecules increased, while the population containing ~700 cargo DNA molecules decreased (***Figure 19 top panel & Figure 19b***). However, the mean abundance of cargo DNA molecules in early decreased upon DNase II inhibition (***Figure 19b***), suggesting a possible slowing down of endosomal maturation, but not uptake. (Scott et al. 2014) Surprisingly, late endosomes showed negligible effect of DNase II inhibition upon cargo abundance revealing that in J774A.1 cells, digestion of endosomally localized DNA cargo does not occur in late endosomes (***Figure 19 middle panel & Figure 19b***). However, when we inhibited DNase II and counted cargo molecules in lysosomes, we observed the accumulation of large amounts of undigested cargo DNA in lysosomes showing a 2-fold increase in maximum observed, i.e., ~100 and a large spread of the mean centered at 233 ± 79 cargo DNA molecules (***Figure 19 bottom panel & Figure 19b*)**. This indicated that DNase II based endosomal DNA processing happens only in lysosomes (***Figure 19c & Figure 18)***.

The changes in populations at the early endosomal stage fits with a slowing down of endosomal fusion with the sorting stations consistent with slower endosomal maturation, possibly as a result of cargo DNA accumulation in lysosomes. Slowing down of endosomal maturation due to cargo accumulation in lysosomes is well documented, e.g., trafficking of acid sphingomyelinase (ASM) via mannose-6-phosphate receptor is impeded in ASM knock out cells. (Dhami and Schuchman 2004)

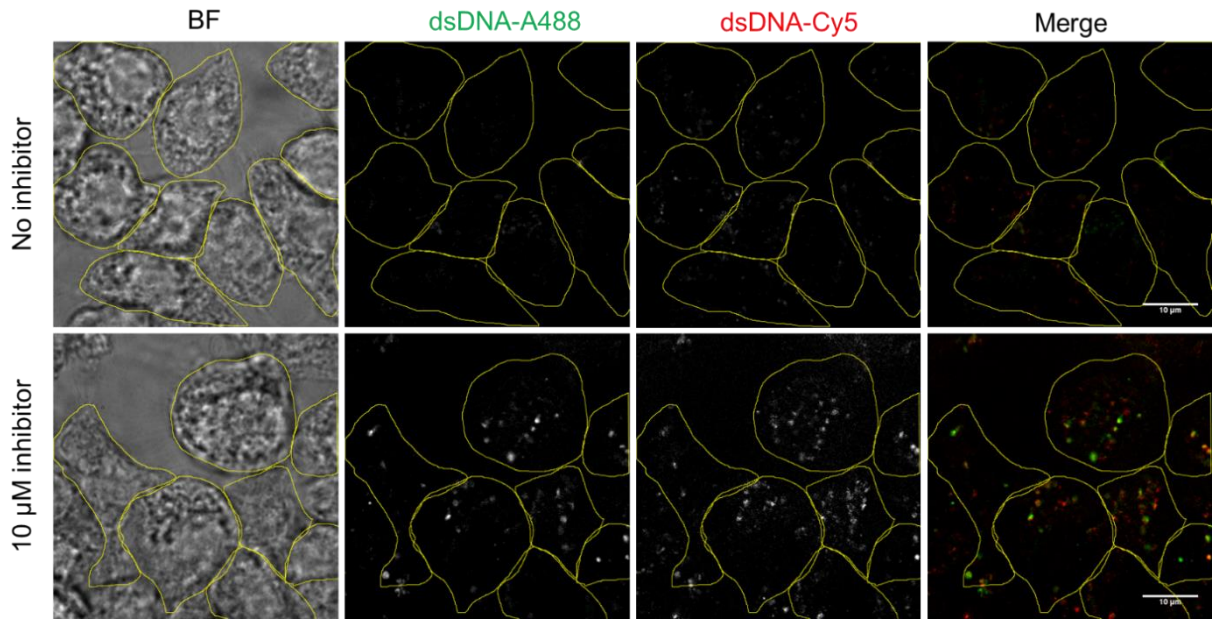

Figure 18 *Effect of DNase II inhibitor on lysosomal cargo DNA processing. Lysosomes of J774 cells were labeled with 100 nM of dsDNA-Cy5 (reporter) + 400 nM dsDNA-A488 (endocytic tracer) for no inhibitor sample and with 50 nM of dsDNA-Cy5 (reporter) + 450 nM dsDNA-A488 (endocytic tracer) for DNase II 10 µM inhibitor sample. Brightness of red channel image for no inhibitor sample has been scaled to half intensity to compensate for double concentration of dsDNA-Cy5. DNase II inhibitor sample shows bright and large lysosomes.*

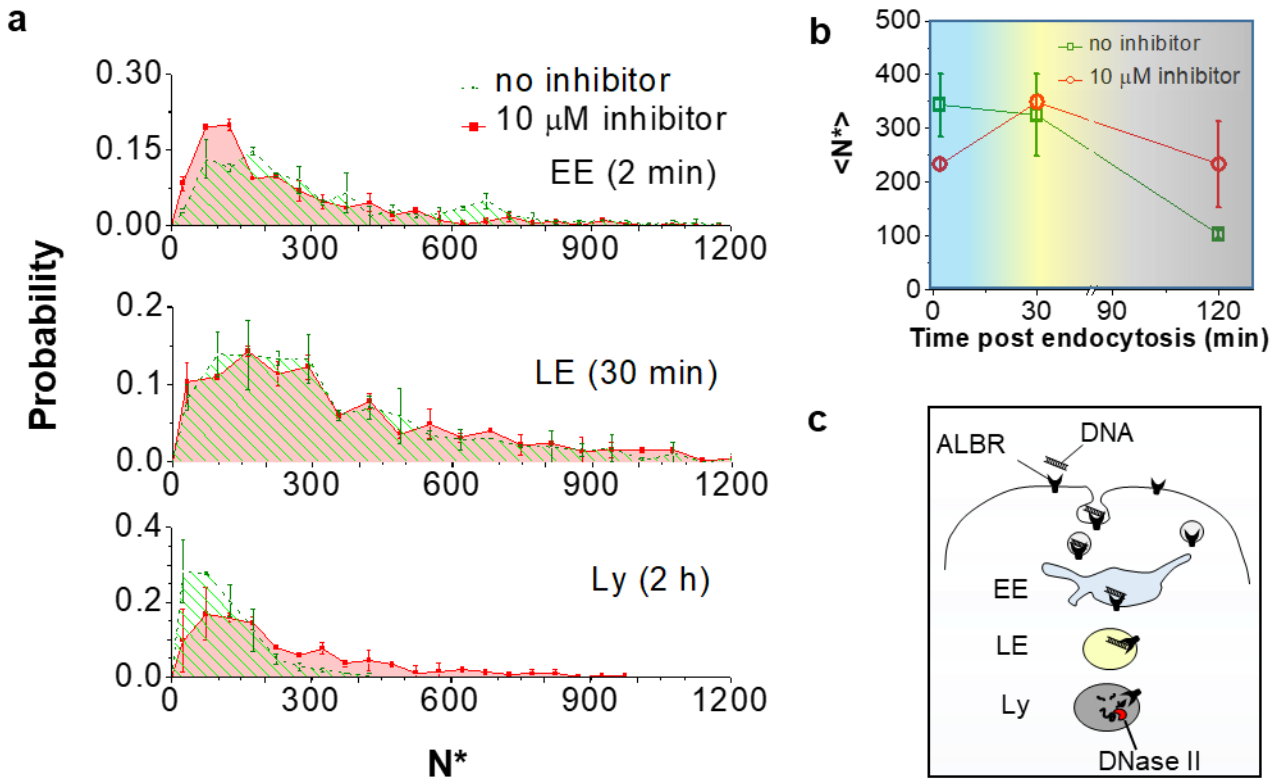

Figure 19 *Molecule counting reveals spatiotemporal role of DNase II. Histograms of number of devices observed per compartment in (a) early endosomes (EE), late endosomes (LE) and lysosomes (Ly) of J774A.1 cells in the presence of 10 μM DNase II inhibitor. Early and late endosomes were labeled as described earlier. Lysosomes were labeled with 50 nM of dsDNA-Cy5 (reporter) + 450 nM dsDNA-A488 (endocytic tracer). Traces are overlaid with the abundance profiles for each organelle in the absence of inhibitor (green) for comparison. (b) Variation in average number of devices per compartment as a function of time. Blue region indicates EE, yellow indicates LE while grey corresponds to lysosomes. Error bars indicate the mean of two independent experiments ± std. dev. N* = n_p × d. n = 200 endosomes (duplicate) (c) Proposed model of DNase II activity along the endolysosomal pathway.*

3.3 Conclusion

Undigested cargo DNA along the endolysosomal pathway of immune cells constitutes one of many important triggers in the immune response. For example, phagocytic as well as nonphagocytic tissues of DNase II knockout mice show elevated levels of undigested DNA from nucleus in autophagosomes and lysosomes and induced inflammation via STING mediated cytosolic DNA sensing pathway. (Lan et al. 2014) Defect in digestion of chromosomal DNA from engulfed cells

in mice activates phagocytic cells like macrophages, leading to anaemia in embryo and chronic arthritis in adults. (Kawane et al. 2001) Sequence specific digestion of immunogenic CpG DNA studies showed that endosomally localized DNase II based digestion of CpG DNA is necessary to trigger TLR-9 mediated cytokine production in dendritic cells.(Chan et al. 2015) Loss of DNase II activity triggers the manifestation of autoimmune disorders such as SLE, of which one of the hallmarks is the production of autoantibodies against double stranded DNA.(Kawane et al. 2001; Kawane et al. 2014) Our capacity to model the immune response using predictive computational models has been hindered by our inability to accurately specify both the location and abundance of ligands that trigger the immune response.

The endosomal load of unprocessed dsDNA cargo is determined by the rate of endocytosis, concentration of extraneous dsDNA, receptor density on plasma membrane and organelle-specific DNase II activity along the endolysosomal pathway.(Scott et al. 2014; Chan et al. 2015) Conventional methods to analyze DNA processing can quantitate processing efficiency albeit without organelle-specific information, or organelle-specific information without the ability to quantitate processing.(Hiroi et al. 2016) oSHiRLoC provides quantitative information on cargo DNA processing along with organelle specific information. This platform can be used to identify the site of action and assay the activity of processing enzymes as we have demonstrated for DNase II. Given the burgeoning use of biologically active, synthetic DNA and RNA nanostructures, circulating endogenous DNA and RNA molecules, methods to understand their differential processing within the cell would be critical to uncovering their mechanisms of action. (Chan et al. 2015; Howell et al. 2003; Surana et al. 2013; Haas et al. 2008; Ohto et al. 2015; Pathak and Mohan 2011; Surana et al. 2015)

Endosomal cargo quantification using oSHiRLoC is not limited to dsDNA, and is potentially applicable to a range of externally added endocytic ligands such as 'self-DNA'; or 'non-self DNA' ssDNA, dsRNA, shiga toxin, EGF, mannose-6-phosphate, that traffic along well-defined pathways.(Bhatia et al. 2016; Chan et al. 2015; Rigby et al. 2014; Henault et al. 2012; Dhami and Schuchman 2004; Tomas et al. 2014) In addition to enabling the quantification of trafficking cargo, this approach can be used to evaluate the processing of solutes, receptors, and pathogenic agents with organelle-specific information. It can also be used to assay the location and activity of regulators of endosomal cargo processing. (Coorens et al. 2015; Howell et al. 2003; Kaestner et al. 2015; Kawane et al. 2001; Crozat and Beutler 2004) For example, structure-activity relationships of various immunogenic CpG DNA sequences and their organelle-specific processing can be correlated with the downstream cellular immune response. (Chan et al. 2015) Absolute cargo abundance along with organelle-specific information would provide information on actual reaction rates and intrinsic processing heterogeneities. (Qian et al. 2015; Jung et al. 2017; Winterbourn et al. 2006) The ability to determine the concentration of reactive analytes in the relevant endocytic organelle and correlate it with the strength of the downstream cellular response would significantly aid quantitative computational modelling of cellular pathways.(Winterbourn et al. 2006)

Bibliography

Amann, R. and Fuchs, B.M. 2008. Single-cell identification in microbial communities by improved fluorescence in situ hybridization techniques. *Nature Reviews. Microbiology* 6(5), pp. 339–348.

Amessou, M., Popoff, V., Yelamos, B., Saint-Pol, A. and Johannes, L. 2006. Measuring retrograde transport to the trans-Golgi network. *Current protocols in cell biology / editorial board, Juan S. Bonifacino ... [et al.]* Chapter 15, p. Unit 15.10.

Ando, T. and Asai, H. 1980. Charge Effects on the Dynamic Quenching of Fluorescence of 1,N6-ethenoadenosine oligophosphates by iodide, thallium (I) and acrylamide. *Journal of biochemistry*.

Anon 2006. Time-Domain Lifetime Measurements. In: *Principles of Fluorescence Spectroscopy*. Boston, MA: Springer US, pp. 97–155.

Armitage, B., Koch, T., Frydenlund, H., Orum, H. and Schuster, G.B. 1998. Peptide nucleic acid (PNA)/DNA hybrid duplexes: intercalation by an internally linked anthraquinone. *Nucleic Acids Research* 26(3), pp. 715–720.

Arosio, D., Ricci, F., Marchetti, L., Gualdani, R., Albertazzi, L. and Beltram, F. 2010. Simultaneous intracellular chloride and pH measurements using a GFP-based sensor. *Nature Methods* 7(7), pp. 516–518.

Atianand, M.K. and Fitzgerald, K.A. 2013. Molecular basis of DNA recognition in the immune system. *Journal of Immunology* 190(5), pp. 1911–1918.

Barton, G.M., Kagan, J.C. and Medzhitov, R. 2006. Intracellular localization of Toll-like receptor 9 prevents recognition of self DNA but facilitates access to viral DNA. *Nature Immunology* 7(1), pp. 49–56.

Berglund, K., Schleich, W., Krieger, P., Loo, L.S., Wang, D., Cant, N.B., Feng, G., Augustine, G.J. and Kuner, T. 2006. Imaging synaptic inhibition in transgenic mice expressing the chloride indicator, Clomeleon. *Brain Cell Biology* 35(4-6), pp. 207–228.

Bhatia, D., Arumugam, S., Nasilowski, M., Joshi, H., Wunder, C., Chambon, V., Prakash, V., Grazon, C., Nadal, B., Maiti, P.K., Johannes, L., Dubertret, B. and Krishnan, Y. 2016. Quantum dot-loaded monofunctionalized DNA icosahedra for single-particle tracking of endocytic pathways. *Nature Nanotechnology* 11(12), pp. 1112–1119.

Bhatia, D., Surana, S., Chakraborty, S., Koushika, S.P. and Krishnan, Y. 2011. A synthetic icosahedral DNA-based host-cargo complex for functional in vivo imaging. *Nature Communications* 2, p. 339.

Bhattacharyya, A. and Lilley, D.M. 1989. The contrasting structures of mismatched DNA sequences containing looped-out bases (bulges) and multiple mismatches (bubbles). *Nucleic Acids Research* 17(17), pp. 6821–6840.

Bhattacharyya, A., Murchie, A.I. and Lilley, D.M. 1990. RNA bulges and the helical periodicity of double-stranded RNA. *Nature* 343(6257), pp. 484–487.

Biwersi, J., Farah, N., Wang, Y.-X., Ketcham, R. and Verkman, A.S. 1992. Synthesis of cell-impermeable Cl-sensitive fluorescent indicators with improved sensitivity and optical properties. *American Journal of Physiology-Cell Physiology*.

Blasius, A.L. and Beutler, B. 2010. Intracellular toll-like receptors. *Immunity* 32(3), pp. 305–315.

Bregestovski, P., Waseem, T. and Mukhtarov, M. 2009. Genetically encoded optical sensors for monitoring of intracellular chloride and chloride-selective channel activity. *Frontiers in Molecular Neuroscience* 2, p. 15.

Brown, J.A. and Swank, R.T. 1983. Subcellular redistribution of newly synthesized macrophage lysosomal enzymes. Correlation between delivery to the lysosomes and maturation. *The Journal of Biological Chemistry* 258(24), pp. 15323–15328.

Bunescu, A., Besse-Hoggan, P., Sancelme, M., Mailhot, G. and Delort, A.-M. 2008. Fate of the nitrilotriacetic acid-Fe(III) complex during photodegradation and biodegradation by Rhodococcus rhodochrous. *Applied and Environmental Microbiology* 74(20), pp. 6320–6326.

Casey, J.R., Grinstein, S. and Orlowski, J. 2010. Sensors and regulators of intracellular pH. *Nature Reviews. Molecular Cell Biology* 11(1), pp. 50–61.

Chakrabarti, M.C. and Schwarz, F.P. 1999. Thermal stability of PNA/DNA and DNA/DNA duplexes by differential scanning calorimetry. *Nucleic Acids Research* 27(24), pp. 4801–4806.

Chakraborty, K., Leung, K. and Krishnan, Y. 2017. High lumenal chloride in the lysosome is critical for lysosome function. *eLife* 6, p. e28862.

Chakraborty, K., Veetil, A.T., Jaffrey, S.R. and Krishnan, Y. 2016. Nucleic Acid-Based Nanodevices in Biological Imaging. *Annual Review of Biochemistry* 85, pp. 349–373.

Chan, M.P., Onji, M., Fukui, R., Kawane, K., Shibata, T., Saitoh, S., Ohto, U., Shimizu, T., Barber, G.N. and Miyake, K. 2015. DNase II-dependent DNA digestion is required for DNA sensing by TLR9. *Nature Communications* 6, p. 5853.

Chen, Y., Deffenbaugh, N.C., Anderson, C.T. and Hancock, W.O. 2014. Molecular counting by photobleaching in protein complexes with many subunits: best practices and application to the cellulose synthesis complex. *Molecular Biology of the Cell* 25(22), pp. 3630–3642.

Christensen, L., Fitzpatrick, R., Gildea, B., Petersen, K.H., Hansen, H.F., Koch, T., Egholm, M., Buchardt, O., Nielsen, P.E., Coull, J. and Berg, R.H. 1995. Solid-phase synthesis of peptide nucleic acids. *Journal of Peptide Science* 1(3), pp. 175–183.

Compeer, E.B., Flinsenberg, T.W.H., van der Grein, S.G. and Boes, M. 2012. Antigen processing and remodeling of the endosomal pathway: requirements for antigen cross-presentation. *Frontiers in immunology* 3, p. 37.

Coorens, M., van Dijk, A., Bikker, F., Veldhuizen, E.J.A. and Haagsman, H.P. 2015. Importance of Endosomal Cathelicidin Degradation To Enhance DNA-Induced Chicken Macrophage Activation. *Journal of Immunology* 195(8), pp. 3970–3977.

Coutinho, M.F., Prata, M.J. and Alves, S. 2012. Mannose-6-phosphate pathway: a review on its role in lysosomal function and dysfunction. *Molecular Genetics and Metabolism* 105(4), pp. 542–550.

Crozat, K. and Beutler, B. 2004. TLR7: A new sensor of viral infection. *Proceedings of the National Academy of Sciences of the United States of America* 101(18), pp. 6835–6836.

Dahm, R. 2008. Discovering DNA: Friedrich Miescher and the early years of nucleic acid research. *Human Genetics* 122(6), pp. 565–581.

Devuyst, O. and Luciani, A. 2015. Chloride transporters and receptor-mediated endocytosis in the renal proximal tubule. *The Journal of Physiology* 593(18), pp. 4151–4164.

Dhami, R. and Schuchman, E.H. 2004. Mannose 6-phosphate receptor-mediated uptake is defective in acid sphingomyelinase-deficient macrophages: implications for Niemann-Pick disease enzyme replacement therapy. *The Journal of Biological Chemistry* 279(2), pp. 1526–1532.

Di, A., Brown, M.E., Deriy, L.V., Li, C., Szeto, F.L., Chen, Y., Huang, P., Tong, J., Naren, A.P., Bindokas, V., Palfrey, H.C. and Nelson, D.J. 2006. CFTR regulates phagosome acidification in macrophages and alters bactericidal activity. *Nature Cell Biology* 8(9), pp. 933–944.

Dobrynin, A. 2008. Theory and simulations of charged polymers: From solution properties to polymeric nanomaterials. *Current Opinion in Colloid & Interface Science* 13(6), pp. 376–388.

Dornberger, U., Hillisch, A., Gollmick, F.A., Fritzsche, H. and Diekmann, S. 1999. Solution structure of a five-adenine bulge loop within a DNA duplex. *Biochemistry* 38(39), pp. 12860–12868.

Egholm, M., Buchardt, O., Christensen, L., Behrens, C., Freier, S.M., Driver, D.A., Berg, R.H., Kim, S.K., Norden, B. and Nielsen, P.E. 1993. PNA hybridizes to complementary oligonucleotides obeying the Watson-Crick hydrogen-bonding rules. *Nature* 365(6446), pp. 566–568.

Eriksson, M. and Nielsen, P.E. 1996. Solution structure of a peptide nucleic acid-DNA duplex. *Nature Structural Biology* 3(5), pp. 410–413.

Evans, C.J. and Aguilera, R.J. 2003. DNase II: genes, enzymes and function. *Gene* 322, pp. 1–15.

Gbadebo, A.M. and Nwufoh, C.O. 2010. Iodine concentrations in blood and urine samples of goitre and non-goitre patients in parts of Ogun State, Southwestern Nigeria. *Journal of geochemical exploration* 107(2), pp. 169–174.

Geddes, C.D. 2001. Optical halide sensing using fluorescence quenching: theory, simulations and applications - a review. *Measurement Science and Technology* 12(9), pp. R53–R88.

Geddes, C D, Apperson, K., Karolin, J. and Birch, D.J. 2001. Chloride-sensitive fluorescent indicators. *Analytical Biochemistry* 293(1), pp. 60–66.

Geddes, Chris D, Apperson, K., Karolin, J. and Birch, D.J.. 2001. Chloride sensitive probes for biological applications. *Dyes and Pigments* 48(3), pp. 227–231.

Germond, A., Fujita, H., Ichimura, T. and Watanabe, T.M. 2016. Design and development of genetically encoded fluorescent sensors to monitor intracellular chemical and physical parameters. *Biophysical reviews* 8(2), pp. 121–138.

Gohlke, C., Murchie, A.I., Lilley, D.M. and Clegg, R.M. 1994. Kinking of DNA and RNA helices by bulged nucleotides observed by fluorescence resonance energy transfer. *Proceedings of the National Academy of Sciences of the United States of America* 91(24), pp. 11660–11664.

Haas, T., Metzger, J., Schmitz, F., Heit, A., Müller, T., Latz, E. and Wagner, H. 2008. The DNA sugar backbone 2' deoxyribose determines toll-like receptor 9 activation. *Immunity* 28(3), pp. 315–323.

Hällbrink, M., Florén, A., Elmquist, A., Pooga, M., Bartfai, T. and Langel, U. 2001. Cargo delivery kinetics of cell-penetrating peptides. *Biochimica et Biophysica Acta* 1515(2), pp. 101–109.

Hazelwood, K.L., Olenych, S.G., Griffin, J.D., Cathcart, J.A. and Davidson, M.W. 2007. Entering the Portal: Understanding the Digital Image Recorded Through a Microscope. In: Shorte, S. L. and Frischknecht, F. eds. *Imaging Cellular and Molecular Biological Functions*. Principles and Practice. Berlin, Heidelberg: Springer Berlin Heidelberg, pp. 3–43.

Heinlein, T., Knemeyer, J.-P., Piestert, O. and Sauer, M. 2003. Photoinduced Electron Transfer between Fluorescent Dyes and Guanosine Residues in DNA-Hairpins. *The Journal of Physical Chemistry B* 107(31), pp. 7957–7964.

Henault, J., Martinez, J., Riggs, J.M., Tian, J., Mehta, P., Clarke, L., Sasai, M., Latz, E., Brinkmann, M.M., Iwasaki, A., Coyle, A.J., Kolbeck, R., Green, D.R. and Sanjuan, M.A. 2012. Noncanonical autophagy is required for type I interferon secretion in response to DNA-immune complexes. *Immunity* 37(6), pp. 986–997.

Hiroi, N., Draviam, V.M. and Funahashi, A. 2016. Editorial: quantitative biology: dynamics of living systems. *Frontiers in physiology* 7, p. 196.

Horisawa, K. 2014. Specific and quantitative labeling of biomolecules using click chemistry. *Frontiers in physiology* 5, p. 457.

Howell, D.P.-G., Krieser, R.J., Eastman, A. and Barry, M.A. 2003. Deoxyribonuclease II is a lysosomal barrier to transfection. *Molecular Therapy* 8(6), pp. 957–963.

Huber, C., Fähnrich, K., Krause, C. and Werner, T. 1999. Synthesis and characterization of new chloride-sensitive indicator dyes based on dynamic fluorescence quenching. *Journal of Photochemistry and Photobiology A: Chemistry*.

Inglefield, J.R. and Schwartz-Bloom, R.D. 1999. Fluorescence imaging of changes in intracellular chloride in living brain slices. *Methods* 18(2), pp. 197–203.

Ishii, K.J. and Akira, S. 2005. Innate immune recognition of nucleic acids: beyond toll-like receptors. *International Journal of Cancer* 117(4), pp. 517–523.

Jayaraman, S., Biwersi, J. and Verkman, A.S. 1999. Synthesis and characterization of dual-wavelength Cl--sensitive fluorescent indicators for ratio imaging. *The American Journal of Physiology* 276(3 Pt 1), pp. C747–57.

Jayaraman, S., Haggie, P., Wachter, R.M., Remington, S.J. and Verkman, A.S. 2000. Mechanism and cellular applications of a green fluorescent protein-based halide sensor. *The Journal of Biological Chemistry* 275(9), pp. 6047–6050.

Johnson, I.M., Kumar, S.G.B. and Malathi, R. 2003. De-intercalation of ethidium bromide and acridine orange by xanthine derivatives and their modulatory effect on anticancer agents: a study of DNA-directed toxicity enlightened by time correlated single photon counting. *Journal of Biomolecular Structure & Dynamics* 20(5), pp. 677–686.

Jones, M.R., Seeman, N.C. and Mirkin, C.A. 2015. Nanomaterials. Programmable materials and the nature of the DNA bond. *Science* 347(6224), p. 1260901.

Jung, S.-R., Fujimoto, B.S. and Chiu, D.T. 2017. Quantitative microscopy based on single-molecule fluorescence. *Current Opinion in Chemical Biology* 39, pp. 64–73.

Jungmann, R., Avendaño, M.S., Dai, M., Woehrstein, J.B., Agasti, S.S., Feiger, Z., Rodal, A. and Yin, P. 2016. Quantitative super-resolution imaging with qPAINT. *Nature Methods* 13(5), pp. 439–442.

Jungmann, R., Avendaño, M.S., Woehrstein, J.B., Dai, M., Shih, W.M. and Yin, P. 2014. Multiplexed 3D cellular super-resolution imaging with DNA-PAINT and Exchange-PAINT. *Nature Methods* 11(3), pp. 313–318.

Kaestner, L., Scholz, A. and Lipp, P. 2015. Conceptual and technical aspects of transfection and gene delivery. *Bioorganic & Medicinal Chemistry Letters* 25(6), pp. 1171–1176.

Kalnik, M.W., Norman, D.G., Li, B.F., Swann, P.F. and Patel, D.J. 1990. Conformational transitions in thymidine bulge-containing deoxytridecanucleotide duplexes. Role of flanking sequence and temperature in modulating the equilibrium between looped out and stacked thymidine bulge states. *The Journal of Biological Chemistry* 265(2), pp. 636–647.

Kasper, D., Planells-Cases, R., Fuhrmann, J.C., Scheel, O., Zeitz, O., Ruether, K., Schmitt, A., Poët, M., Steinfeld, R., Schweizer, M., Kornak, U. and Jentsch, T.J. 2005. Loss of the chloride channel ClC-7 leads to lysosomal storage disease and neurodegeneration. *The EMBO Journal* 24(5), pp. 1079–1091.

Kawane, K., Fukuyama, H., Kondoh, G., Takeda, J., Ohsawa, Y., Uchiyama, Y. and Nagata, S. 2001. Requirement of DNase II for definitive erythropoiesis in the mouse fetal liver. *Science* 292(5521), pp. 1546–1549.

Kawane, K., Motani, K. and Nagata, S. 2014. DNA degradation and its defects. *Cold Spring Harbor Perspectives in Biology* 6(6).

Kawane, K., Ohtani, M., Miwa, K., Kizawa, T., Kanbara, Y., Yoshioka, Y., Yoshikawa, H. and Nagata, S. 2006. Chronic polyarthritis caused by mammalian DNA that escapes from degradation in macrophages. *Nature* 443(7114), pp. 998–1002.

Kellenberger, C.A., Wilson, S.C., Sales-Lee, J. and Hammond, M.C. 2013. RNA-based fluorescent biosensors for live cell imaging of second messengers cyclic di-GMP and cyclic AMP-GMP. *Journal of the American Chemical Society* 135(13), pp. 4906–4909.

Kim, J., Choi, D.-K., Park, S., Shin, S.-M., Bae, J., Kim, D.-M., Yoo, T.H. and Kim, Y.-S. 2015. Quantitative assessment of cellular uptake and cytosolic access of antibody in living cells by an enhanced split GFP complementation assay. *Biochemical and Biophysical Research Communications* 467(4), pp. 771–777.

Koch, T., Hansen, H.F., Andersen, P., Larsen, T., Batz, H.G., Otteson, K. and Orum, H. 1997. Improvements in automated PNA synthesis using Boc/Z monomers. *The Journal of Peptide Research* 49(1), pp. 80–88.

Krieser, R.J., MacLea, K.S., Longnecker, D.S., Fields, J.L., Fiering, S. and Eastman, A. 2002. Deoxyribonuclease IIalpha is required during the phagocytic phase of apoptosis and its loss causes perinatal lethality. *Cell Death and Differentiation* 9(9), pp. 956–962.

Krishnan, Y. and Bathe, M. 2012. Designer nucleic acids to probe and program the cell. *Trends in Cell Biology* 22(12), pp. 624–633.

Krishnan, Y. and Simmel, F.C. 2011. Nucleic acid based molecular devices. *Angewandte Chemie* 50(14), pp. 3124–3156.

Kuner, T. and Augustine, G.J. 2000. A genetically encoded ratiometric indicator for chloride: capturing chloride transients in cultured hippocampal neurons. *Neuron* 27(3), pp. 447–459.

Lakowicz, J.R. ed. 2006. *Principles of Fluorescence Spectroscopy*. Boston, MA: Springer US.

Lamphier, M.S., Sirois, C.M., Verma, A., Golenbock, D.T. and Latz, E. 2006. TLR9 and the recognition of self and non-self nucleic acids. *Annals of the New York Academy of Sciences* 1082, pp. 31–43.

Lan, Y.Y., Londoño, D., Bouley, R., Rooney, M.S. and Hacohen, N. 2014. Dnase2a deficiency uncovers lysosomal clearance of damaged nuclear DNA via autophagy. *Cell reports* 9(1), pp. 180–192.

Lande, R., Gregorio, J., Facchinetti, V., Chatterjee, B., Wang, Yi-Hong, Homey, B., Cao, W., Wang, Yui-Hsi, Su, B., Nestle, F.O., Zal, T., Mellman, I., Schröder, J.-M., Liu, Y.-J. and Gilliet, M. 2007. Plasmacytoid dendritic cells sense self-DNA coupled with antimicrobial peptide. *Nature* 449(7162), pp. 564–569.

Leake, M.C., Chandler, J.H., Wadhams, G.H., Bai, F., Berry, R.M. and Armitage, J.P. 2006. Stoichiometry and turnover in single, functioning membrane protein complexes. *Nature* 443(7109), pp. 355–358.

Lee, S.-H., Shin, J.Y., Lee, A. and Bustamante, C. 2012. Counting single photoactivatable fluorescent molecules by photoactivated localization microscopy (PALM). *Proceedings of the National Academy of Sciences of the United States of America* 109(43), pp. 17436–17441.

Lewis, F.D. and Letsinger, R.L. 1998. Distance-dependent photoinduced electron transfer in synthetic single-strand and hairpin DNA. *Journal of Biological Inorganic Chemistry* 3(2), pp. 215–221.

Lilley, D.M. 1995. Kinking of DNA and RNA by base bulges. *Proceedings of the National Academy of Sciences of the United States of America* 92(16), pp. 7140–7142.

Litt, M.H., Kim, J. and Rodriguezparada, J.M. 1985. Synthesis of N-substituted polyethylenimines with polarizable side chain pendent groups. *Journal of Polymer Science: Polymer Chemistry Edition*.

Lorenz, S., Tomcin, S. and Mailänder, V. 2011. Staining of mitochondria with Cy5-labeled oligonucleotides for long-term microscopy studies. *Microscopy and microanalysis : the official journal of Microscopy Society of America, Microbeam Analysis Society, Microscopical Society of Canada* 17(3), pp. 440–445.

Majumdar, A., Cruz, D., Asamoah, N., Buxbaum, A., Sohar, I., Lobel, P. and Maxfield, F.R. 2007. Activation of microglia acidifies lysosomes and leads to degradation of Alzheimer amyloid fibrils. *Molecular Biology of the Cell* 18(4), pp. 1490–1496.

Marandi, N., Konnerth, A. and Garaschuk, O. 2002. Two-photon chloride imaging in neurons of brain slices. *Pflugers Archiv: European Journal of Physiology* 445(3), pp. 357–365.

Markova, O., Mukhtarov, M., Real, E., Jacob, Y. and Bregestovski, P. 2008. Genetically encoded chloride indicator with improved sensitivity. *Journal of Neuroscience Methods* 170(1), pp. 67–76.

Marras, S.A.E., Kramer, F.R. and Tyagi, S. 2002. Efficiencies of fluorescence resonance energy transfer and contact-mediated quenching in oligonucleotide probes. *Nucleic Acids Research* 30(21), p. e122.

Mckinney, R.M., Spillane, J.T. and Pearce, G.W. 1964. Factors affecting the rate of reaction of fluorescein isothiocyanate with serum proteins. *Journal of Immunology* 93, pp. 232–242.

Merrill, A.R., Palmer, J.L.R. and Szabos, A.G. 1993. Acrylamide Quenching of the Intrinsic Fluorescence of Tryptophan Residues Genetically Engineered into the Soluble Colicin E 1 Channel Peptide . Structural Characterization of the Insertion-Competent State7.

Modi, S., Halder, S., Nizak, C. and Krishnan, Y. 2014. Recombinant antibody mediated delivery of organelle-specific DNA pH sensors along endocytic pathways. *Nanoscale* 6(2), pp. 1144–1152.

Modi, S., M G, S., Goswami, D., Gupta, G.D., Mayor, S. and Krishnan, Y. 2009. A DNA nanomachine that maps spatial and temporal pH changes inside living cells. *Nature Nanotechnology* 4(5), pp. 325–330.

Modi, S., Nizak, C., Surana, S., Halder, S. and Krishnan, Y. 2013. Two DNA nanomachines map pH changes along intersecting endocytic pathways inside the same cell. *Nature Nanotechnology* 8(6), pp. 459–467.

Murphy, M.C., Rasnik, I., Cheng, W., Lohman, T.M. and Ha, T. 2004. Probing single-stranded DNA conformational flexibility using fluorescence spectroscopy. *Biophysical Journal* 86(4), pp. 2530–2537.

Nazarenko, I., Pires, R., Lowe, B., Obaidy, M. and Rashtchian, A. 2002. Effect of primary and secondary structure of oligodeoxyribonucleotides on the fluorescent properties of conjugated dyes. *Nucleic Acids Research* 30(9), pp. 2089–2195.

Nielsen, P.E., Egholm, M., Berg, R.H. and Buchardt, O. 1991. Sequence-selective recognition of DNA by strand displacement with a thymine-substituted polyamide. *Science* 254(5037), pp. 1497–1500.

Nielsen, P.E. and Haaima, G. 1997. Peptide nucleic acid (PNA). A DNA mimic with a pseudopeptide backbone. *Chemical Society Reviews* 26(2), p. 73.

Odaka, C. and Mizuochi, T. 1999. Role of macrophage lysosomal enzymes in the degradation of nucleosomes of apoptotic cells. *Journal of Immunology* 163(10), pp. 5346–5352.

Ohto, U., Shibata, T., Tanji, H., Ishida, H., Krayukhina, E., Uchiyama, S., Miyake, K. and Shimizu, T. 2015. Structural basis of CpG and inhibitory DNA recognition by Toll-like receptor 9. *Nature* 520(7549), pp. 702–705.

Olszowy, H.A., Rossiter, J., Hegarty, J. and Geoghegan, P. 1998. Background levels of bromide in human blood. *Journal of analytical toxicology* 22(3), pp. 225–230.

Paige, J.S., Wu, K.Y. and Jaffrey, S.R. 2011. RNA mimics of green fluorescent protein. *Science* 333(6042), pp. 642–646.

Paredes, J.M., Idilli, A.I., Mariotti, L., Losi, G., Arslanbaeva, L.R., Sato, S.S., Artoni, P., Szczurkowska, J., Cancedda, L., Ratto, G.M., Carmignoto, G. and Arosio, D. 2016. Synchronous bioimaging of intracellular ph and chloride based on LSS fluorescent protein. *ACS Chemical Biology* 11(6), pp. 1652–1660.

Pathak, S. and Mohan, C. 2011. Cellular and molecular pathogenesis of systemic lupus erythematosus: lessons from animal models. *Arthritis Research & Therapy* 13(5), p. 241.

Paul, B.D. and Smith, M.L. 2006. Cyanide and thiocyanate in human saliva by gas chromatography-mass spectrometry. *Journal of analytical toxicology* 30(8), pp. 511–515.

Penna, A., Demuro, A., Yeromin, A.V., Zhang, S.L., Safrina, O., Parker, I. and Cahalan, M.D. 2008. The CRAC channel consists of a tetramer formed by Stim-induced dimerization of Orai dimers. *Nature* 456(7218), pp. 116–120.

Pitchiaya, S., Androsavich, J.R. and Walter, N.G. 2012. Intracellular single molecule microscopy reveals two kinetically distinct pathways for microRNA assembly. *EMBO Reports* 13(8), pp. 709–715.

Pitchiaya, S., Krishnan, V., Custer, T.C. and Walter, N.G. 2013. Dissecting non-coding RNA mechanisms in cellulo by Single-molecule High-Resolution Localization and Counting. *Methods* 63(2), pp. 188–199.

Prakash, V., Saha, S., Chakraborty, K. and Krishnan, Y. 2016. Rational design of a quantitative, pH-insensitive, nucleic acid based fluorescent chloride reporter. *Chemical Science*.

Puchner, E.M., Walter, J.M., Kasper, R., Huang, B. and Lim, W.A. 2013. Counting molecules in single organelles with superresolution microscopy allows tracking of the endosome maturation trajectory. *Proceedings of the National Academy of Sciences of the United States of America* 110(40), pp. 16015–16020.

Qian, Z., Dougherty, P.G. and Pei, D. 2015. Monitoring the cytosolic entry of cell-penetrating peptides using a pH-sensitive fluorophore. *Chemical Communications* 51(11), pp. 2162–2165.

Raje, C.I., Kumar, S., Harle, A., Nanda, J.S. and Raje, M. 2007. The macrophage cell surface glyceraldehyde-3-phosphate dehydrogenase is a novel transferrin receptor. *The Journal of Biological Chemistry* 282(5), pp. 3252–3261.

Rigby, R.E., Webb, L.M., Mackenzie, K.J., Li, Y., Leitch, A., Reijns, M.A.M., Lundie, R.J., Revuelta, A., Davidson, D.J., Diebold, S., Modis, Y., MacDonald, A.S. and Jackson, A.P. 2014. RNA:DNA hybrids are a novel molecular pattern sensed by TLR9. *The EMBO Journal* 33(6), pp. 542–558.

Rincon-Restrepo, M., Mayer, A., Hauert, S., Bonner, D.K., Phelps, E.A., Hubbell, J.A., Swartz, M.A. and Hirosue, S. 2017. Vaccine nanocarriers: Coupling intracellular pathways and cellular biodistribution to control CD4 vs CD8 T cell responses. *Biomaterials* 132, pp. 48–58.

Rosen, M.A., Shapiro, L. and Patel, D.J. 1992. Solution structure of a trinucleotide ATA bulge loop within a DNA duplex. *Biochemistry*.

Saenger, W. 1984. *Principles of nucleic acid structure*. New York, NY: Springer New York.

Saha, S., Prakash, V., Halder, S., Chakraborty, K. and Krishnan, Y. 2015a. A pH independent , fluorescent DNA nanodevice quantitates chloride transport in subcellular organelles of living cells. *Nature nanotechnology*.

Saha, S., Prakash, V., Halder, S., Chakraborty, K. and Krishnan, Y. 2015b. A pH-independent DNA nanodevice for quantifying chloride transport in organelles of living cells. *Nature Nanotechnology* 10(7), pp. 645–651.

Sauer, M, Drexhage,K.H., Lieberwirth,U., Muller,R., Nord,S., Zander, C. 1998. Dynamics of the electron transfer reaction between an oxazine dye and DNA oligonucleotides monitored on the single-molecule level. *Chemical Physics Letters*.

Scott, C.C., Vacca, F. and Gruenberg, J. 2014. Endosome maturation, transport and functions. *Seminars in Cell & Developmental Biology* 31, pp. 2–10.

Seeman, N.C. 2010. Nanomaterials based on DNA. *Annual Review of Biochemistry* 79, pp. 65–87.

Seidel, C.A.M., Schulz, A. and Sauer, M.H.M. 1996. Nucleobase-Specific Quenching of Fluorescent Dyes. 1. Nucleobase One-Electron Redox Potentials and Their Correlation with Static and Dynamic Quenching Efficiencies. *The Journal of physical chemistry* 100(13), pp. 5541–5553.

Sener, Y., Tosun, G., Kahvecioglu, F., Gökalp, A. and Koç, H. 2007. Fluoride levels of human plasma and breast milk. *European journal of dentistry* 1(1), pp. 21–24.

Seong, C.-S., Varela-Ramirez, A. and Aguilera, R.J. 2006. DNase II deficiency impairs innate immune function in Drosophila. *Cellular Immunology* 240(1), pp. 5–13.

Shack, J. 1959. The influence of sodium and magnesium ions on the action of deoxyribonuclease II. *The Journal of Biological Chemistry* 234, pp. 3003–3006.

Sonawane, N.D., Thiagarajah, J.R. and Verkman, A.S. 2002. Chloride concentration in endosomes measured using a ratioable fluorescent Cl- indicator: evidence for chloride accumulation during acidification. *The Journal of Biological Chemistry* 277(7), pp. 5506–5513.

Sonawane, N.D. and Verkman, A.S. 2003. Determinants of [Cl-] in recycling and late endosomes and Golgi complex measured using fluorescent ligands. *The Journal of Cell Biology* 160(7), pp. 1129–1138.

Spectrometry, G.C., Kage, S., Kudo, K. and Ikeda, N. 2000. Determination of Azide in Blood and Urine by.

Sperinde, J.J., Choi, S.J. and Szoka, F.C. 2001. Phage display selection of a peptide DNase II inhibitor that enhances gene delivery. *The Journal of Gene Medicine* 3(2), pp. 101–108.

Stauber, T. and Jentsch, T.J. 2013. Chloride in vesicular trafficking and function. *Annual Review of Physiology* 75, pp. 453–477.

Stechmann, B., Bai, S.-K., Gobbo, E., Lopez, R., Merer, G., Pinchard, S., Panigai, L., Tenza, D., Raposo, G., Beaumelle, B., Sauvaire, D., Gillet, D., Johannes, L. and Barbier, J. 2010. Inhibition of retrograde transport protects mice from lethal ricin challenge. *Cell* 141(2), pp. 231–242.

Sugiyama, H. and Saito, I. 1996. Theoretical Studies of GG-Specific Photocleavage of DNA via Electron Transfer: Significant Lowering of Ionization Potential and 5‘-Localization of HOMO of Stacked GG Bases in B-Form DNA. *Journal of the American Chemical Society* 118(30), pp. 7063–7068.

Sugiyama, Y., Kawabata, I., Sobue, K. and Okabe, S. 2005. Determination of absolute protein numbers in single synapses by a GFP-based calibration technique. *Nature Methods* 2(9), pp. 677–684.

Suh, D. and Chaires, J.B. 1995. Criteria for the mode of binding of DNA binding agents. *Bioorganic & Medicinal Chemistry* 3(6), pp. 723–728.

Surana, S., Bhat, J.M., Koushika, S.P. and Krishnan, Y. 2011. An autonomous DNA nanomachine maps spatiotemporal pH changes in a multicellular living organism. *Nature Communications* 2, p. 340.

Surana, S., Bhatia, D. and Krishnan, Y. 2013. A method to study in vivo stability of DNA nanostructures. *Methods* 64(1), pp. 94–100.

Surana, S., Shenoy, A.R. and Krishnan, Y. 2015. Designing DNA nanodevices for compatibility with the immune system of higher organisms. *Nature Nanotechnology* 10(9), pp. 741–747.

Timtcheva, I., Maximova, V., Deligeorgiev, T., Zaneva, D. and Ivanov, I. 2000. New asymmetric monomethine cyanine dyes for nucleic-acid labelling: absorption and fluorescence spectral characteristics. *Journal of Photochemistry and Photobiology A: Chemistry* 130(1), pp. 7–11.

Tjelle, T.E., Brech, A., Juvet, L.K., Griffiths, G. and Berg, T. 1996. Isolation and characterization of early endosomes, late endosomes and terminal lysosomes: their role in protein degradation. *Journal of Cell Science* 109 (Pt 12), pp. 2905–2914.

Tomas, A., Futter, C.E. and Eden, E.R. 2014. EGF receptor trafficking: consequences for signaling and cancer. *Trends in Cell Biology* 24(1), pp. 26–34.

Tsekouras, K., Custer, T.C., Jashnsaz, H., Walter, N.G. and Pressé, S. 2016. A novel method to accurately locate and count large numbers of steps by photobleaching. *Molecular Biology of the Cell* 27(22), pp. 3601–3615.

Tyagi, S. and Kramer, F.R. 1996. Molecular beacons: probes that fluoresce upon hybridization. *Nature Biotechnology* 14(3), pp. 303–308.

Vallin, H., Perers, A., Alm, G.V. and Rönnblom, L. 1999. Anti-double-stranded DNA antibodies and immunostimulatory plasmid DNA in combination mimic the endogenous IFN-alpha inducer in systemic lupus erythematosus. *Journal of Immunology* 163(11), pp. 6306–6313.

Veetil, A.T., Chakraborty, K., Xiao, K., Minter, M.R., Sisodia, S.S. and Krishnan, Y. 2017. Cell-targetable DNA nanocapsules for spatiotemporal release of caged bioactive small molecules. *Nature Nanotechnology*.

Vivian, J.T. and Callis, P.R. 2001. Mechanisms of tryptophan fluorescence shifts in proteins. *Biophysical Journal* 80(5), pp. 2093–2109.

Wadsworth, S.J. and Goldfine, H. 2002. Mobilization of protein kinase C in macrophages induced by Listeria monocytogenes affects its internalization and escape from the phagosome. *Infection and Immunity* 70(8), pp. 4650–4660.

Wang, Y.H., Barker, P. and Griffith, J. 1992. Visualization of diagnostic heteroduplex DNAs from cystic fibrosis deletion heterozygotes provides an estimate of the kinking of DNA by bulged bases. *The Journal of Biological Chemistry* 267(7), pp. 4911–4915.

Wang, Y.H. and Griffith, J. 1991. Effects of bulge composition and flanking sequence on the kinking of DNA by bulged bases. *Biochemistry* 30(5), pp. 1358–1363.

Weihe, A. 2014. Quantification of organellar DNA and RNA using real-time PCR. *Methods in Molecular Biology* 1132, pp. 235–243.

Weisz, O.A. 2003. Organelle acidification and disease. *Traffic* 4(2), pp. 57–64.

Winterbourn, C.C., Hampton, M.B., Livesey, J.H. and Kettle, A.J. 2006. Modeling the reactions of superoxide and myeloperoxidase in the neutrophil phagosome: implications for microbial killing. *The Journal of Biological Chemistry* 281(52), pp. 39860–39869.

Wittung, P., Kim, S.K., Buchardt, O., Nielsen, P. and Nordèn, B. 1994. Interactions of DNA binding ligands with PNA-DNA hybrids. *Nucleic Acids Research* 22(24), pp. 5371–5377.

Wu, H.-L., Li, W.-Y., He, X.-W., Miao, K. and Liang, H. 2002. Spectral studies of the binding of lucigenin, a bisacridinium derivative, with double-helix DNA. *Analytical and Bioanalytical Chemistry* 373(3), pp. 163–168.

Yang, J., Chen, H., Vlahov, I.R., Cheng, J.-X. and Low, P.S. 2006. Evaluation of disulfide reduction during receptor-mediated endocytosis by using FRET imaging. *Proceedings of the National Academy of Sciences of the United States of America* 103(37), pp. 13872–13877.

Yu, H., Lai, H.-J., Lin, T.-W., Chen, C.-S. and Lo, S.J. 2015. Loss of DNase II function in the gonad is associated with a higher expression of antimicrobial genes in Caenorhabditis elegans. *The Biochemical Journal* 470(1), pp. 145–154.

Zacharias, M. and Hagerman, P.J. 1995. Bulge-induced bends in RNA: quantification by transient electric birefringence. *Journal of Molecular Biology* 247(3), pp. 486–500.

Zhong, S., Navaratnam, D. and Santos-Sacchi, J. 2014. A genetically-encoded YFP sensor with enhanced chloride sensitivity, photostability and reduced ph interference demonstrates augmented transmembrane chloride movement by gerbil prestin (SLC26a5). *Plos One* 9(6), p. e99095.